

# Local-to-global heating crossover in chains of nanomagnets: A two-scale analytical framework

H. Kachkachi

Université de Perpignan Via Domitia, Laboratoire PROMES-CNRS (UPR 8521), 66100 Perpignan, France

(Dated: 4 June 2026)

We develop a two-scale analytical formalism to study heat generation and thermal transport in one-dimensional systems of nanomagnets subjected to a uniform alternating magnetic field. At the nanoscale, each nanomagnet acts as a localized, temperature-dependent heat source governed by its magnetic response, dipolar interactions, and interfacial coupling to the matrix, characterized by a nanoscale volumetric loss coefficient  $L_m$ . After spatial and temporal averaging, we obtain a coarse-grained assembly-scale equation with effective heating terms and a macroscopic loss coefficient  $L_N$ .

Using modal decomposition, we solve both equations exactly under Dirichlet and Neumann boundary conditions and establish explicit conditions for a local-to-global heating crossover; this is governed by the competition between heat generation, diffusion, dipolar coupling, and hierarchical losses. The crossover is quantified through the spatial correlation length and temperature variance, with stability criteria incorporating both diffusion and nanoscale losses. The coarse-graining procedure is derived rigorously, and its systematic approximation errors are quantified.

For prototypical magnetic hyperthermia systems, such as magnetite nanomagnets in water, our formalism reveals that realistic parameters place these systems firmly in the collective heating regime, with local temperature variations at the  $\sim \mu\text{K}$  level, which is currently unresolvable experimentally. The continuum Fourier description used here is validated by a Knudsen-number analysis ( $\text{Kn} \ll 1$  for amorphous polymer and aqueous matrices).

## I. INTRODUCTION

Thermal transport in nanostructures, driven by nanoscale heat sources, is central to a wide range of physical, chemical, and biological processes<sup>1–3</sup> and applications, including magnetic hyperthermia<sup>4–6</sup>, nanoscale catalysis<sup>7–9</sup>, spin-caloritronics<sup>10–12</sup>, and thermally assisted switching<sup>13–15</sup> in nanostructured materials. In assemblies of nanomagnets subjected to alternating magnetic fields, each nanomagnet dissipates energy through magnetic relaxation mechanisms, converting the electromagnetic energy it absorbs into heat. This dissipation is commonly quantified by the Specific Absorption Rate (SAR), or Specific Loss Power (SLP), which depends on intrinsic magnetic parameters, such as particle size and anisotropy, interparticle dipolar interactions (DI), as well as on the amplitude and frequency of the applied field.

A fundamental question that arises in such systems concerns the spatial organization of heating. At sufficiently short times and small length scales, heat generation should *a priori* be inherently local. This implies that each nanomagnet acts as an individual source, giving rise to localized temperature elevations in its immediate vicinity<sup>16–18</sup>, thus constituting a *hotspot*. On the other hand, at longer times and larger scales, thermal diffusion, interparticle interactions, and heat exchange with the surrounding medium couple these sources, leading to collective heating and spatial homogenization of the temperature field<sup>4,19–22</sup>. Understanding the conditions under which a system could transition from localized to global heating, and whether such conditions are realizable in practice, is essential for controlling thermal effects

in applications ranging from targeted hyperthermia to nanoscale chemical activation<sup>5,16,23</sup>. In dense nanomagnet assemblies, magnetic dipolar coupling between the nanomagnets can significantly alter their collective magnetic response, thereby modifying the power dissipation under an AC field<sup>24–26</sup>. This anisotropic and long-range interaction not only shifts the effective anisotropy and relaxation times<sup>27–30</sup> but also introduces a temperature-dependent feedback that competes with purely thermal diffusion and interfacial coupling.

In this work we aim to establish a unified theoretical framework that accounts for both electromagnetic (dipolar) and thermal interplay in nanomagnet arrays, clarifying how interparticle spacing, which modulates dipolar coupling strength, affects the transition between local and global heating regimes. In this respect, a two-scale description is necessary. Indeed, estimating the orders of magnitude for an isolated nanomagnet reveals a number of stringent physical constraints. For example, the energy required to raise its temperature by 1 K is only  $\sim 10^{-17}$  J, and the associated thermal relaxation time is on the order of 0.1–1 ns, which is far shorter than typical AC-field periods ( $\sim \mu\text{s}$ ). This means that any temperature spike (or hotspot) generated during one field cycle decays completely before the next, making heating effectively impulsive at the nanomagnet level<sup>17,22,31</sup>. Furthermore, maintaining a steady elevation of even 1 K a few nanometers from an isolated nanomagnet would require an unrealistically large dissipated power ( $\text{SLP} \sim 10^9 \text{ W g}^{-1}$ ), far beyond experimentally attainable values ( $\sim 10^2\text{--}10^3 \text{ W g}^{-1}$  for state-of-the-art magnetite)<sup>5,6,32</sup>.

A conclusion of this short analysis is that observ-

able heating at realistic power levels necessarily involves the collective contribution of many nanomagnets across multiple length and time scales. However, most of the existing theoretical descriptions implicitly adopt a coarse-grained approach in which sources are pre-averaged over space and time and dissipation is modeled through effective volumetric loss terms. While adequate for macroscopic or long-time behavior<sup>16,17,19,22,33</sup>, this approach washes out local temperature variations by construction<sup>20,21,31</sup> and may require unphysically large loss coefficients to match observations. To address this issue, we develop a physically consistent description that explicitly separates, and then rigorously reconnects, two relevant scales. At the nanomagnet scale, individual nanomagnets are resolved as localized, temperature-dependent heat sources embedded in a thermal matrix. Heat exchange with the surrounding medium is characterized by both an interfacial (Newton-type) heat transfer coefficient  $h_s$ <sup>31,34,35</sup> and a nanoscale volumetric loss coefficient  $L_m$ . Then, the nanomagnet-scale heat equation, which incorporates these effects through renormalized coefficients  $\tilde{a}$  and  $\tilde{b}$  [see Eq. (18)], is solved exactly under Dirichlet and Neumann boundary conditions. At the assembly scale, we derive a coarse-grained heat equation by explicit spatial and temporal averaging (Section III C). At this scale, microscopic sources are replaced by effective heating terms consistent with the time-averaged SLP, and the environmental coupling is described by an assembly-scale loss coefficient  $L_N$ . Then, the relationship  $L_N = L_m + L_{\text{emergent}}$  implies that assembly-scale losses incorporate both direct nanoscale coupling and emergent large-scale contributions<sup>21,36,37</sup>. This approach allows us to (i) establish the mathematical conditions under which localized thermal hotspots can exist and persist, and (ii) quantify the crossover toward collective heating as diffusion, dipolar coupling, feedback ( $\tilde{b}$ ), and hierarchical losses ( $L_m, L_N$ ) compete.

Although developed explicitly for one-dimensional nanomagnet chains, a geometry that is analytically tractable and experimentally relevant<sup>38–40</sup>, the formalism is quite general. For typical hyperthermia ferrofluids, the present analysis places the system firmly in the collective regime, with local variations suppressed to the  $\sim \mu\text{K}$  level<sup>16,22,31</sup>. Our formalism thus identifies what parameter combinations, such as ultra-high SLP materials, sub-nanometer spacings, or MHz-range fields that outpace diffusion, would be required to access genuinely localized heating regimes.

*Organization of the paper:* The paper is organized as follows. Section II validates the continuum Fourier diffusion approximation via Knudsen number analysis. Section III introduces the two-scale theoretical framework: Section III A formulates the nanomagnet-resolved heat equation with nanoscale losses and interfacial coupling, presenting its exact analytical solution in terms of renormalized coefficients; Section III B introduces the coarse-grained, assembly-scale heat equation; and Section III C explicitly derives the mathematical connection between

the two descriptions. Section IV provides explicit scaling relations between physical parameters and dimensionless control variables, with reference values for magnetite-PMMA and magnetite-water systems. Section V analyzes the resulting thermal dynamics, identifies the indicators of the local-to-global heating crossover, quantifies the two-scale consistency and its systematic limitations, and provides physical interpretation of boundary condition effects. The expressions of the heating terms and their relation to SLP calculations are addressed in Appendix A, a comparison between Dirichlet boundary conditions (DBC) and Neumann boundary conditions (NBC) is presented in Appendix B, and for completeness, Appendix C presents an alternative Green’s function formulation of the nanomagnet-scale problem.

## II. VALIDITY OF THE CONTINUUM APPROXIMATION AT THE NANOSCALE

A critical requirement for modeling thermal transport at the nanoscale is to determine the applicability of classical Fourier diffusion<sup>1,35,41–44</sup>. In low-dimensional crystalline systems, such as silicon nanowires, the phonon mean free path ( $\Lambda_{\text{mfp}}$ ) can exceed hundreds of nanometers, leading to ballistic transport and a breakdown of Fourier’s law when the system dimensions are comparable to  $\Lambda_{\text{mfp}}$ . However, the validity of the continuum approximation depends intrinsically on the material’s crystalline order and the resulting phonon scattering rates. Here, we explicitly define the physical regime in which our two-scale framework is valid.

### A. Length scale hierarchy and Knudsen number

The transition from diffusive to ballistic transport is governed by the Knudsen number,  $Kn = \Lambda_{\text{mfp}}/d$ , where  $d$  is the characteristic system length scale (here, the interparticle spacing). Fourier’s law is valid only in the limit  $Kn \ll 1$ <sup>45–47</sup>.

We consider nanomagnets embedded in two distinct environments: an amorphous polymer matrix (PMMA) and an aqueous fluid.

1. **Amorphous matrices (PMMA):** In amorphous solids, the lack of long-range structural order leads to strong phonon scattering. The phonon mean free path is typically on the order of the interatomic spacing or short-range correlation lengths. For PMMA at room temperature,  $\Lambda_{\text{PMMA}} \simeq 0.5 - 2$  nm.
2. **Liquid matrices (water):** In aqueous ferrofluids, heat transport is dominated by molecular collisions with extremely short mean free paths,  $\Lambda_{\text{water}} < 0.5$  nm.

For the typical interparticle spacings considered in this work ( $d \simeq 30 - 50$  nm, i.e., at least three times the NM

diameter), we calculate the Knudsen number:

$$Kn_{\text{PMMA}} \simeq \frac{2 \text{ nm}}{30 \text{ nm}} \simeq 0.07, \quad Kn_{\text{water}} \simeq \frac{0.3 \text{ nm}}{30 \text{ nm}} \simeq 0.01. \quad (1)$$

In both cases,  $Kn \ll 1$  (or at most  $Kn \sim 0.1$  for very dense PMMA arrays). Consequently, the phonon transport is dominated by scattering events within the matrix rather than boundary scattering at the nanomagnets. This places the system firmly in the diffusive regime, justifying the use of the parabolic heat equation (4) and the definition of an effective thermal conductivity  $\kappa_m$ .

It is important to note that our framework would not apply without modification to nanomagnets embedded in crystalline matrices (e.g., Silicon or Graphene)<sup>46,47</sup>, where  $\Lambda_{\text{mfp}} \sim 100 \text{ nm}$  would yield  $Kn > 1$ , necessitating a ballistic-diffusive approach such as the Cattaneo-Vernotte equation<sup>48,49</sup> or the Boltzmann Transport Equation<sup>50,51</sup>.

## B. Timescale separation and thermal inertia

The validity of the parabolic diffusion model also requires that the observation timescale dominates the thermal relaxation time of the heat carriers (phonons),  $\tau_{\text{ph}}$ . The Cattaneo-Vernotte equation<sup>48,49</sup>, which accounts for the finite velocity of heat propagation (second sound), introduces a relaxation term  $\tau_{\text{ph}} \partial \mathbf{q} / \partial t$ . For amorphous polymers,  $\tau_{\text{ph}}$  is on the order of 1 – 10 ps. In contrast, the magnetic heating occurs on the timescale of the AC driving field period,  $\mathcal{T}_{\text{AC}} = 1/f$ . For a typical frequency  $f = 200 \text{ kHz}$ , the excitation period is  $\mathcal{T}_{\text{AC}} \simeq 5 \mu\text{s}$ . The diffusive time scale across the interparticle spacing is  $t_d \simeq 0.1 - 1 \text{ ns}$ . The hierarchy of time scales thus is:

$$\tau_{\text{ph}} (\sim 10 \text{ ps}) \ll t_d (\sim 1 \text{ ns}) \ll \mathcal{T}_{\text{AC}} (\sim 5000 \text{ ns}). \quad (2)$$

Since the thermal inertia timescale  $\tau_{\text{ph}}$  is orders of magnitude shorter than the diffusion time  $t_d$ , the hyperbolic terms in the heat equation can be safely neglected. The system operates in a quasi-static thermal regime relative to the phonon dynamics, ensuring thermodynamic consistency without the need for generalized hydrodynamic terms.

## III. THEORETICAL FRAMEWORK

### A. Nanomagnet-scale heat equation

Now, we formulate the thermal problem at the scale of individual nanomagnets, where heat is generated from magnetic dissipation under an alternating magnetic field and is transferred locally to the surrounding matrix. This description resolves spatial variations on nanometer length scales and applies to time scales larger than the AC-field period but short compared to macroscopic thermal relaxation times. At this scale, each nanomagnet

acts as a localized heat source embedded in a continuous host medium, and exchanges heat with its immediate surroundings through interfacial thermal coupling.

We consider a one-dimensional domain  $0 \leq x \leq L$  containing a chain of  $\mathcal{N}$  nanomagnets located at positions

$$x_n = nd, \quad n = 0, \dots, \mathcal{N} - 1, \quad (3)$$

where  $d$  is the interparticle spacing and  $L = (\mathcal{N} - 1)d$ . The nanomagnets are embedded in a homogeneous matrix characterized by mass density  $\rho_m$ , specific heat  $c_{v,m}$ , and thermal conductivity  $\kappa_m$ .

The temperature field  $T(x, t)$  denotes the continuous temperature in the embedding medium. It obeys the heat equation

$$\rho_m c_{v,m} \frac{\partial T}{\partial t} - \kappa_m \frac{\partial^2 T}{\partial x^2} = \sum_{n=0}^{\mathcal{N}-1} P_n(t) \delta(x - x_n) - L_m [T(x, t) - T_0], \quad (4)$$

where  $P_n(t)$  is the *power density per unit transverse area* ( $\text{W}/\text{m}^2$ ) dissipated by the nanomagnet  $n$  and transferred to the surrounding matrix, and  $L_m$  is a volumetric Newton cooling coefficient representing heat leakage from the matrix to the external environment at the nanoscale. More precisely, it characterizes direct environmental coupling of the immediate matrix surrounding each nanomagnet. At the nanoscale and short times ( $t \sim t_d$ , where  $t_d$  is the diffusion time across one interparticle spacing), heat remains largely confined near the NM, and environmental losses are relatively weak.

For each nanomagnet  $n$ , we distinguish: (i) its internal (assumed uniform) temperature  $T_i^{(n)}(t)$ , (ii) its surface temperature  $T_s^{(n)}(t)$ , and (iii) the matrix temperature  $T(x, t)$  evaluated at the nanomagnet position,  $T(x_n, t)$ .

At the nanomagnet scale, we model heat exchange between each nanomagnet and the matrix via an interfacial (Newtonian) thermal conductance  $h_s$  ( $\text{W m}^{-2}\text{K}^{-1}$ ). Because of the small nanomagnet size ( $R \sim 10 \text{ nm}$ ) and high internal thermal conductivity  $\kappa_p$ , the Biot number<sup>1</sup>  $\text{Bi} = R/(\kappa_p/h_s) \ll 1$ , justifying the approximation,

$$T_i^{(n)}(t) = T_s^{(n)}(t), \quad (5)$$

so that the nanomagnet is characterized by a single internal temperature.

Therefore, heat transfer between a nanomagnet  $n$  and the surrounding matrix is governed by (Newtonian) interfacial exchange,

$$P_n(t) = h_s [T_s^{(n)}(t) - T(x_n, t)], \quad (6)$$

<sup>1</sup>The Biot number (Bi) is defined as the ratio of internal conduction resistance to external convection resistance [See Ref. 1]:  $\text{Bi} = hL/\kappa$ , where  $h$  is the heat transfer coefficient ( $\text{W}/\text{m}^2/\text{K}$ ),  $L$  the characteristic length (m), and  $\kappa$  the thermal conductivity of the solid ( $\text{W}/\text{m}/\text{K}$ ).

This equation defines how the nanomagnet injects heat into the matrix and ensures that thermal coupling between different nanomagnets is mediated through the temperature field  $T(x, t)$ .

Each nanomagnet is subjected to an AC magnetic field of angular frequency  $\omega$  and amplitude  $h_0$ . Magnetic dissipation occurs on the time scale of the AC period  $\mathcal{T}_{AC} = 2\pi/\omega$ . Since thermal diffusion and interfacial heat exchange are much slower than the field oscillations, we replace the instantaneous dissipated power by its cycle-averaged value,

$$P_n(t) \longrightarrow \bar{P}_n(T_i^{(n)}). \quad (7)$$

The cycle-averaged magnetic power dissipated inside a nanomagnet  $n$  is related to the specific loss power (SLP), in W/kg, as

$$\bar{P}_n(T_i^{(n)}) = \frac{V_p \rho_p}{A_p} \text{SLP}(T_i^{(n)}), \quad (8)$$

where  $A_p$  is the nanomagnet surface area,  $V_p$  its volume and  $\rho_p$  its mass density. For a spherical nanomagnet of radius  $R$ , the coefficient in Eq. (8) becomes  $R\rho_p/3$ .

$\text{SLP}(T_i^{(n)})$  depends on the nanomagnet's internal temperature through its magnetic relaxation parameters, as derived in Appendix A from the linear response theory, taking into account (weak) dipolar interactions<sup>4,6,25,33,52</sup>,

$$\rho_p \text{SLP}(T) = \frac{\mu_0 h_0^2 \omega}{2} \chi_{\text{eq}}(T) \frac{\eta(T)}{1 + \eta^2}, \quad \eta(T) = \frac{\omega}{\Gamma(T)}, \quad (9)$$

where  $\chi_{\text{eq}}$  is the equilibrium susceptibility and  $\Gamma(T)$  the relaxation rate.

Combining Eqs. (6) and (8) gives the self-consistent relation for the nanomagnet's internal temperature:

$$\frac{V_p \rho_p}{A_p} \text{SLP}(T_i^{(n)}) = h_s [T_i^{(n)} - T(x_n, t)], \quad (10)$$

which implicitly determines  $T_i^{(n)}$  in terms of the local matrix temperature  $T(x_n, t)$  [see below]. This coupling indirectly links all nanomagnets through the matrix temperature field  $T(x, t)$ .

In a prototypical situation, we have moderate (relative) temperature elevations ( $|T_i^{(n)} - T_0| \ll T_0$ )<sup>33</sup>, so that the SLP can be linearized about the ambient temperature  $T_0$  and written in terms of the relative temperature elevation

$$\theta_i^{(n)}(t) = \frac{T_i^{(n)}(t) - T_0}{T_0}, \quad (11)$$

as

$$\rho_p \text{SLP}(T_i^{(n)}) \simeq a_p(T_0) + b_p(T_0) \theta_i^{(n)}, \quad (12)$$

where the coefficients  $a_p(T_0)$  and  $b_p(T_0)$  which encode, respectively, the baseline heating strength and

the thermo-magnetic feedback; their explicit expressions, their plots, and other details are given in Appendix A.

Therefore, using Eqs. (8, 12), the cycle-averaged power injected by nanomagnet  $n$  can be written as

$$\bar{P}_n(T_i^{(n)}) = \frac{V_p}{A_p} [a_p + b_p \theta_i^{(n)}]. \quad (13)$$

The relationship between the nanomagnet's internal temperature  $\theta_i^{(n)}$  and the matrix temperature at the nanomagnet position,  $\theta(x_n, t)$ , is obtained from the self-consistent condition equating the magnetic power dissipated inside the nanomagnet to the interfacial heat flux into the matrix, Eqs. (8, 10). Substituting the linearized power expression Eq. (13) and the Newtonian exchange law Eq. (6) yields:

$$\frac{V_p}{A_p} [a_p + b_p \theta_i^{(n)}(t)] = T_0 h_s [\theta_i^{(n)} - \theta(x_n, t)], \quad (14)$$

where we have also introduced the relative temperature elevation

$$\theta(x, t) = \frac{T(x, t) - T_0}{T_0}.$$

Using the (renormalized) interfacial coupling strength (in W/m<sup>3</sup>),  $\gamma_s = A_p h_s T_0 / V_p$ , and introducing the following dimensionless coefficients

$$\gamma \equiv \frac{\gamma_s}{a_p}, \quad \varepsilon \equiv \frac{b_p}{a_p}, \quad (15)$$

Eq. (14) can be solved for  $\theta_i^{(n)}$  to obtain the explicit relation

$$\theta_i^{(n)}(t) = \frac{1 + \gamma \theta(x_n, t)}{\gamma - \varepsilon}, \quad (16)$$

which is valid for arbitrary  $\gamma$ .

Let us now introduce the following dimensionless space and time variables

$$\xi = \frac{x}{d}, \quad \tau = \frac{t}{t_d}, \quad t_d = \frac{\rho_m c_v m d^2}{\kappa_m}, \quad (17)$$

where  $t_d$  is interpreted as the *thermal diffusion time* over one interparticle spacing  $d$ .

Next, substituting Eq. (16) into Eq. (13) eliminates the explicit dependence on the nanomagnet's internal temperature  $\theta_i^{(n)}$  and leads to the following closed equation (dimensionless) for the matrix temperature  $\theta(\xi, \tau)$

$$\frac{\partial \theta}{\partial \tau} - \frac{\partial^2 \theta}{\partial \xi^2} = \sum_{n=0}^{N-1} [\tilde{a} + \tilde{b} \theta(\xi_n, \tau)] \delta(\xi - \xi_n) - \beta \theta(\xi, \tau), \quad (18)$$

where the renormalized heating coefficients

$$\tilde{a} = \frac{\gamma}{\gamma - \varepsilon} a, \quad \tilde{b} = \frac{\gamma}{\gamma - \varepsilon} b, \quad (19)$$

incorporate the effect of finite interfacial thermal resistance through the dimensionless coupling strength  $\gamma$ . For later convenience, we have introduced, respectively, the renormalized baseline heating strength, the thermo-magnetic feedback and the nanoscale loss coefficient

$$a = \Upsilon_0 a_p, \quad b = \Upsilon_0 b_p, \quad \beta \equiv \frac{L_m t_d}{\rho_m c_{v,m}}, \quad (20)$$

with

$$\Upsilon_0 \equiv \frac{V_p t_d}{A_p \rho_m c_{v,m} T_0 d}. \quad (21)$$

The parameter  $\beta$  can also be written as  $\beta = t_d/t_l$ , where  $t_l = \rho_m c_{v,m}/L_m$  represents the leakage time.

In the strong interfacial-coupling limit ( $\gamma \gg |\varepsilon|$ ), Eq. (16) reduces to  $\theta_i^{(n)} \simeq \theta(x_n, t)$ , implying that the nanomagnet and matrix temperatures are essentially equal, and the renormalized coefficients recover their bare values,  $\tilde{a} \rightarrow a$ ,  $\tilde{b} \rightarrow b$ . For finite  $\gamma$ , however, the nanomagnet's internal temperature differs from the matrix temperature: the parameter  $\varepsilon$  is renormalized by the interfacial thermal resistance through the denominator  $\gamma - \varepsilon$ , and the resulting coefficients  $\tilde{a}$ ,  $\tilde{b}$  modify both the baseline heating and the thermo-magnetic feedback, thereby capturing the influence of interfacial resistance on the effective heat injection into the matrix<sup>1</sup>.

Note that, by using the delta function on the right-hand side of Eqs. (4, 18), we are considering the nanomagnets as point heat sources. However, to reflect finiteness of the nanomagnet size, we may replace the point sources at  $\xi_n$  by narrow Gaussian functions

$$g_{\sigma_g}(\xi - \xi_n) = \frac{1}{\sqrt{2\pi}\sigma_g} \exp\left(-\frac{(\xi - \xi_n)^2}{2\sigma_g^2}\right), \quad (22)$$

$$\int_{\mathbb{R}} g_{\sigma_g}(\xi) d\xi = 1, \quad (23)$$

so that the first term on right-hand side of (18) becomes

$$\sum_{n=0}^{\mathcal{N}-1} \left[ \tilde{a} + \tilde{b} \theta(\xi_n, \tau) \right] g_{\sigma_g}(\xi - \xi_n).$$

As such, the feedback is still local in temperature (evaluated at the particle center  $\xi_n$ ), but spatially distributed over a small neighborhood by  $g_{\sigma_g}$ .

We now impose Dirichlet boundary conditions,

$$\theta(0, \tau) = \theta(\Lambda, \tau) = 0, \quad \Lambda = \frac{L}{d}, \quad (24)$$

<sup>1</sup>Furthermore, Kapitza-interface effects at nanomagnet/matrix contact can be included by introducing the Kapitza resistance  $R_K$  (or conductance  $G = 1/R_K$ , and replacing  $b \rightarrow b_{\text{eff}} = \lambda b$ ,  $a \rightarrow a_{\text{eff}} = \lambda a$ , with  $\lambda = \Lambda_3/(1 + \Lambda_3)$ ,  $\Lambda_3 = GR/\kappa$ ;  $R$  is the radius of the nanomagnet.

corresponding to a nanomagnet chain in contact with an ideal thermal bath.

The choice of boundary conditions—Dirichlet (DBC) versus Neumann (NBC)—has non-trivial consequences for the thermal response of the assembly, and a detailed comparison is deferred to Sections (III D 3, V) and Appendix B. Here we proceed with DBC by way of illustration and build the exact modal solution, the structure of which carries over directly to NBC with the substitution of the corresponding eigenfunctions.

The solution of Eq. (18) is obtained by expanding the temperature field in the orthonormal Dirichlet eigenfunctions

$$\phi_r(\xi) = \sqrt{\frac{2}{\Lambda}} \sin\left(\frac{r\pi\xi}{\Lambda}\right), \quad r = 1, 2, \dots, \quad (25)$$

as

$$\theta(\xi, \tau) = \sum_{r=1}^{\infty} c_r(\tau) \phi_r(\xi). \quad (26)$$

The modal amplitudes satisfy the coupled system

$$\frac{d\mathbf{c}}{d\tau} = \mathbf{B}\mathbf{c} + \mathbf{d}, \quad (27)$$

where  $\mathbf{c} = (c_1, \dots, c_R)^T$ ,

$$B_{rs} = -(\lambda_r + \beta)\delta_{rs} + \tilde{b} \sum_{n=0}^{\mathcal{N}-1} \phi_r(\xi_n)\phi_s(\xi_n), \quad (28)$$

$$d_r = \tilde{a} \sum_{n=0}^{\mathcal{N}-1} \phi_r(\xi_n), \quad (29)$$

and  $\lambda_r = (r\pi/\Lambda)^2$ .

For vanishing initial (relative) temperature,  $\mathbf{c}(0) = \mathbf{0}$ , the exact solution is

$$\mathbf{c}(\tau) = \mathbf{B}^{-1} (e^{\mathbf{B}\tau} - \mathbf{I}) \mathbf{d}. \quad (30)$$

Substitution into the eigenfunction expansion (26) yields the full space–time temperature field  $\theta(\xi, \tau)$ . This exact solution provides complete access to transient dynamics, steady states, and stability properties of nanomagnet-scale heating, and forms the basis for the analysis of localized hotspots and thermal overlap presented in the following sections.

## B. Assembly-scale heat equation and coarse-grained description

We now turn to the description of heat transport at the scale of the entire nanomagnet assembly and its embedding matrix. This second level of description is obtained by coarse-graining the nanoscale temperature field over space and time scales large compared to the nanomagnet size and the AC-field period. It is intended to capture

the collective thermal response of the array rather than the detailed structure of local hotspots.

At the assembly scale, we assume that: (i) the temperature field varies smoothly on length scales larger than the interparticle distance  $d$ ; (ii) fast nanoscale temperature oscillations over individual AC cycles have been averaged out; (iii) the surrounding matrix and environment act as effective thermal reservoirs characterized by macroscopic transport and leakage parameters.

Under these conditions, the detailed nanomagnet-resolved source term  $P_n(t)\delta(\mathbf{r} - \mathbf{r}_n)$  introduced in Sec. III A is replaced by an effective volumetric heat source  $Q_{\text{eff}}(\mathbf{r}, t)$ , representing the spatial and temporal average of the power dissipated by many nanomagnets within a coarse-graining volume. The resulting temperature field  $T_{\text{cg}}(\mathbf{r}, t)$  describes the collective thermal response of the assembly; see Eq. (44).

The assembly-scale temperature field obeys the standard heat equation with effective material parameters,

$$\rho_{\text{eff}}c_{v,\text{eff}}\frac{\partial T_{\text{cg}}}{\partial t}(\mathbf{r}, t) = \kappa_{\text{eff}}\nabla^2 T_{\text{cg}}(\mathbf{r}, t) + Q_{\text{eff}}(\mathbf{r}, t) - L_N[T_{\text{cg}}(\mathbf{r}, t) - T_0], \quad (31)$$

where  $\rho_{\text{eff}}c_{v,\text{eff}}$  and  $\kappa_{\text{eff}}$  are the effective volumetric heat capacity and thermal conductivity of the nanocomposite, and  $L_N$  is an effective volumetric Newtonian cooling coefficient describing heat leakage from the assembly to the external environment.

The solution of Eq. (31), with and without the diffusion term, was investigated in Refs. 33 and 36 for the prototypical ferrofluids of magnetite and maghemite nanomagnet in water, where the parameter  $L_N$  was estimated by adjusting the solution to the experimental data.

The coefficient  $L_N$  represents the total effective environmental coupling after coarse-graining and its hierarchical relationship with  $L_m$  can be written as  $L_N = L_m + L_{\text{emergent}}$ , where

- $L_m$  is the nanoscale loss coefficient (introduced earlier).
- $L_{\text{emergent}}$  captures additional losses that become significant. only at larger scales and longer times, including:
  1. Boundary effects as heat reaches system edges.
  2. Enhanced heat exchange when temperature gradients span the entire assembly.
  3. Collective modes of environmental coupling.

Typical values for the systems studied here are:

$$\text{PMMA nanocomposite: } L_N \sim 10^4 - 10^5 \text{ W}/(\text{K}\cdot\text{m}^3)$$

$$\text{Aqueous ferrofluid: } L_N \sim 10^5 - 10^6 \text{ W}/(\text{K}\cdot\text{m}^3)$$

The ratio  $L_N/L_m \sim 10 - 100$  quantifies the emergent losses that develop as heat diffuses beyond the nanoparticle vicinity.

Similarly to the nanoscale, we introduce the relative temperature elevation

$$\Theta(\mathbf{r}, t) = \frac{T_{\text{cg}}(\mathbf{r}, t) - T_0}{T_0}, \quad (32)$$

the characteristic leakage time

$$t_s = \frac{\rho_{\text{eff}}c_{v,\text{eff}}}{L_N}, \quad (33)$$

and the dimensionless coordinate

$$\boldsymbol{\xi} = \frac{\mathbf{r}}{\ell_c}, \quad \ell_c = L, \quad (34)$$

so that  $\nabla^2 = \ell_c^{-2}\nabla_{\boldsymbol{\xi}}^2$ . Note that now  $\ell_c$  is the full chain's length.

Then, defining the dimensionless time  $\tau_s = t/t_s$ , we obtain the heat equation at the assembly scale

$$\frac{\partial \Theta}{\partial \tau_s} = \zeta \nabla_{\boldsymbol{\xi}}^2 \Theta - \Theta + \Xi_{\text{cg}}(\boldsymbol{\xi}, \tau_s), \quad (35)$$

with

$$\zeta = \frac{\kappa_{\text{eff}}}{L_N \ell_c^2} = \frac{\kappa_{\text{eff}}}{L_N L^2}, \quad \Xi_{\text{cg}} = \frac{Q_{\text{eff}}}{L_N T_0}. \quad (36)$$

We again refer to the work in Ref. 36 for a discussion of this formulation applied to magnetite ferrofluids.

At this scale, the effective source term  $\Xi_{\text{cg}}$  is directly related to the *time-averaged* SLP of the nanomagnet, as derived in Appendix A. After coarse-graining, it may be expressed in the linearized form

$$\Xi_{\text{cg}}(\mathbf{r}, \tau_s) \simeq a_{\text{cg}} + b_{\text{cg}} \Theta(\mathbf{r}, \tau_s), \quad (37)$$

where the coefficients  $a_{\text{cg}}$  and  $b_{\text{cg}}$  are obtained from the SLP expressions by averaging over the nanomagnets within the coarse-graining volume and normalizing by  $L_N T_0$ .

For consistency with the nanoscale analysis, we restrict attention to a one-dimensional domain  $0 \leq \xi \leq \Lambda$  and impose Dirichlet boundary conditions,

$$\Theta(0, \tau_s) = \Theta(\Lambda, \tau_s) = 0, \quad (38)$$

corresponding to an idealized thermal bath at the system boundaries. As at the nanoscale, the modal solution structure carries over directly to NBC with the substitution of the corresponding eigenfunctions; the two cases are compared in Sections (III D 3, V) and Appendix B.

Under these conditions, Eq. (35) admits the same modal structure as the nanoscale problem, with the crucial difference that the source term is now spatially smooth rather than localized at discrete particle sites. As a result, only long-wavelength modes contribute significantly to the temperature field, reflecting the collective nature of heating at the assembly scale.

The assembly-scale equation (35) provides a macroscopic description valid after sufficient temporal and spatial averaging. Its main role in the present work is to connect the nanoscale heating physics to previously studied

collective thermal transport models<sup>4,6,33,36,37,53–59</sup> and to identify the conditions under which localized heating crosses over to global, homogenized behavior.

Now, we discuss the mathematical and physical connection between the nanoscale and assembly-scale equations.

### C. Relation between nanomagnet-scale and assembly-scale descriptions

Sections III A and III B describe thermal transport at two distinct but complementary space-time scales. Here we derive how the coarse-grained heat equation emerges from the nanomagnet-scale formulation through controlled averaging, and establish quantitative relations between the parameters at each scale.

#### 1. Separation of space and time scales

The key assumption underlying the two-scale approach is a strong separation of characteristic time and length scales:

$$t_d \ll T_{AC} \ll t_s, \quad R \ll d \ll L, \quad (39)$$

where  $t_d \sim d^2/\alpha$  is the thermal diffusion time across one interparticle spacing [Eq. (17)],  $T_{AC} = 2\pi/\omega$  is the AC-field period, and  $t_s$  is the macroscopic (assembly-level) thermal leakage time [Eq. (33)];  $R$  is the nanomagnet radius,  $d$  the interparticle spacing, and  $L$  the system size.

For the systems considered here (magnetite in PMMA or water):

- $t_d \sim 10 - 15$  ns (diffusion across  $d \sim 30$  nm)
- $T_{AC} \sim 5$   $\mu$ s (for  $f = 194$  kHz)
- $t_s \sim 0.1-1$  s (depending on  $L_N$ )
- $R \sim 10$  nm,  $d \sim 30-50$  nm,  $L \sim 2$   $\mu$ m

The hierarchy (39) is thus satisfied with comfortable margins:  $t_d/T_{AC} \sim 10^{-3}$ ,  $T_{AC}/t_s \sim 10^{-5}$ , and  $d/L \sim 10^{-2}$ .

At the nanomagnet scale, the magnetic power loss is first averaged over one AC cycle, yielding the time-averaged power  $\overline{P}_n(T)$  used in Eq. (4). The next averaging step is performed over times  $\Delta t$  such that

$$T_{AC} \ll \Delta t \ll t_s, \quad (40)$$

which filters out nanomagnet-scale transients while preserving the slow evolution of the macroscopic temperature field.

Averaging the source term in Eq. (4) over  $\Delta t$  gives:

$$Q_{\text{eff}}(x, t) = \frac{1}{\Delta t} \int_t^{t+\Delta t} \sum_{n=0}^{\mathcal{N}-1} \overline{P}_n [T(x_n, t')] \delta(x - x_n) dt'. \quad (41)$$

Because  $\Delta t \gg t_d$ , the temperature  $T(x_n, t')$  varies slowly over the interval  $[t, t + \Delta t]$ , and we can approximate:

$$Q_{\text{eff}}(x, t) \simeq \sum_{n=0}^{\mathcal{N}-1} \overline{P}_n [T(x_n, t)] \delta(x - x_n), \quad (42)$$

where  $\overline{P}_n$  denotes the time-averaged power at the quasi-steady temperature  $T(x_n, t)$ , see Section III A.

The next coarse-graining step consists in averaging over spatial regions of size  $\ell_{\text{cg}}$  satisfying

$$d \ll \ell_{\text{cg}} \ll L. \quad (43)$$

We define the coarse-grained temperature as:

$$T_{\text{cg}}(x, t) = \frac{1}{\ell_{\text{cg}}} \int_{x-\ell_{\text{cg}}/2}^{x+\ell_{\text{cg}}/2} T(x', t) dx', \quad (44)$$

and similarly for the source term:

$$Q_{\text{cg}}(x, t) = \frac{1}{\ell_{\text{cg}}} \int_{x-\ell_{\text{cg}}/2}^{x+\ell_{\text{cg}}/2} \sum_n \overline{P}_n \delta(x' - x_n) dx'. \quad (45)$$

For a uniform distribution of nanomagnets with concentration  $n_{\text{NM}} = 1/d$  (one nanomagnet per interparticle spacing), the number of nanomagnets within the averaging window is  $N_{\text{win}} = \ell_{\text{cg}}/d \gg 1$ . The discrete sum over delta functions is then replaced by:

$$Q_{\text{cg}}(x, t) = n_{\text{NM}} \langle \overline{P}_n \rangle = \frac{1}{d} \langle \overline{P}_n \rangle, \quad (46)$$

where  $\langle \overline{P}_n \rangle$  is the average power per nanomagnet in the coarse-graining volume.

Using the linearized form  $\overline{P}_n = (V_p/A_p)[a_p + b_p \theta_i^{(n)}]$  from Eq. (12), and noting that after coarse-graining  $\theta_i^{(n)} \simeq \Theta(x, t)$  (the assembly-scale relative temperature), we obtain:

$$Q_{\text{cg}}(x, t) = \frac{V_p}{A_p d} [a_p + b_p \Theta(x, t)]. \quad (47)$$

Dividing by  $L_N T_0$  to obtain the dimensionless source term  $\Xi_{\text{cg}} = Q_{\text{cg}}/(L_N T_0)$  as in Eq. (35), we find:

$$a_{\text{cg}} = \frac{V_p a_p}{A_p d L_N T_0}, \quad (48)$$

$$b_{\text{cg}} = \frac{V_p b_p}{A_p d L_N T_0}. \quad (49)$$

We see that the coarse-grained coefficients scale inversely with the interparticle spacing  $d$  (denser packing  $\rightarrow$  higher effective heating) and inversely with the assembly-scale loss coefficient  $L_N$ . Note that the ratio  $a_{\text{cg}}/b_{\text{cg}} = a_p/b_p$  is independent of the coarse-graining procedure.

The nanoscale loss term  $-\beta\theta$  in Eq. (18) represents direct environmental coupling at short length scales ( $\sim d$ )

and short times ( $\sim t_d$ ). After spatial and temporal averaging, this term contributes to the assembly-scale loss  $-\Theta$  in Eq. (35), but with a renormalized coefficient.

To derive the relationship explicitly, consider the average loss rate over the coarse-graining volume:

$$\langle \text{Loss rate} \rangle = \frac{1}{\ell_{\text{cg}}} \int L_m [T(x) - T_0] dx = L_m [T_{\text{cg}} - T_0]. \quad (50)$$

However, at larger scales, additional loss mechanisms become active:

1. **Boundary losses:** When the thermal field extends to the system edges ( $x \sim 0, L$ ), heat leaks through the boundaries at a rate  $\sim \kappa_{\text{eff}} \nabla T / L$ .
2. **Enhanced convective coupling:** At larger scales, collective thermal gradients drive more efficient heat transfer to the environment.
3. **Radiation losses:** For elevated temperatures (not relevant here), radiative losses  $\propto T^4$  become significant.

These emergent mechanisms contribute an additional loss coefficient  $L_{\text{emergent}}$ , so that the total assembly-scale loss is:

$$L_N = L_m + L_{\text{emergent}}. \quad (51)$$

**Order-of-magnitude estimate:** For the systems studied here,  $L_m \sim 10^4\text{--}10^5 \text{ W m}^{-3} \text{ K}^{-1}$  (nanoscale direct losses), while  $L_N \sim 10^5\text{--}10^7 \text{ W m}^{-3} \text{ K}^{-1}$  (assembly-scale total losses), giving  $L_N/L_m \sim 10\text{--}100$ , which means that the emergent losses dominate at larger scales and longer times.

We can easily check that the coarse-graining procedure preserves the dimensional consistency.

In summary, the coarse-grained assembly-scale description emerges from the nanoscale formulation through:

1. **Temporal averaging** over  $\Delta t$  (Eq. 41), filtering out AC oscillations and nanomagnet-scale transients.
2. **Spatial averaging** over  $\ell_{\text{cg}}$  (Eq. 45), replacing discrete sources by volumetric densities.
3. **Parameter mapping:** Nanoscale coefficients ( $a_p, b_p, L_m$ ) are related to assembly-scale coefficients ( $a_{\text{cg}}, b_{\text{cg}}, L_N$ ) via Eqs. (48)–(51).
4. **Emergent losses:** The assembly-scale loss  $L_N$  incorporates both direct nanoscale losses  $L_m$  and additional losses  $L_{\text{emergent}}$  that arise at larger scales.

This explicit derivation clarifies that the two-scale framework is not merely a heuristic separation, but a systematic coarse-graining procedure with well-defined approximations. In Section V F, we quantify the accuracy of this approximation by comparing full nanoscale computations with assembly-scale predictions.

#### D. Local-to-global heating crossover (L2GHC): indicators and conditions

The transition from local to global heating is a central feature of thermal transport in nanomagnet assemblies under alternating magnetic fields. At short times and small scales, heating is confined to the immediate vicinity of each nanomagnet, creating localized hot spots ideal for targeted processes such as nanoscale catalysis or site-specific activation. As time progresses and thermal diffusion couples neighboring sources, the temperature field evolves toward spatial homogenization, resulting in collective heating suitable for applications such as magnetic hyperthermia or bulk thermal actuation.

The efficiency and controllability of such systems depend critically on the competition between heat injection, diffusion, and thermal leakage—quantified by parameters such as particle spacing  $d$ , interfacial coupling  $\gamma$ , matrix conductivity  $\kappa_m$ , and the thermo-magnetic feedback coefficient  $b$ . Understanding and mapping the crossover conditions allows for the rational design of materials in which heating can be tuned from highly localized to uniformly global, optimizing therapeutic efficacy while minimizing unwanted thermal spread.

##### 1. Analytical stability criterion

The crossover from local to global heating is fundamentally a stability transition of the temperature field. In the linearized regime, the dynamics of the modal amplitudes  $\mathbf{c}(\tau)$  are governed by the matrix  $\mathbf{B}$  defined in Eqs. (27, 28). The eigenvalues of  $\mathbf{B}$  determine the growth or decay of thermal modes.

The system crosses from localized to global heating when the most unstable mode becomes marginally stable:

$$\max[\text{Re}(\text{eig}(\mathbf{B}))] = 0. \quad (52)$$

For the fundamental Dirichlet mode ( $r = 1$ ), the diagonal element of  $\mathbf{B}$  reads<sup>1</sup>

$$B_{11} = -(\lambda_1 + \beta) + \tilde{b} \frac{2}{\Lambda} \sum_{n=0}^{N-1} \sin^2\left(\frac{\pi \xi_n}{\Lambda}\right), \quad \lambda_1 = \left(\frac{\pi}{\Lambda}\right)^2. \quad (53)$$

Setting  $B_{11} = 0$  yields the critical feedback coefficient

$$\tilde{b}_c = \frac{\lambda_1 + \beta}{\frac{2}{\Lambda} \sum_{n=0}^{N-1} \sin^2\left(\frac{\pi \xi_n}{\Lambda}\right)}. \quad (54)$$

The sign of  $\tilde{b}_c$  is strictly positive. Indeed, diffusion losses ( $\lambda_1$ ) and Newton losses ( $\beta$ ) must be compensated

<sup>1</sup>See Appendix B for NBC.

by a positive thermo-magnetic feedback before the uniform mode can grow. The crossover is therefore accessible only when the renormalized coefficient  $\tilde{b}$  is itself positive.

The sign of  $\tilde{b}$  is not, however, determined solely by the bare SLP coefficient  $b_p$  whose sign in turn depends on several system parameters [see Appendix A and Fig. 14]. From the renormalization (19),

$$\tilde{b} = \frac{\gamma}{\gamma - \varepsilon} b = \Upsilon_0 \frac{\gamma_s b_p}{\gamma_s - b_p}, \quad (55)$$

where  $\gamma_s = h_s A_p T_0 / V_p > 0$  is the interfacial coupling coefficient and  $\Upsilon_0 > 0$  [see Eq. (21)]. Since  $\Upsilon_0$  is strictly positive, the sign of  $\tilde{b}$  is determined entirely by the ratio  $\gamma_s b_p / (\gamma_s - b_p)$ , i.e. by the relative magnitude of the interfacial coupling  $\gamma_s$  and the bare feedback coefficient  $b_p$ . Equivalently, in terms of the dimensionless quantities  $\gamma = \gamma_s / a_p$  and  $\varepsilon = b_p / a_p$ , the sign is controlled by  $\gamma$  relative to  $\varepsilon$ . Then, three cases may arise:

1.  $b_p < 0$  (self-limiting bare SLP):  $\tilde{b} < 0$ . The sign is preserved by renormalization.
2.  $b_p > 0$  and  $\gamma_s > b_p$  (self-amplifying SLP, strong interfacial coupling):  $\tilde{b} > 0$ . The positive feedback couples effectively into the matrix.
3.  $b_p > 0$  and  $\gamma_s < b_p$  (self-amplifying SLP, weak interfacial coupling):  $\tilde{b} < 0$ . Physically, the interfacial thermal resistance is so large that the self-amplifying feedback cannot couple efficiently into the matrix temperature field; at the matrix level the effective feedback appears self-limiting.

Three limiting values of  $\gamma_s$  clarify the role of the nanomagnet–matrix interface.

*No interfacial resistance (baseline model).* The most direct formulation of the nanomagnet-chain heat equation is obtained by writing the source term with the bare SLP coefficients,  $[a_p + b_p \theta(\xi_n)] \delta(\xi - \xi_n)$ , without introducing the interfacial boundary condition (6) at all. In this case the renormalization (19) is not needed and the entire stability analysis of the present section applies with  $b_p$  in place of  $\tilde{b}$ . The crossover criterion (54) becomes simply  $b_p > \tilde{b}_c$ . Within the renormalized theory, this baseline model is recovered formally in the perfect-contact limit  $h_s \rightarrow \infty$  ( $\gamma_s \rightarrow \infty$ ), where Eqs. (19) give  $\tilde{a} \rightarrow a$  and  $\tilde{b} \rightarrow b$ . The interfacial boundary condition (6) and the associated renormalization are thus a refinement of this baseline, introducing the richer structure discussed in the following two limiting cases.

*Decoupled limit* ( $\gamma_s \rightarrow 0$ ). In the opposite extreme,  $h_s \rightarrow 0$  and the nanomagnet–matrix interface becomes thermally insulating. Equations (19) give  $\tilde{a} \rightarrow 0$  and  $\tilde{b} \rightarrow 0$ , so the source term in the matrix heat equation (18) vanishes identically. The nanomagnet still dissipates power internally, but the infinite interfacial resistance traps all heat inside the nanomagnet; the matrix temperature field remains at ambient regardless of

the values of  $a_p$  and  $b_p$ . No heating—neither local nor global—can develop in the embedding medium in this limit.

*Resonant limit* ( $\gamma_s \rightarrow b_p^+$ , for  $b_p > 0$ ). When  $\gamma_s$  approaches  $b_p$  from above, the denominator  $\gamma_s - b_p \rightarrow 0^+$  and both  $\tilde{a}$  and  $\tilde{b}$  diverge. Physically, the rate at which the interface extracts heat from the nanomagnet exactly matches the self-amplifying feedback: the nanomagnet temperature grows without bound in the linearized model, signaling the breakdown of the first-order Taylor expansion of the SLP before any collective matrix-level instability is reached. For  $\gamma_s < b_p$  the renormalized coefficients change sign (case 3 above), but the linearized framework is only quantitatively reliable for  $\gamma_s$  sufficiently far from  $b_p$ . In practice, the divergence at  $\gamma_s = b_p$  is regularized by higher-order (nonlinear) terms in the SLP, which saturate the nanomagnet temperature at a finite value.

The interplay between  $b_p$  and  $\gamma_s$  thus governs not merely the magnitude of  $\tilde{b}$  but its sign, and thereby determines whether the local-to-global crossover is accessible at all.

Finally, combining these observations with the stability criterion (54), we identify three physical regimes for the temperature field:

- **Unconditionally stable (localized) regime** ( $\tilde{b} \leq 0$ , i.e.  $b_p < 0$ , or  $b_p > 0$  with  $\gamma_s < b_p$ ). Both terms in  $B_{11}$  are non-positive;  $\mathbf{B}$  is negative definite for all  $|\tilde{b}|$ . The temperature field remains localized and spatially heterogeneous. No crossover to global heating is possible regardless of nanomagnet density or geometry.
- **Sub-critical amplifying regime** ( $0 < \tilde{b} < \tilde{b}_c$ ). The positive feedback partially compensates diffusion and Newton losses. The system is still stable, but as  $\tilde{b} \rightarrow \tilde{b}_c^-$  the fundamental-mode decay rate  $|B_{11}| \rightarrow 0$ : thermal modes become long-lived, the temperature grows quasi-linearly, and spatial correlations extend over multiple interparticle spacings.
- **Super-critical regime** ( $\tilde{b} > \tilde{b}_c$ ). The positive feedback overcomes all loss channels. The fundamental mode grows exponentially, driving the temperature field toward spatially homogeneous, collective heating at the assembly scale. In practice, nonlinear saturation of the SLP (higher-order terms in the Taylor expansion) arrests the growth and sets the final steady-state temperature.

Equation (54) therefore encodes a *dual* condition for the local-to-global crossover: i) the bare SLP must be self-amplifying ( $b_p > 0$ , controlled by the nanomagnet size  $D$ , field amplitude  $h_0$ , frequency  $f$ , and interparticle spacing; cf. Fig. 14 in Appendix A), and ii) the interfacial coupling must be strong enough ( $\gamma_s > b_p$ ) for the positive feedback to survive renormalization into the matrix. In the perfect-contact limit ( $\gamma_s \rightarrow \infty$ ), or equivalently in

the baseline model where the interfacial boundary condition (6) is not imposed, the second condition is automatically satisfied and the crossover is controlled by  $b_p$  alone. When either condition fails—whether because  $b_p < 0$ , owing to  $\gamma_s < b_p$ , or in the decoupled limit  $\gamma_s \rightarrow 0$  where the matrix receives no heat at all—the system is locked into the localized-heating regime.

## 2. Physical indicators of the crossover

To quantify the transition in practice, we introduce complementary scalar and spatial indicators derived from the temperature field  $\theta(\xi, \tau)$ .

- **Mean temperature** (global indicator):

$$\langle \theta \rangle(\tau) = \frac{1}{\mathcal{N}} \sum_{n=0}^{\mathcal{N}-1} \theta(\xi_n, \tau), \quad (56)$$

which in steady state ( $\tau \rightarrow \infty$ ) is given by

$$\langle \theta \rangle_{\text{ss}} = \frac{\tilde{a} \mathbf{1}^\top \mathbf{K}_R(0) [\mathbf{I} - \tilde{b} \mathbf{K}_R(0)]^{-1} \mathbf{1}}{\mathcal{N}}.$$

A sharp rise in  $\langle \theta \rangle_{\text{ss}}$  as  $\tilde{b}$  approaches  $1/\lambda_{\max}(\mathbf{K}_R(0))$  signals the onset of collective heating.

- **Temperature variance** (local heterogeneity indicator):

$$\text{Var}_\tau(\theta) = \frac{1}{\mathcal{N}} \sum_{n=0}^{\mathcal{N}-1} [\theta(\xi_n, \tau) - \langle \theta \rangle(\tau)]^2, \quad (57)$$

which measures spatial inhomogeneity. In the local-heating regime, the variance is large due to distinct hot spots; in the global-heating regime, diffusion and boundary conditions homogenize the temperature, driving the variance toward zero.

- **Thermal correlation length** (spatial coherence indicator): The two-point spatial correlator

$$C(\Delta\xi, \tau) = \langle \theta(\xi, \tau) \theta(\xi + \Delta\xi, \tau) \rangle_\xi$$

can be expanded in the modal basis as

$$C(\Delta\xi, \tau) = \sum_{r=1}^{\infty} |c_r(\tau)|^2 \phi_r(0) \phi_r(\Delta\xi). \quad (58)$$

From this, a thermal correlation length is defined via the first moment:

$$\xi_{\text{corr}}(\tau) = \frac{\int_0^\Lambda \Delta\xi C(\Delta\xi, \tau) d\Delta\xi}{\int_0^\Lambda C(\Delta\xi, \tau) d\Delta\xi}.$$

Growth of  $\xi_{\text{corr}}$  beyond the interparticle spacing ( $\xi_{\text{corr}} \gtrsim 1$ ) signals the emergence of collective, assembly-scale heating.

Together, these indicators provide a multifaceted view of the local-to-global crossover, linking the analytical stability criterion to observable thermal statistics. Their behavior across parameter space is illustrated numerically in Sec. V.

## 3. Role of boundary conditions: Dirichlet versus Neumann

The stability analysis and crossover indicators discussed above assume Dirichlet boundary conditions (DBC),  $\theta(0, \tau) = \theta(\Lambda, \tau) = 0$ , modelling a chain terminated by ideal thermal baths. However, alternative boundary conditions alter the modal spectrum and can qualitatively change both the absolute temperature levels and the spatial structure of the temperature field<sup>60,61</sup>. We summarize here the main results for the opposite limiting case—homogeneous Neumann (no-flux) conditions (NBC),  $\partial_\xi \theta|_{\xi=0, \Lambda} = 0$ —which models thermally insulated chain ends. Full derivations are given in Appendix B.

The Neumann eigenfunctions are cosines,  $\phi_r^{(N)}(\xi) = \sqrt{2/\Lambda} \cos(r\pi\xi/\Lambda)$  for  $r \geq 1$ , supplemented by the spatially uniform zero mode  $\phi_0^{(N)} = 1/\sqrt{\Lambda}$  with eigenvalue  $\lambda_0^{(N)} = 0$ . This zero mode—absent from the Dirichlet spectrum, where  $\lambda_1^{(D)} = (\pi/\Lambda)^2 > 0$ —is the structural feature responsible for all qualitative differences between the two boundary conditions, see Section V.

*Stability.* The zero-mode growth rate in the diagonal approximation is  $-\beta + \mathcal{N} \tilde{b}/\Lambda$ . The corresponding critical feedback coefficient,

$$\tilde{b}_c^{(0)} = \frac{\beta \Lambda}{\mathcal{N}}, \quad (59)$$

vanishes as  $\beta \rightarrow 0$ . So, with insulated boundaries (NBC) and negligible volumetric losses, *any* positive feedback—however small—destabilises the uniform temperature channel. By contrast, the Dirichlet critical value (54) remains finite even for  $\beta = 0$ , because the boundary heat sinks provide diffusive stabilisation through  $\lambda_1^{(D)} > 0$ . The Neumann system is therefore generically less stable. In the physically relevant regime ( $\tilde{b} < 0$ ,  $\beta > 0$ ), both systems are unconditionally stable, but their steady-state properties differ markedly.

*Steady state and the background effect.* The zero mode contributes a spatially uniform temperature offset to the Neumann steady state [see Appendix B],

$$\theta_{\text{ss}}^{(N)}|_{r=0} = \frac{\tilde{a} \mathcal{N}/\Lambda}{\beta - \tilde{b} \mathcal{N}/\Lambda}, \quad (60)$$

which, for  $\beta \ll |\tilde{b}| \mathcal{N}/\Lambda$ , simplifies to  $\tilde{a}/|\tilde{b}|$ —independent of system size and loss parameter. No analogous contribution exists under DBC, where  $\theta$  vanishes at the boundaries. Consequently, the absolute NBC temperature exceeds the DBC value at every interior point; the difference is dominated by the zero-mode term  $1/(\Lambda\beta)$  in the diagonal Green's function [Eq. (B31) in Appendix B].

*Spatial heterogeneity.* Because the zero mode is spatially uniform, it cancels exactly in the hotspot contrast  $\Delta\theta_n$  (defined as the difference between a nanomagnet-site temperature and its inter-site baseline), which is governed entirely by the  $r \geq 1$  modes common to both spectra. Interior hotspot contrasts are therefore comparable under DBC and NBC. However, the *relative* spatial variance  $\mathcal{V}_{\text{rel}} = \text{Var}(\theta_{\text{ss}})/\langle\theta_{\text{ss}}\rangle^2$  is strongly suppressed under NBC, because the zero-mode pedestal inflates the mean while leaving the variance (set by  $r \geq 1$  modes) essentially unchanged:  $\mathcal{V}_{\text{rel}}^{(\text{N})} \ll \mathcal{V}_{\text{rel}}^{(\text{D})}$  when  $\beta \ll |\tilde{b}|\mathcal{N}/\Lambda$ . This is the central trade-off: *NBC maximises absolute temperature at the cost of washing out spatial heterogeneity, while DBC preserves strong spatial contrast at the cost of lower absolute temperatures.*

*Boundary nanomagnet activity.* Under DBC, the two boundary nanomagnets ( $n = 0$  and  $n = \mathcal{N} - 1$ ) are thermally invisible: the sine eigenfunctions vanish at  $\xi = 0$  and  $\xi = \Lambda$ , so these particles do not contribute to the modal source vector or coupling matrix. Under NBC, the cosine eigenfunctions attain their extremal values at the boundaries, so all  $\mathcal{N}$  particles are thermally active.

*Design implications.* Real systems are likely intermediate between these two limits, described by Robin boundary conditions with an effective Biot number  $\text{Bi}_b = h_b d / \kappa_m$  interpolating between  $\text{Bi}_b \rightarrow \infty$  (Dirichlet) and  $\text{Bi}_b \rightarrow 0$  (Neumann). The analysis shows that conducting boundaries ( $\text{Bi}_b \gg 1$ ) favour applications requiring maximum spatial contrast (e.g. site-selective activation), while insulating boundaries ( $\text{Bi}_b \ll 1$ ) favour those requiring maximum absolute temperature (e.g. bulk hyperthermia). These conclusions apply equally to the crossover indicators introduced above: under NBC, the correlation length  $\xi_{\text{corr}}$  saturates rapidly at the system size once the zero mode dominates, and the variance-to-mean ratio drops considerably compared to DBC. Numerical illustrations for both boundary conditions are presented in the Results Sec. V.

#### IV. PHYSICAL PARAMETERS AND SCALING

For numerical convenience, we introduced in Sec. III the dimensionless formulation of the thermal problem in terms of a compact set of control parameters. To connect this formulation to real experimental systems, we provide explicit scaling relations between these dimensionless parameters and physical material properties, geometric arrangements, and excitation conditions. This mapping is essential for interpreting the results in Sec. V and for designing experiments aimed at observing the local-to-global heating crossover.

##### A. Parameter hierarchy

We distinguish three levels of parameters: (i) *raw input parameters*, directly measurable or independently

tunable quantities that define the experimental system; (ii) *inferred physical parameters*, derived from raw inputs via constitutive relations (magnetic response, thermal transport); and (iii) *dimensionless control parameters*, the final scaled variables governing the heat equations.

From the raw inputs, the specific loss power (SLP) is obtained from linear-response theory including dipolar interactions, as detailed in Appendix A. The key outputs are the dimensional coefficients  $a_p$  and  $b_p$  appearing in the linearized heating law (12), which depend on the reduced anisotropy barrier  $\sigma_0 = KV_p/(k_B T_0)$ , the reduced frequency  $\varpi_0 = \omega\tau_0$ , the dipolar coupling strength (renormalized by  $2KV_p$ )

$$\lambda = \frac{\mu_0}{4\pi} \frac{M_s^2 V_p^2}{d^3} \frac{1}{2KV_p}, \quad (61)$$

and the field amplitude  $h_0$ . Their explicit expressions are given in Eqs. (A2)–(A3).

The dimensionless parameters entering the nanomagnet-scale and assembly-scale heat equations were introduced in Sec. III; here we collect the definitions and explain how they are evaluated from the raw inputs above.

The nanomagnet-scale coefficients  $a = \Upsilon_0 a_p$  and  $b = \Upsilon_0 b_p$ , with the scaling prefactor  $\Upsilon_0$  defined in Eq. (21), set the baseline heating strength and the thermo-magnetic feedback. The dimensionless interfacial coupling  $\gamma$  and ratio  $\varepsilon$  [Eq. (15)], together with the interfacial coupling strength  $\gamma_s = A_p h_s T_0 / V_p$ , determine the renormalized coefficients  $\tilde{a}$  and  $\tilde{b}$  [Eq. (19)], which reduce to  $a$  and  $b$  in the strong interfacial coupling limit  $\gamma \gg |\varepsilon|$ . The nanoscale loss parameter  $\beta = L_m t_d / (\rho_m c_{v,m})$  captures environmental coupling at the nanomagnet level, while the diffusive coupling  $\zeta$  [Eq. (36)] and the system size  $\Lambda = L/d$  complete the nanomagnet-scale description.

At the assembly scale, the discrete delta-function sources are replaced by an effective volumetric heating density after spatial averaging over  $\ell_{\text{cg}} \gg d$  [Eq. (35)]. For a uniform chain of identical nanomagnets, the coarse-grained source density is  $(V_p/A_p) a_p/d$ , and the linearized source term (37) yields the coarse-grained coefficients

$$a_{\text{cg}} = \frac{a}{\beta_N}, \quad b_{\text{cg}} = \frac{b}{\beta_N}, \quad \beta_N \equiv \frac{L_N t_d}{\rho_m c_{v,m}} = \frac{L_N d^2}{\kappa_m}. \quad (62)$$

Here  $\beta_N$  is the assembly-scale analogue of  $\beta$ : it measures the ratio of the diffusion time  $t_d$  to the assembly-scale leakage time  $t_s \simeq \rho_m c_{v,m} / L_N$ . Because  $L_N \gg L_m$  (the hierarchical relation discussed in Sec. III B), we have  $\beta_N / \beta = L_N / L_m \gg 1$ , so  $a_{\text{cg}}$  and  $b_{\text{cg}}$  are parametrically smaller than  $a/\beta$  and  $b/\beta$ , respectively, but typically of order unity or larger.

## B. Reference parameter set

Table I lists the reference values used for the magnetite–PMMA system, by way of illustration, throughout Sec. V. These values are representative of typical nanocomposites used in magnetic hyperthermia studies. For the reference set,  $\sigma_0 \simeq 6.6$  places the NM in the intermediate barrier regime, with  $\eta_0 \simeq 0.37$  and  $b_p < 0$  (self-limiting heating, cf. Appendix A). The interfacial coupling is moderate ( $\gamma \simeq 2.5$ ), so the renormalization (19) is significant:  $\tilde{a}$  is reduced by about a factor of 3 relative to  $a$ . The system lies in the unconditionally stable regime ( $\tilde{b} < 0$ , cf. Sec. III D 1).

The coarse-grained coefficients  $a_{\text{cg}} \simeq 11$  and  $b_{\text{cg}} \simeq -66$  reflect the large ratio of source power to assembly-scale losses:  $\langle a_p \rangle_{\text{cg}} / (L_N T_0) \gg 1$ .

*Case studies.* Table II contrasts two representative configurations, both using the same nanomagnet ( $D = 12$  nm magnetite) but differing in matrix environment and geometric packing.

- The aqueous ferrofluid ( $d/D = 5$ ) has high matrix conductivity, strong interfacial coupling ( $\gamma \simeq 4.4 \times 10^4$ , so  $\tilde{a} \simeq a$ ), and large environmental losses ( $\beta$  an order of magnitude above the reference,  $L_N/L_m = 50$ ). The dilute packing and efficient heat removal favor the localized-heating regime.
- The reference PMMA nanocomposite ( $d/D = 3$ ) reproduces the parameter set of Table I. Here the interfacial coupling is moderate ( $\gamma \simeq 2.5$ ), making the renormalization significant:  $\tilde{a}$  is reduced by about a factor of 3 relative to  $a$ . The denser packing and lower matrix conductivity yield  $a_{\text{cg}} \simeq 11$ , promoting collective heating.

## C. Physical versus illustrative parameters

As discussed in the introduction, a single nanomagnet driven by an AC magnetic field dissipates heat, but the associated temperature perturbation is both *weak* (limited power per particle) and *rapidly homogenized* by diffusion in the embedding medium. The renormalized coefficients  $\tilde{a}_{\text{phys}}$  and  $\tilde{b}_{\text{phys}}$  for the reference magnetite–PMMA system are of order  $10^{-8}$ – $10^{-9}$ , reflecting this extreme weakness of individual nanomagnet heating relative to thermal diffusion. Under these physical conditions local temperature peaks at source sites (hotspots) are unresolvable: the dimensionless temperature field is dominated by the lowest spatial modes and thermal heterogeneity is suppressed by factors of  $10^8$  or more.

*Single-particle scales (energy, diffusion time, AC cycles).* We recall from the introduction that, for a spherical nanomagnet of radius  $R \sim 10$  nm, the energy needed to raise its temperature by  $\Delta T \sim 1$  K is

$$E_{1\text{K}} \sim \rho_{\text{NP}} c_{p,\text{NP}} \frac{4\pi R^3}{3} (1\text{K}) \simeq 10^{-17}\text{--}10^{-16}\text{J}. \quad (63)$$

TABLE I: Reference physical and dimensionless parameters for the magnetite–PMMA nanocomposite.

Parameter	Symbol	Value
<b>Nanoparticle properties</b>		
Diameter	$D$	12.0 nm
Volume	$V_p$	$9.05 \times 10^{-25} \text{ m}^3$
Density	$\rho_p$	$5200 \text{ kg/m}^3$
Saturation magn.	$M_s$	480 kA/m
Anisotropy constant	$K$	$30 \text{ kJ/m}^3$
Attempt time	$\tau_0$	$1.0 \times 10^{-9} \text{ s}$
<b>Geometric arrangement</b>		
Interparticle spacing	$d$	36.0 nm
System length	$L$	$1.98 \mu\text{m}$
Number of NMs	$\mathcal{N}$	56
<b>Thermal properties</b>		
Matrix conductivity	$\kappa_m$	$0.2 \text{ W/(m}\cdot\text{K)}$
Matrix heat capacity	$\rho_m c_{v,m}$	$2.21 \times 10^6 \text{ J/(m}^3\cdot\text{K)}$
Base temperature	$T_0$	300 K
Interfacial coeff.	$h_s$	$0.33 \text{ W/(m}^2\cdot\text{K)}$
Nanoscale loss coeff.	$L_m$	$3.0 \times 10^3 \text{ W/(K}\cdot\text{m}^3)$
Assembly-scale loss	$L_N$	$3.3 \times 10^5 \text{ W/(K}\cdot\text{m}^3)$
<b>AC magnetic field</b>		
Amplitude	$h_0$	38.2 kA/m
Frequency	$f$	194 kHz
<b>Inferred magnetic parameters</b>		
Reduced anisotropy	$\sigma_0$	6.55
Reduced frequency	$\varpi_0$	$1.22 \times 10^{-3}$
Dipolar strength	$\lambda$	0.0074
<b>Dimensionless control parameters</b>		
Baseline heating	$a$	$2.38 \times 10^{-8}$
Feedback coefficient	$b$	$-1.41 \times 10^{-7}$
Interfacial coupling	$\gamma$	2.50
Renormalized baseline	$\tilde{a}$	$7.05 \times 10^{-9}$
Renormalized feedback	$\tilde{b}$	$-4.18 \times 10^{-8}$
Nanoscale loss	$\beta$	$1.94 \times 10^{-11}$
Diffusive coupling	$\zeta$	$1.55 \times 10^5$
System size	$\Lambda$	55
CG baseline	$a_{\text{cg}}$	11.1
CG feedback	$b_{\text{cg}}$	-65.8

Yet the surrounding medium (water/polymers,  $\alpha \sim 10^{-7} \text{ m}^2/\text{s}$ ) diffuses heat away on the nanoscale time

$$\tau_{\text{diff}} \sim \frac{R^2}{\alpha} \sim 10^{-9} \text{ s}. \quad (64)$$

Comparing  $\tau_{\text{diff}}$  with the AC period  $T = 1/f$  gives

$$N_{\text{cyc}} \sim f\tau_{\text{diff}} \ll 1 \quad (f \sim 10^5 \text{ Hz} \Rightarrow N_{\text{cyc}} \sim 10^{-4}), \quad (65)$$

so nanoscale gradients relax within a small fraction of a single cycle. In the time-averaged (quasi-steady) picture a localized power  $P$  yields the far-field scaling

TABLE II: Case studies: aqueous ferrofluid vs. reference PMMA nanocomposite (Table I). Both use  $D = 12$  nm magnetite,  $L = 1.98 \mu\text{m}$ ,  $h_0 = 38.2$  kA/m,  $f = 194$  kHz.

Parameter	Ferrofluid	Reference PMMA
<b>Physical parameters</b>		
$d/D$	5	3
$\kappa_m$ (W/mK)	0.6	0.2
$\rho_m c_{v,m}$ ( $10^6$ J/m <sup>3</sup> K)	4.19	2.21
$h_s$ (W/m <sup>2</sup> K)	5000	0.33
$L_m$ ( $10^3$ W/Km <sup>3</sup> )	20.0	3.0
$L_N$ ( $10^5$ W/Km <sup>3</sup> )	10.0	3.3
<b>Dimensionless parameters</b>		
$a$	$1.14 \times 10^{-8}$	$2.38 \times 10^{-8}$
$b$	$-7.05 \times 10^{-8}$	$-1.41 \times 10^{-7}$
$\gamma$	$4.4 \times 10^4$	2.50
$\tilde{a}$	$1.14 \times 10^{-8}$	$7.05 \times 10^{-9}$
$\tilde{b}$	$-7.04 \times 10^{-8}$	$-4.18 \times 10^{-8}$
$\beta$	$1.20 \times 10^{-10}$	$1.94 \times 10^{-11}$
$\zeta$	$1.50 \times 10^5$	$1.55 \times 10^5$
$\Lambda$	33	55
$a_{\text{cg}}$	1.89	11.1
$b_{\text{cg}}$	-11.7	-65.8

TABLE III: Illustrative parameter set used in the local-profile figures (Sec. V), compared with the physical values from Table I.

Parameter	Physical	Illustrative	Ratio
$\tilde{a}$	$7.05 \times 10^{-9}$	0.4	$5.7 \times 10^7$
$\tilde{b}$	$-4.18 \times 10^{-8}$	-0.5	$1.2 \times 10^7$
$\beta$	$1.94 \times 10^{-11}$	0.015	$7.7 \times 10^8$

$\Delta T(r) \sim P/(4\pi\kappa r)$  for  $r \gtrsim R^1$ , so local contrasts decay rapidly with distance; conversely, maintaining  $\Delta T(a) \sim 1$  K would require  $P \sim 4\pi k a \Delta T \sim 10^{-7}$  W for  $k \sim 0.6$  W/(mK), corresponding to unrealistically large per-particle SLP. The key message is therefore not that local peaks are absent, but that under realistic conditions they are *too small and too fast* to appear as resolved hotspots in mesoscale profiles.

*Orders-of-magnitude gap and design criteria.* To render the analytical structure of the solution visible—the cusp-like peaks at source sites, the edge–bulk asymmetry imposed by boundary conditions, and the localized-to-diffuse heating crossover—we employ an illustrative

<sup>1</sup>In steady state and with spherical symmetry, the temperature field around a point source of power  $P$  embedded in an infinite medium of thermal conductivity  $\kappa$  satisfies  $\kappa \nabla^2 T + P \delta^{(3)}(\mathbf{r}) = 0$ . For  $r > 0$  this reduces to  $(1/r^2) d(r^2 dT/dr)/dr = 0$ , whose general solution vanishing at infinity is  $T = C/r$ . The constant  $C$  is fixed by energy conservation: the total power conducted outward through any sphere of radius  $r$  must equal  $P$ , i.e.  $P = -\kappa(dT/dr) 4\pi r^2 = 4\pi\kappa C$ , giving  $\Delta T(r) = P/(4\pi\kappa r)$ .

parameter set elevated by  $\sim 7$ – $9$  orders of magnitude relative to the physical values (Table III). These illustrative values are chosen so that (i) the dimensionless temperature field is of order unity, (ii) the system lies in the stable localized heating regime ( $\tilde{b} < \tilde{b}_c$ ), and (iii) the interplay between boundary conditions, interfacial coupling, and loss hierarchy is clearly legible. All qualitative features of the solution—including the crossover indicators and the DBC/NBC contrast—are independent of the absolute magnitude of the source coefficients.

*Assembly-scale perspective.* Real nanomagnet assemblies in water/polymer are expected to exhibit mainly a smooth, collective temperature rise governed by boundary exchange and low spatial modes<sup>33,52</sup>. The use of illustrative parameters should therefore best be viewed as a pedagogical step: they expose how localized heating imprints peaks at source locations before those features are washed out by diffusion and by averaging across many nanomagnets at the assembly scale. This amplification is a deliberate visualization device and does not affect the qualitative mechanism by which global heating emerges from many weak nanoscale sources.

In practice, in the following section we will apply *baseline-subtraction (or detrending) procedure* to remove the zero-mode pedestal (or background) and low-mode structure so as to expose the cusp-like peaks. Indeed, under the physical magnetite–PMMA parameters the dimensionless temperature field is dominated by the lowest spatial modes, which produce a smooth, slowly varying background of order  $10^{-6}$ ; the source-localised cusps sit on top of this background with amplitudes of order  $10^{-8}$ – $10^{-9}$ , rendering them invisible on a linear scale. Hence, to expose the local peak structure, *e.g.*, in Fig. 2, a local linear detrend is applied independently for each panel and each time snapshot. More precisely, within the plotting window centred on source  $\xi_s$ , a least-squares linear fit  $\hat{\theta}(\xi) = a_0 + a_1\xi$  is computed and subtracted, yielding the residual  $\delta\theta(\xi, \tau) = \theta(\xi, \tau) - \hat{\theta}(\xi)$ . This removes the contribution of all modes whose wavelength exceeds the window width (a few interparticle spacings) while preserving the cusp-like structure at  $\xi_s$ .

## V. RESULTS

Unless otherwise stated, all results presented in this section are obtained using the reference physical and dimensionless parameters summarized in Sec. IV and Table I, corresponding to a one-dimensional chain of magnetite nanoparticles embedded in a PMMA matrix.

The local-to-global heating crossover in nanomagnet assemblies is governed by the competition between heat injection, thermal diffusion, and environmental losses across multiple scales. At the nanomagnet scale, the renormalized feedback coefficient  $\tilde{b}$  (incorporating both magnetic feedback  $b$  and interfacial resistance via  $\gamma$ ) and the nanoscale loss parameter  $\beta$  determine the stability of localized hotspots. The analytical condition  $\tilde{b} = \tilde{b}_c$ ,

where  $\tilde{b}_c$  depends on both diffusion ( $\lambda_1$ ) and nanoscale losses ( $\beta$ ) as given in Eq. (54), provides a compact criterion for the onset of collective heating. However, how this transition manifests in space and time depends on the spatial arrangement of the heat sources, the efficiency of thermal coupling between them, and the loss mechanisms operating at different scales. In the following, we also vary the interparticle distance  $d$  as an organizing geometric parameter, as it directly reflects nanoparticle concentration and simultaneously controls thermal diffusion, dipolar interactions, and the dimensionless loss parameters. For any fixed geometry, equivalent transitions can also be induced by varying magnetic or excitation parameters through their impact on  $a$ ,  $b$ , and thereby  $\tilde{a}$ ,  $\tilde{b}$ ; the role of these additional control parameters is highlighted throughout the section.

*Raw versus inferred parameters.* We emphasize that only physically independent quantities are specified as raw input parameters in the numerical implementation. These include the nanomagnet properties ( $D$ ,  $K$ ,  $M_s$ ), the interparticle spacing  $d$ , the matrix thermal properties ( $\kappa_m$ ,  $\rho_m c_{v,m}$ ), the interfacial coefficient  $h_s$ , the nanoscale loss coefficient  $L_m$ , the assembly-scale loss coefficient  $L_N$ , and the AC-field parameters ( $h_0$ ,  $f_0$ ). All secondary quantities—in particular the dimensionless parameters  $\tilde{a}$ ,  $\tilde{b}$ ,  $\beta$ ,  $\gamma$ ,  $\zeta$ , and the characteristic times  $t_d$  and  $t_s$ —are then inferred from these raw parameters using the scaling relations defined in Sec. IV.

As detailed in Sec. IV C, we employ two parameter sets throughout this section: the physical magnetite, with PMMA coefficients, and an illustrative set elevated by several orders of magnitude, the latter being designed to make the source-localized structure of the temperature field, namely the cusp-like peaks, edge-bulk asymmetry, and the localized-to-diffuse crossover, directly visible in the figures.

### A. Local temperature profiles at source sites

In Fig. 1 and 2 we display the temperature field in the neighbourhood of three selected source sites, near the left boundary ( $\xi = 1$ ), at the chain centre ( $\xi = 28$ ), and near the right boundary ( $\xi = 54$ ), under DBC and NBC. Both figure pairs use the reference magnetite–PMMA chain geometry ( $\Lambda = 55$ ,  $\mathcal{N} = 56$ ,  $\Delta\xi = 1$ ); the illustrative set (Fig. 1) replaces the physical SLP coefficients by  $\tilde{a} = 0.4$ ,  $\tilde{b} = -0.5$ ,  $\beta = 0.015$  while keeping everything else identical, so that the only difference between the two figures is the magnitude of the source and loss terms.

As mentioned earlier, in Fig. 2, we used a baseline-subtraction (or detrending) procedure to remove the zero-mode pedestal (or background) and low-mode structure so as to expose the cusp-like peaks. On the other hand, we have applied no detrending to the illustrative profiles (Fig. 1), where the source peaks are directly visible without post-processing. Even after detrending, the peak amplitudes in Fig. 2 are of order  $10^{-8}$  (DBC) and

$10^{-9}$  (NBC), corresponding to absolute temperature excursions  $\delta T \sim 10^{-8} T_0 \sim 3 \mu\text{K}$  and  $\sim 0.3 \mu\text{K}$ , respectively. Note that since both figure pairs share identical chain geometry, the comparison isolates the sole effect of the 7–9 order-of-magnitude coefficient gap given in Table III of Sec. IV: under the illustrative set (Fig. 1),  $\theta$  is of order unity and no detrending is needed. The fact that the NBC detrended amplitude is one order of magnitude *smaller* than the DBC value is due to the fact that NBC produces a higher temperature field, but the zero-mode pedestal inflates the local linear trend, so that the residual peak-above-trend shrinks. Despite the dramatic scale difference, the qualitative features are identical across both parameter sets: cusp-like peaks at source sites, edge–bulk asymmetry under DBC, near-symmetric profiles under NBC, and monotonic growth with  $\tau$ . The physical profiles thus confirm the conclusion of Sec. IV C, namely that nanoscale thermal localisation, while mathematically exact, is physically unresolvable for individual nanomagnets under realistic conditions; the observable temperature rise emerges only through the collective action of the full assembly at the coarse-grained scale.

*Effects of the boundary condition.* Under DBC [Figs. 1 and 2, upper panels], the temperature vanishes at the chain ends and the peak envelope is approximately uniform across the interior, while the edge source ( $\xi = 1$ ) is visibly suppressed and asymmetrically truncated on the boundary side. We see that each source generates a cusp-like peak that decays within one or two interparticle spacings, though in the bulk the overlap of many such contributions builds a smooth background that grows with  $\tau$ . On the other hand, under NBC [Figs. 1 and 2, lower panels], the edge–bulk hierarchy is reversed. Indeed, the boundary sources produce the highest peaks, because the zero-flux condition reflects all diffusing heat inward, effectively doubling the local source strength at the chain ends. In addition, the interpeak baseline is lifted by the growing zero-mode background  $\phi_0^{(N)} = 1/\sqrt{\Lambda}$ , which accumulates heat without decay (Appendix B). In the illustrative case, the global peak temperature reaches  $\theta \simeq 0.51$  under NBC versus  $\simeq 0.42$  under DBC; however, the raised baseline reduces the peak-to-valley contrast, which is consistent with the suppression of relative spatial variance  $\mathcal{V}_{\text{rel}}^{(N)} \ll \mathcal{V}_{\text{rel}}^{(D)}$  derived in Appendix B. The bulk source profiles ( $\xi = 28$ ) display nearly identical cusp shapes under both boundary conditions, obviously confirming that the DBC/NBC distinction is primarily an edge and global-mode effect.

*Effect of interparticle separation.* In Fig. 3, we examine the dependence of the local profile shape on the interparticle spacing  $d$ , using the physical magnetite–PMMA parameter set at the central source ( $\xi_{\text{src}} = \Lambda/2$ ) and late time  $\tau = 100$  for three spacings:  $d = 36$ , 50, and 80 nm. Since  $\beta = L_m t_d / (\rho_m c_{v,m})$  and  $t_d = d^2 / \alpha_m$ , the Newton loss parameter scales as  $\beta \propto d^2$ , ranging from  $1.94 \times 10^{-11}$  at  $d = 36$  nm to  $9.60 \times 10^{-11}$  at  $d = 80$  nm. Simultaneously, the chain length in dimensionless units  $\Lambda = L/d$  decreases from 55.0 to 25.0 as  $d$  increases, thus reducing

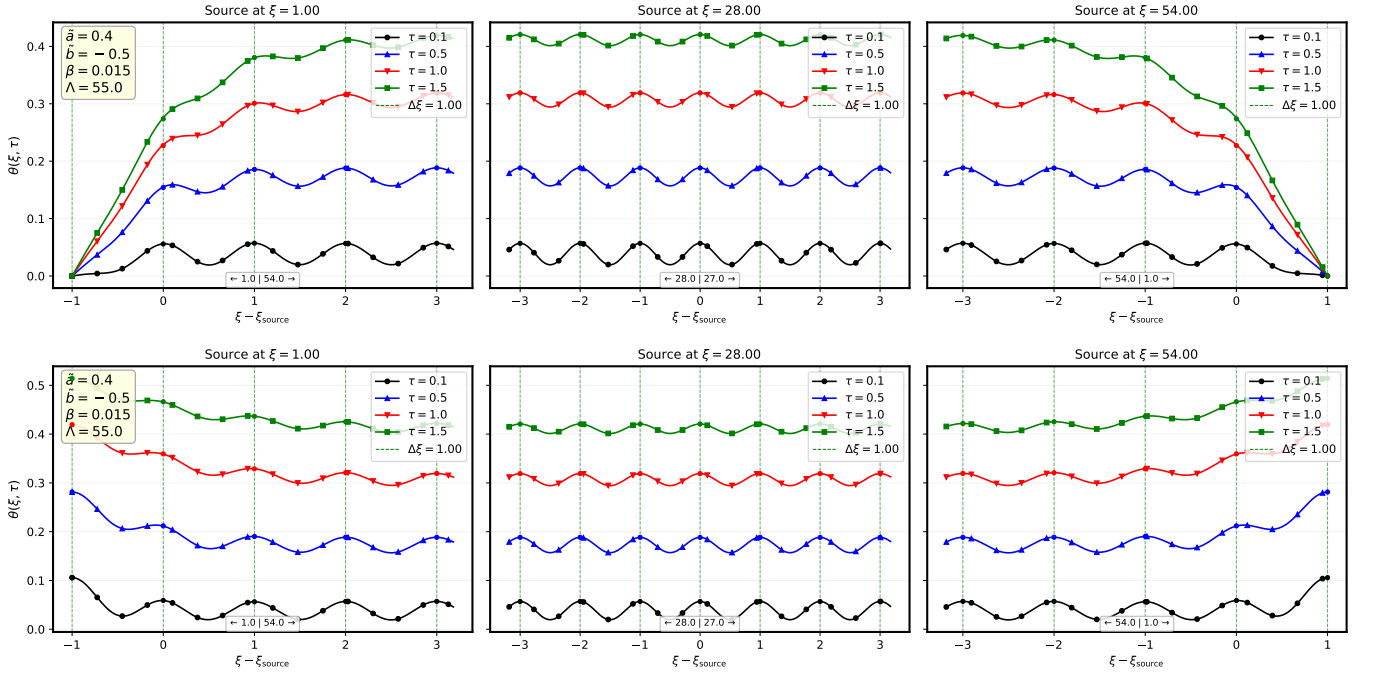


FIG. 1: Local temperature profiles  $\theta(\xi, \tau)$  around three source sites ( $\xi = 1, 28, 54$ ) at instants  $\tau = 0.1, 0.5, 1.0, 1.5$  for the illustrative parameter set (Table III). Vertical dashed lines mark the interparticle spacing  $\Delta\xi = 1$ . (Upper panel) Dirichlet BCs. (Lower panel) Neumann BCs.

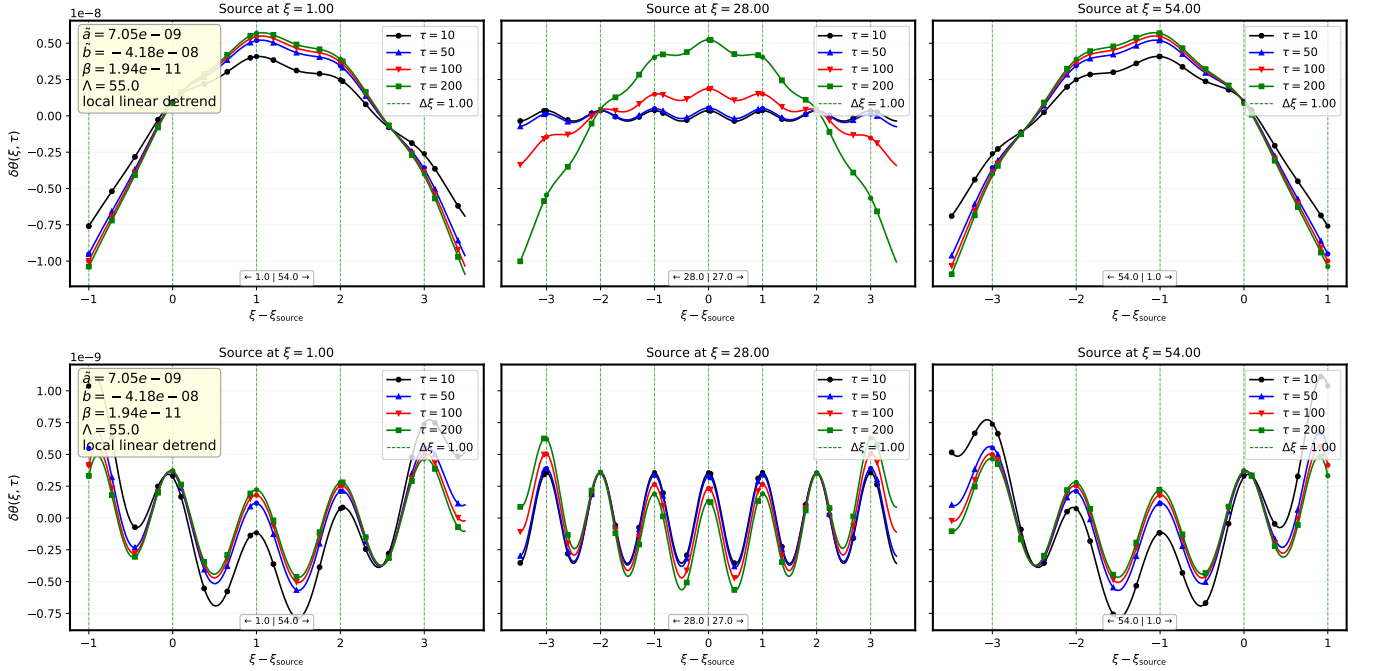


FIG. 2: Detrended local profiles  $\delta\theta(\xi, \tau)$  around three source sites ( $\xi = 1, 28, 54$ ) for the physical magnetite-PMMA parameter set (Table I) at  $\tau = 10, 50, 100, 200$ . (Upper panel) Dirichlet BCs. (Lower panel) Neumann BCs.

the number of sources from  $\mathcal{N} = 56$  to 26, while the chain physical length  $L$  remains fixed.

We see that, under DBC [Fig. 3, left panel], the detrended profile at  $d = 80$  nm (red curve) exhibits the

largest amplitude, with a broad, dome-shaped peak extending over several interparticle spacings. As  $d$  decreases, both the amplitude and the spatial extent of the peak shrink: at  $d = 36$  nm (black curve), the detrended

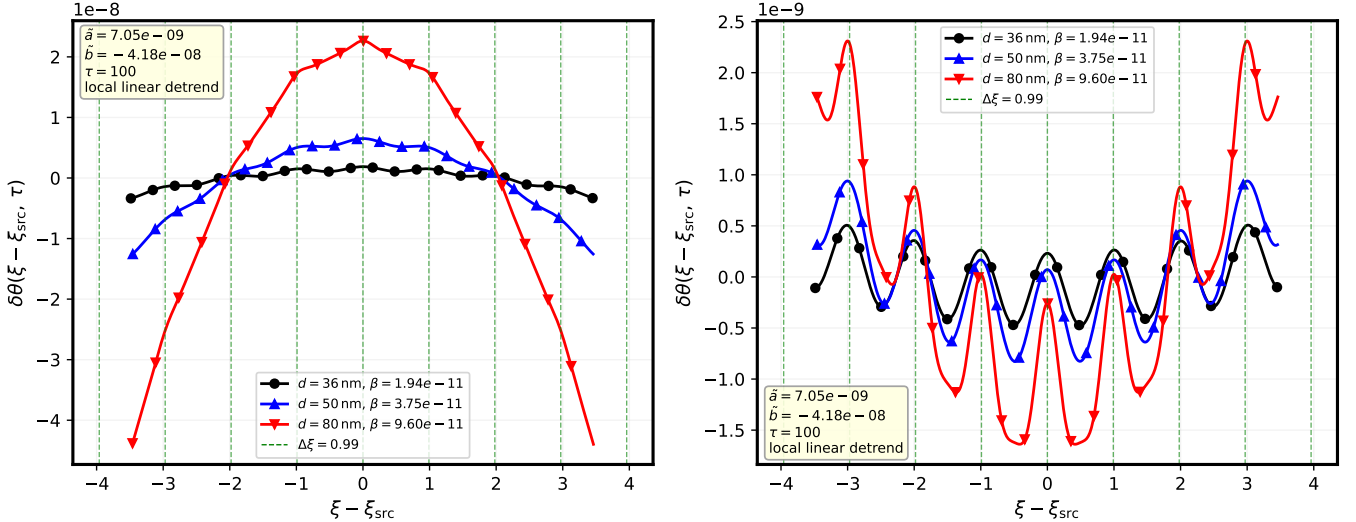


FIG. 3: Local profiles at the central source vs. interparticle separation  $d$ . Detrended profile  $\delta\theta(\xi - \xi_{\text{src}}, \tau)$  for the physical magnetite–PMMA parameter set (same as Fig. 2) at  $\tau = 100$ , for  $d = 36, 50, 80$  nm. Note that  $\beta \propto d^2$  and  $\Lambda = L/d$  vary with  $d$ ; the annotation box shows the reference values at  $d = 36$  nm. (Left panel) Dirichlet BCs. (Right panel) Neumann BCs.

structure is barely discernible. This behavior reflects two effects: (i) at smaller  $d$  more sources contribute to the smooth background that the detrending removes, and (ii) the thermal decay length  $\ell_T \sim 1/\sqrt{\beta + |\tilde{b}|}$  in units of  $d$  increases (since  $\beta$  shrinks faster than  $|\tilde{b}|$ ), causing the tails of adjacent cusps to overlap and merge into the background.

On the other hand, under NBC [Fig. 3, right panel], the same ordering persists ( $d = 80$  nm largest,  $d = 36$  nm smallest), but the amplitudes are uniformly one order of magnitude lower. The profiles also display resolved satellite peaks at neighbouring source positions, particularly visible for  $d = 80$  nm where the oscillatory structure of the Neumann Green’s function is most prominent. These satellites arise because the cosine eigenfunctions couple neighbouring sources more effectively than the sine eigenfunctions (of the DBC), and the zero-mode background is removed by the detrending.

## B. Transient dynamics at individual source sites

Now, we examine the temperature time profile  $\theta(\tau)$  at selected source positions. Figure 4 shows temperature temporal evolution at five probe positions, from near-edge ( $\xi_0 = 1$ ) to chain centre ( $\xi_0 = 10$ ), for a chain with  $\Lambda = 20$ ,  $\mathcal{N} = 21$  (illustrative parameters:  $\tilde{a} = 0.4$ ,  $\tilde{b} = -0.5$ ,  $\beta = 0.015$ ).

Under DBC [Fig. 4(a)], we may organize the five probe positions into three distinct groups: the near-edge source ( $\xi_0 = 1$ ) saturates at  $\theta_{\text{ss}} \simeq 0.39$ , the intermediate source ( $\xi_0 = 3$ ) at  $\simeq 0.68$ , and the three bulk sources ( $\xi_0 = 6, 8, 10$ ) cluster tightly at  $\simeq 0.77$ . We see that the

edge–bulk contrast ratio is roughly 1:2 and persists at all times. This reflects the permanent cooling imposed by the boundary thermal baths, or in other words, sources near the boundaries are cooled more efficiently than interior ones, producing a graded temperature distribution across the chain.

The picture is qualitatively different under NBC [Fig. 4(b)] since all five curves converge to a narrow band at  $\theta_{\text{ss}} \simeq 0.77$ – $0.78$ , corresponding to the spatially uniform steady state governed by the zero-mode balance (60).

Regarding the saturation value of  $\theta$ , we may show that the saturation time is given by  $\tau_{\text{sat}} = 1/|\mu_{\text{min}}| \simeq 2$ , where  $\mu_{\text{min}}$  is the least negative eigenvalue of the evolution matrix  $\mathbf{B}$ , and we note that 95% saturation requires  $\tau \simeq 3\tau_{\text{sat}} \simeq 6$ . This timescale is set by the competition between the source strength  $\tilde{a}$  and the effective decay rate  $|\tilde{b}| + \beta + \lambda_1$  of the fundamental mode [see Eqs. (B5, B14)], and is independent of the boundary condition for interior sources.

## C. Steady-state temperature profiles

The most direct illustration of the DBC/NBC dichotomy is provided by the steady-state temperature field  $\theta_{\text{ss}}(\xi)$ , obtained in the limit  $\tau \rightarrow \infty$  as  $\mathbf{c}_{\text{ss}} = -\mathbf{B}^{-1}\mathbf{d}$  [cf. Eq. (30)]. Accordingly, Figure 5 displays  $\theta_{\text{ss}}(\xi)$  for three interparticle spacings  $d = 30, 50, 100$  nm, using the physical magnetite–PMMA parameter set (Table I).

As expected, under DBC [Fig. 5(a)],  $\theta_{\text{ss}}(\xi)$  forms a smooth dome that vanishes at both chain ends, with a broad maximum in the interior. Then, smaller spacing  $d$  (i.e. larger  $\Lambda$  and more sources) yields higher peak tem-

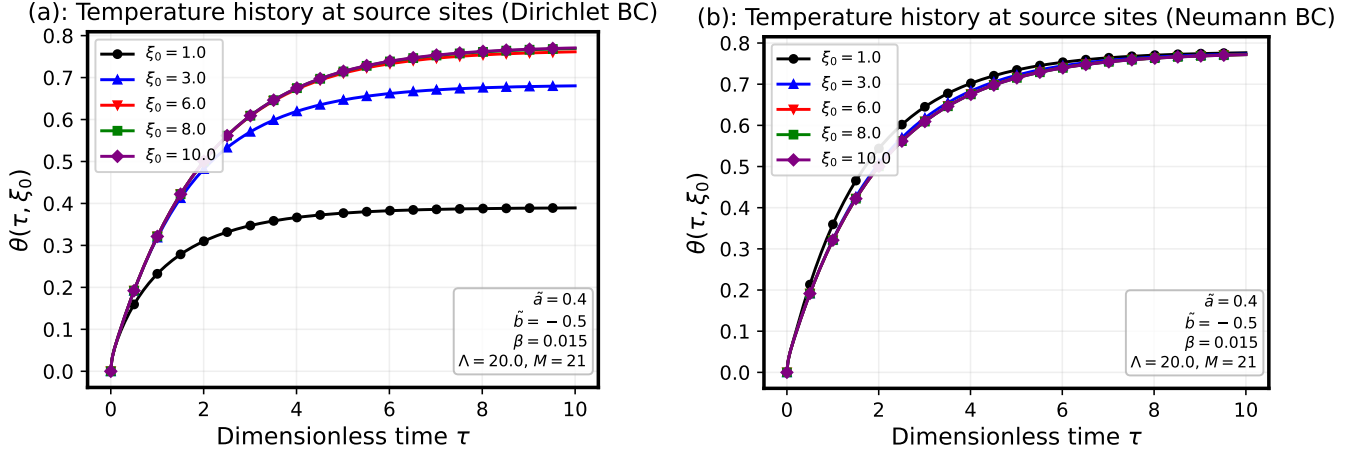


FIG. 4: Temperature history  $\theta(\tau)$  at five source positions from near-edge ( $\xi_0 = 1$ ) to chain centre ( $\xi_0 = 10$ ) ( $\Lambda = 20$ ,  $\mathcal{N} = 21$ ,  $\tilde{a} = 0.4$ ,  $\tilde{b} = -0.5$ ,  $\beta = 0.015$ ).

peratures. At this scale, individual nanomagnet cusps are entirely invisible and the temperature field is dominated by the lowest-order modal contributions, which produce a smooth, macroscopic envelope. Therefore, the characteristic parabolic-to-dome shape results from the balance between uniform internal heating and diffusive losses to the boundary baths, with the  $\sin(\pi\xi/\Lambda)$  fundamental mode providing the dominant contribution.

NBC [Fig. 5(b)] leads to a strikingly different situation. More precisely, the profile is essentially flat for all three spacings, with amplitudes of order 0.16–0.18, *i.e.* roughly five orders of magnitude larger than the DBC peak. This dramatic difference arises directly from the zero-mode accumulation: because  $\lambda_0 = 0$ , the zero mode cannot decay by diffusion to the boundaries and only the volumetric loss  $\beta\theta$  and the negative feedback  $\tilde{b} < 0$  can drain it. In the hypothetical  $\tilde{b} \rightarrow 0$  limit, the zero-mode balance [Eq. (60)] would give  $\theta_{\text{ss}} \simeq \tilde{a}\mathcal{N}/(\Lambda\beta)$ . For the physical parameters,  $\beta_{\text{phys}} \simeq 2 \times 10^{-11}$  is negligible compared with  $|\tilde{b}|\mathcal{N}/\Lambda \simeq 4 \times 10^{-8}$ , so the denominator of Eq. (60) is dominated by the feedback term and the pedestal reduces to  $\theta_{\text{ss}} \simeq \tilde{a}/|\tilde{b}| \approx 0.17$ , which is still five orders of magnitude above the DBC peak.

A word is in order regarding the weak  $d$ -dependence of the NBC profiles: the three curves in Fig. 5(b) are nearly coincident, making it difficult to read off the variation quantitatively from a spatial plot. Figure 5(c) addresses this directly by displaying both the NBC uniform amplitude and the DBC peak temperature as functions of  $d$  on a logarithmic scale.

Consequently, three observations follow from Fig. 5(c). First, the DBC peak falls monotonically with  $d$ , reflecting the decrease in the total number of sources  $\mathcal{N} \propto d^{-1}$  at fixed system length  $L$ . Second, the NBC amplitude is almost perfectly flat. Indeed, to leading order it equals  $\tilde{a}/|\tilde{b}|$  [Eq. (60)], which is  $d$ -independent, and the sub-leading correction  $\propto \beta/|\tilde{b}|\mathcal{N}/\Lambda$  is tiny for

$\beta_{\text{phys}} \ll |\tilde{b}|\mathcal{N}/\Lambda$ . Third, the gap between the two curves, roughly five orders of magnitude across the full range, encapsulates the central physical trade-off identified in Sec. III D 3, namely: insulating (Neumann-like) boundaries maximise absolute temperature, while conducting (Dirichlet-like) boundaries preserve spatial heterogeneity.

#### D. Spatial profiles: localized regime and crossover

To visualise the full spatio-temporal dynamics, we display spatial profiles  $\theta(\xi, \tau)$  at selected times for both the stable localized regime (Fig. 6) and the critical crossover regime (Fig. 7). This representation conveys the same information as a space-time map but makes the growth of individual source peaks, the edge–bulk hierarchy, and the onset of spatial homogenisation directly readable on a common scale.

##### 1. Localized heating regime

Figure 6 shows  $\theta(\xi, \tau)$  at  $\tau = 0.25, 0.5, 1.0, 2.0$  for  $\Lambda = 42$ ,  $\mathcal{N} = 7$ ,  $\Delta\xi = 7$ ,  $\tilde{b} = -0.52$ ,  $\beta = 0.017$  (localized regime, well below  $\tilde{b}_c$ ). Both panels share the same set of source positions; the faint vertical dashed lines mark each source site for orientation.

Under DBC [Fig. 6, left], the profiles grow uniformly across the interior of the chain, with the edge sources visibly suppressed relative to the bulk. We see that the envelope of the peaks is nearly flat in the interior at each time, thus confirming that the fundamental Dirichlet mode  $\sin(\pi\xi/\Lambda)$  spreads the heating broadly. On the other hand, individual source peaks are resolved. Indeed, since the inter-particle spacing  $\Delta\xi = 7$  exceeds the thermal decay length  $\ell_T = 1/\sqrt{\beta + |\tilde{b}|} \approx 1.3$ , the tails of adjacent peaks do not overlap significantly. As  $\tau$  increases

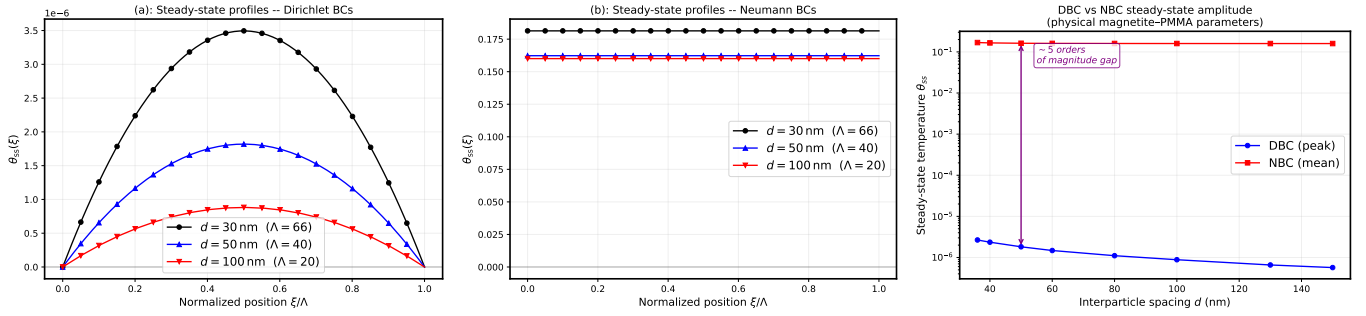


FIG. 5: Steady-state profiles for  $d = 30, 50, 100$  nm (physical magnetite–PMMA parameters). (a) DBC:  $\theta_{ss}(\xi)$ . (b) NBC:  $\theta_{ss}(\xi)$ . (c) Peak amplitudes  $\theta_{ss}^{(D)}$  (circles) and  $\theta_{ss}^{(N)}$  (squares) vs  $d$  (log scale).

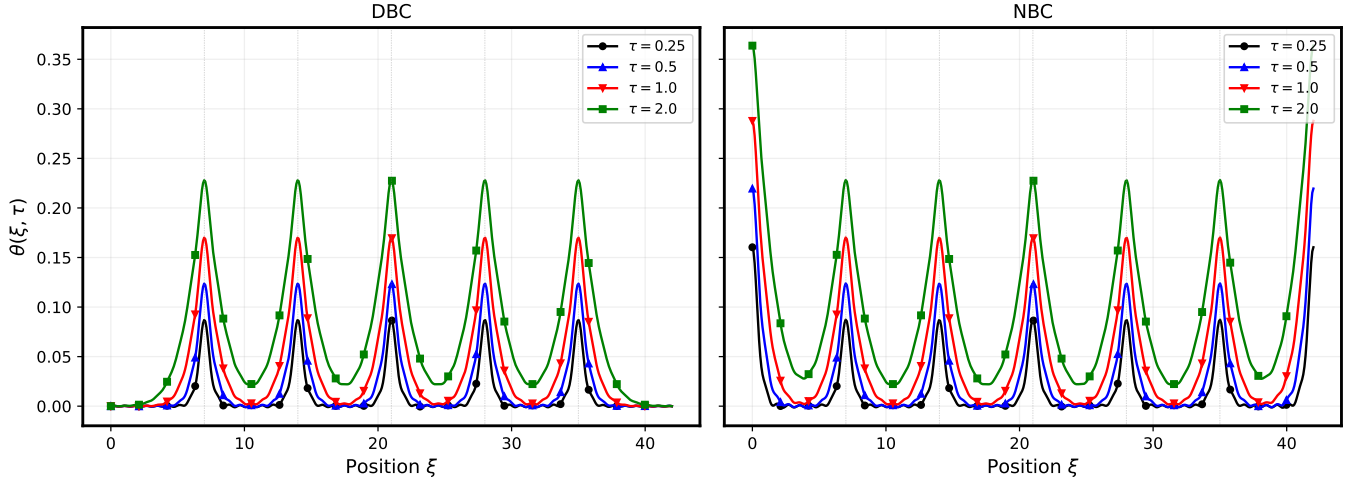


FIG. 6: Spatial temperature profiles  $\theta(\xi, \tau)$  at  $\tau = 0.25, 0.5, 1.0, 2.0$  in the localized regime ( $\Lambda = 42, \mathcal{N} = 7, \Delta\xi = 7, \tilde{b} = -0.52, \beta = 0.017$ ). Faint dashed lines mark the source positions.

from 0.25 to 2.0, the profiles grow quasi-proportionally, approaching the dome-shaped steady state of Fig. 5(a).

In the case of NBC [Fig. 6, right], two distinct features appear. First, the baseline rises monotonically with  $\tau$ : even the inter-peak minima increase in time, reflecting the accumulation of heat in the spatially uniform zero mode  $\phi_0 = 1/\sqrt{\Lambda}$ . So, by  $\tau = 2.0$ , the baseline has risen to a level comparable to the individual peak amplitudes, indicating that the zero-mode background is already substantial. Second, the edge sources ( $\xi = 0$  and  $\xi = \Lambda$ ) produce the largest peaks at every time, reversing the DBC hierarchy. Indeed, as already mentioned earlier, the no-flux boundary reflects all diffusing heat inward, effectively doubling the local source strength. The peak-to-valley contrast, *i.e.*, the direct measure of spatial localisation, decreases visibly with  $\tau$  as the zero mode inflates the baseline, consistent with the suppression of the relative variance  $\mathcal{V}_{\text{rel}}^{(N)}$  established analytically in Appendix B.

Comparing the two panels at the same time and on the same scale makes explicit the fact that the overall temperature level is uniformly higher under NBC, but

the spatial contrast (peak height above local baseline) is substantially lower. This is the real-space counterpart of the variance-mean ratio diagnostic we discussed in Sec. V E.

## 2. Crossover regime

In Figure 7, we plot the same profile representation for the crossover regime:  $\Lambda = 10, \mathcal{N} = 6, \Delta\xi = 2, \beta = 0.017, \tilde{b} \simeq \tilde{b}_c$ . The DBC panel uses  $\tilde{b} \simeq \tilde{b}_c^{(D)} = -0.23$  and the NBC panel uses  $\tilde{b} \simeq \tilde{b}_c^{(N)} = -0.17$  (the respective critical values).

We note that near the critical feedback coefficient  $\tilde{b}_c$ , the least-negative eigenvalue of  $\mathbf{B}$  approaches zero and thereby the temperature grows quasi-linearly in time. The profile plots reveal the spatial structure of this growth in detail.

Under DBC [Fig. 7, left], the profiles retain a clearly resolved, sine-shaped envelope at all four times, while individual source peaks sit on top of the fundamental-mode background. Again, the temperature vanishes at

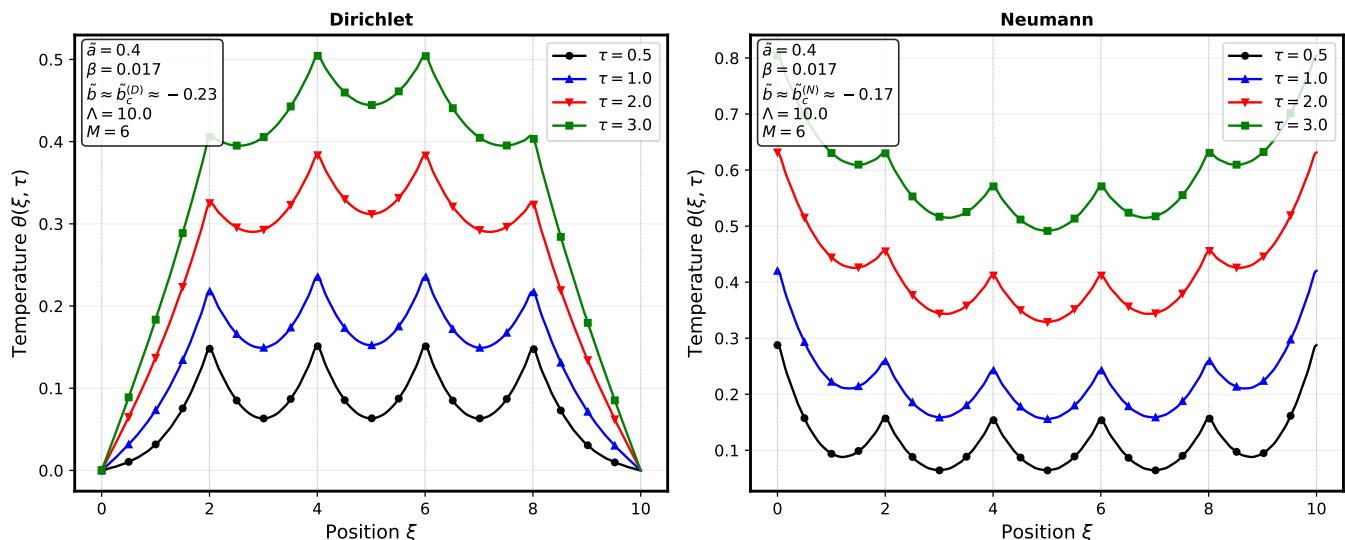


FIG. 7: Spatial temperature profiles  $\theta(\xi, \tau)$  at  $\tau = 0.5, 1.0, 2.0, 3.0$  near criticality ( $\Lambda = 10, \mathcal{N} = 6, \Delta\xi = 2, \beta = 0.017$ ). Left: DBC at  $\tilde{b} = \tilde{b}_c^{(D)} = -0.23$ . Right: NBC at  $\tilde{b} = \tilde{b}_c^{(N)} = -0.17$ .

both edges at all  $\tau$ , maintaining the edge–bulk hierarchy even as the amplitude grows. This growth is nearly proportional in time up to  $\tau = 3$ : the ratio of the  $\tau = 3$  and  $\tau = 0.5$  profiles is approximately constant across  $\xi$ , thus confirming the dominance of a single slow mode ( $r = 1$ ) whose decay rate  $|B_{11}|$  is small but finite.

Under NBC [Fig. 7, right], the temporal evolution is qualitatively different. At early times ( $\tau = 0.5$ ), individual source peaks are still resolved and the edge sources are enhanced relative to the interior, essentially the same pattern seen in Fig. 6. By  $\tau = 1.0$ , the zero-mode pedestal starts to dominate the overall amplitude while individual source peaks remain resolved above it. By  $\tau = 2.0$ – $3.0$ , the pedestal continues to grow steeply and the peak-to-baseline contrast decreases markedly, though discrete source peaks remain discernible at all times shown. This is the direct visualisation of the near-critical NBC regime: the spatially uniform zero mode drives the dominant temperature rise, thus progressively reducing the relative spatial heterogeneity without fully suppressing the individual source peaks.

### E. Statistical indicators of the crossover: variance and mean

The physical indicators introduced in Sec. III D, namely the mean temperature  $\langle\theta\rangle$  [Eq. (56)] and spatial variance  $\text{Var}(\theta)$  [Eq. (57)], provide us with scalar diagnostics that track the local-to-global crossover as  $\tilde{b}$  varies. Accordingly, Fig. 8 displays both quantities at late time as a function of  $\tilde{b}$ , with the vertical dotted line marking the analytical critical value  $\tilde{b}_c$ .

As we can see, both quantities diverge as  $\tilde{b} \rightarrow \tilde{b}_c^-$ . This behavior signals the approach to marginal stability: the fundamental-mode decay rate  $|\mu_1| \rightarrow 0$ , the modal am-

plitudes grow without bound, and the temperature field fails to reach a finite steady state within the simulated time window.

Under DBC [Fig. 8(a)], the variance and mean are of the same order of magnitude (both  $\sim 0.2$ – $1.2$  in the pre-critical range), confirming that the temperature field retains significant spatial structure. The peaks at source sites contribute comparably to both the mean (through their absolute height) and the spread (through the peak-to-valley contrast), so the ratio  $\text{Var}(\theta)/\langle\theta\rangle^2 = \mathcal{O}(1)$ .

Under NBC [Fig. 8(b)], we see that the mean temperature is much larger ( $\langle\theta\rangle \sim 1$ – $3$ ), while the variance remains very small ( $\text{Var}(\theta) \sim 0$ – $0.025$ ), roughly two orders of magnitude below the DBC values. This quantitatively confirms the homogenising effect of the zero mode. More precisely, NBC produces a large but spatially uniform temperature, whereas DBC preserves strong spatial contrast.

This figure provides the most direct numerical verification of the central trade-off identified analytically in Sec. III D 3, namely the relative spatial variance  $\mathcal{V}_{\text{rel}}^{(N)} \ll \mathcal{V}_{\text{rel}}^{(D)}$  whenever  $\beta \ll |\tilde{b}|\mathcal{N}/\Lambda$ . Therefore, for applications requiring spatially targeted heating (e.g. site-selective drug release), the DBC regime with its preserved heterogeneity is preferable; for applications requiring maximal bulk temperature rise (e.g. whole-tumour hyperthermia), the NBC regime is more effective.

### F. Assembly-scale temperature evolution

We recall that the coarse-grained assembly-scale heat equation (35), with the linearized source term (37), is designed to describe the macroscopic temperature

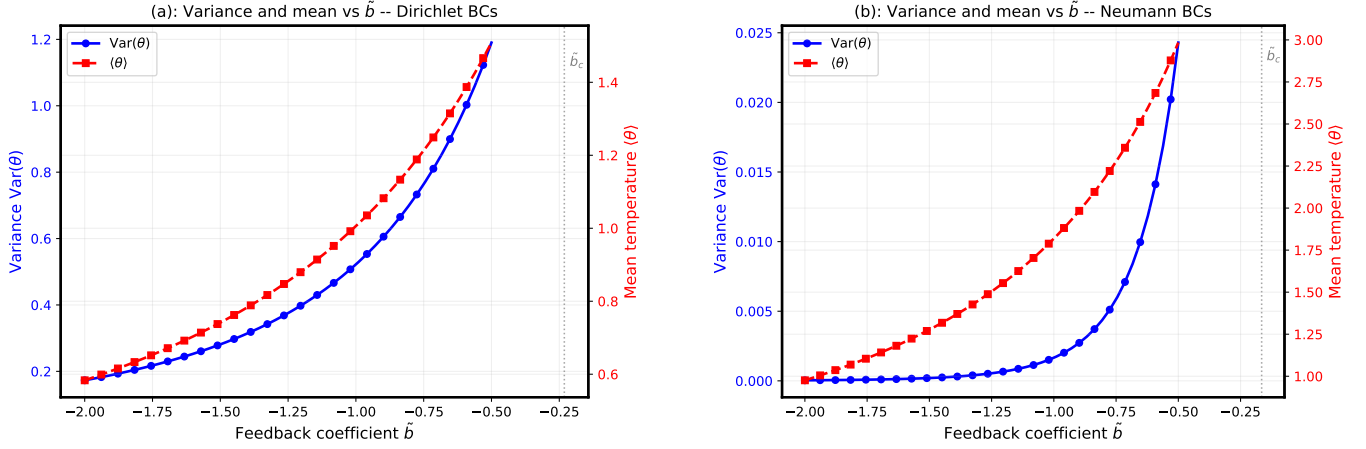


FIG. 8: Spatial variance  $\text{Var}(\theta)$  and mean  $\langle \theta \rangle$  at late time vs feedback coefficient  $\tilde{b}$ . Dotted line:  $\tilde{b}_c$ .

field  $\Theta(\xi, \tau_s)$  that emerges from spatial averaging of the nanoscale sources. Accordingly, Figure 9 shows  $\Theta(\xi, \tau)$  at three time snapshots ( $\tau = 0.5, 1.0, 2.0$ ), using the coarse-grained coefficients  $a_{cg} = 0.5$ ,  $b_{cg} = -1.0$  (illustrative values) and  $\zeta = 1$ .

Under DBC [Fig. 9(a)],  $\Theta$  vanishes at both ends and develops a broad, flat-topped profile in the interior, with the plateau rising as  $\tau$  increases. The boundary layers sharpen with time as the interior approaches the steady-state value  $\Theta_{ss} = a_{cg}/(1 - b_{cg})$ . This dome-shaped profile is the assembly-scale analogue of the nanoscale steady-state profile [Fig. 5(a)], thus confirming the consistency of the two-scale framework.

In contrast, under NBC [Fig. 9(b)],  $\Theta$  is perfectly spatially uniform at all times, because the zero-flux boundaries eliminate all spatial modes, and only the spatially uniform zero mode survives. So, the three horizontal lines in Fig. 9(b) make explicit what the modal analysis already shows analytically, *i.e.* the fact that the assembly-scale NBC problem reduces to the first-order ODE  $\dot{\Theta} = a_{cg} + (b_{cg} - 1)\Theta$ , whose solution is a pure exponential approach to  $\Theta_{ss}$ . Since the spatial profiles provide no additional information beyond the amplitude at each time, Fig. 9(c) presents the more informative comparison as a time profile. These plots make quantitative two features, which follow directly from the coarse-grained equation (35).

*Asymptotes.* Setting  $\partial\Theta/\partial\tau_s = 0$  in Eq. (35) yields the steady-state ODE

$$\zeta\Theta'' - k^2\zeta\Theta = -a_{cg}, \quad k = \sqrt{(1 - b_{cg})/\zeta}. \quad (66)$$

Under NBC the zero-mode condition  $\Theta'' = 0$  gives the spatially uniform solution  $\Theta_{ss} = a_{cg}/(1 - b_{cg}) = 0.25$ . Under DBC the general even solution (the source and domain are both symmetric) is  $\Theta(\tilde{\xi}) = \Theta_{ss} + C \cosh(k\tilde{\xi})$ , where  $\tilde{\xi} = \xi - \Lambda/2$ . Imposing  $\Theta(\pm\Lambda/2) = 0$  fixes  $C =$

$-\Theta_{ss}/\cosh(k\Lambda/2)$ , so the midpoint value is

$$\Theta_{ss}^{\text{DBC}}(\xi) = \Theta_{ss} \left[ 1 - \frac{1}{\cosh(k\Lambda/2)} \right]. \quad (67)$$

For the chosen parameters ( $k\Lambda \approx 7.07$ ) this evaluates to  $\Theta_{ss}^{\text{DBC}}(\Lambda/2) \approx 0.235$ , lying  $\sim 6\%$  below  $\Theta_{ss}^{\text{NBC}} = 0.25$ , a correction of order  $e^{-k\Lambda/2}$  that vanishes for  $k\Lambda \gg 1$ . Both asymptotes are therefore governed by the source-loss balance alone, not by the boundary conditions.

*Decay rates.* Expanding  $\Theta$  in the eigenbasis of  $-\nabla^2$  (eigenvalues  $\lambda_r$ ), the linear operator  $\zeta\nabla^2 + (b_{cg} - 1)$  in Eq. (35) is diagonal with eigenvalues  $-(\zeta\lambda_r + 1 - b_{cg})$ , so each modal amplitude decays as  $e^{-\mu_r\tau}$  with the rate

$$\mu_r = \zeta\lambda_r + (1 - b_{cg}). \quad (68)$$

For NBC the only excited mode is the zero mode ( $\lambda_0 = 0$ ), giving  $\mu_0^{\text{NBC}} = 1 - b_{cg} = 2$ . For DBC the dominant late-time mode is the fundamental mode ( $\lambda_1 = \pi^2/\Lambda^2$ ), giving  $\mu_1^{\text{DBC}} = \zeta(\pi/\Lambda)^2 + (1 - b_{cg}) \approx 2.39$ . Since  $\zeta(\pi/\Lambda)^2 > 0$ , the DBC midpoint always saturates *faster* than NBC by the diffusive excess  $\zeta(\pi/\Lambda)^2$  [see Fig. 9(c)], which encodes the additional spatial relaxation of the DBC eigenfunction basis. This faster DBC saturation is the assembly-scale counterpart of the higher critical threshold  $|\tilde{b}_c^{(D)}| > |\tilde{b}_c^{(0)}|$  identified at the nanomagnet scale: the extra spatial mode structure of the DBC solution provides an additional dissipation channel absent under NBC.

### G. Two-scale consistency: nanoscale mean versus assembly-scale prediction

The two-scale framework we develop here rests on the assumption that the spatial mean of the nanoscale temperature field can be faithfully represented by the coarse-grained assembly-scale equation with effective coefficients  $a_{cg}$ ,  $b_{cg}$ . We test this assumption by comparing, in

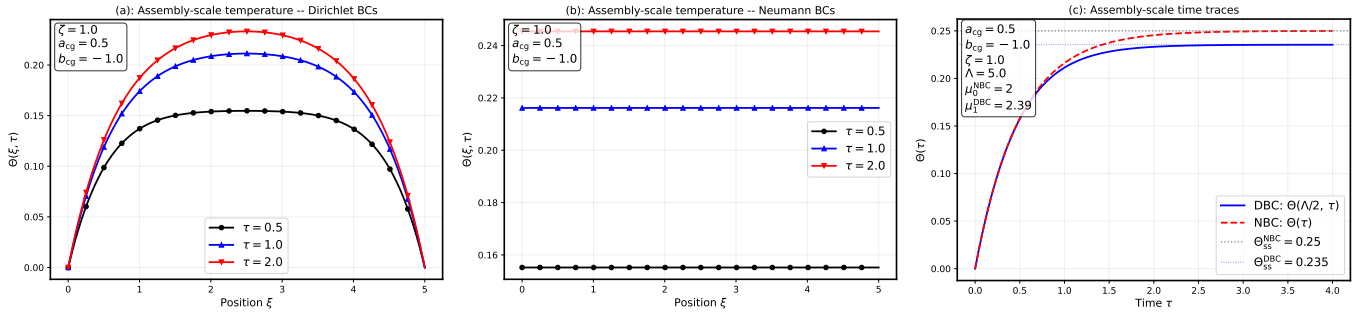


FIG. 9: Coarse-grained assembly-scale temperature ( $a_{cg} = 0.5$ ,  $b_{cg} = -1.0$ ,  $\zeta = 1$ ,  $\Lambda = 5$ ). (a) DBC spatial profiles at  $\tau = 0.5, 1.0, 2.0$ . (b) NBC spatial profiles at the same times. (c) DBC midpoint  $\Theta(\Lambda/2, \tau)$  (blue solid) and NBC uniform temperature  $\Theta(\tau)$  (red dashed). Dotted lines: respective long-time asymptotes (see text).

Figure 10, the nanoscale spatial mean  $\langle \theta \rangle_\xi(\tau)$  with the coarse-grained spatial mean  $\langle \Theta \rangle_\xi(\tau)$ , for two choices of coefficients: the analytically matched coefficients derived below (red dashed) and the naive density mapping included for comparison (gray dotted) <sup>1</sup>.

*Derivation of the effective coarse-grained coefficients.* To obtain the coefficients that faithfully reproduce the nanoscale spatial mean, we integrate Eq. (18) over the domain  $[0, \Lambda]$ . Under NBC (where the boundary flux vanishes), this yields an exact ODE for the spatial mean  $\langle \theta \rangle$ ,

$$\frac{d\langle \theta \rangle}{d\tau} = a_{cg}^{(0)} - (\beta - R b_{cg}^{(0)}) \langle \theta \rangle, \quad (71)$$

where  $a_{cg}^{(0)} = \mathcal{N}\tilde{a}/\Lambda$  and  $b_{cg}^{(0)} = \mathcal{N}\tilde{b}/\Lambda$  are the source densities, and  $R = \langle \theta \rangle_{\text{sites}} / \langle \theta \rangle_\xi = (\mathcal{N}^{-1} \sum_n \theta(\xi_n)) / \langle \theta \rangle_\xi$  is the source-site enhancement factor. Under NBC the spatially uniform zero mode ( $\lambda_0 = 0$ ) contributes equally to  $\langle \theta \rangle_{\text{sites}}$  and  $\langle \theta \rangle_\xi$ , so  $R = 1$  exactly in the zero-mode limit; the correction  $R - 1$  arises from the higher cosine modes ( $r \geq 1$ ), which peak at the source positions but integrate to zero over  $[0, \Lambda]$ , making  $R$  only slightly above unity ( $R_{\text{NBC}} \approx 1.01$  for the crossover set).  $R$  is evaluated numerically from the steady-state modal solution and can also be expressed analytically via the static Green's function of the operator  $-\partial_\xi^2 + \beta$  (Appendix C). The two corrections encoded in Eq. (71) relative to a direct density substitution are: (i) the feedback term  $\tilde{b}\theta(\xi_n, \tau)$  in

<sup>1</sup>The assembly-scale equation (35) under NBC (spatially uniform zero mode) reads:

$$\frac{d\Theta}{d\tau_s} = a_{cg} - (1 - b_{cg})\Theta. \quad (69)$$

Changing to nanoscale time via  $d/d\tau = (t_d/t_s) d/d\tau_s$ , and defining the effective coefficients to absorb the time-scale factor, the (naive) coarse format in  $\tau$  is:

$$\frac{d\Theta}{d\tau} = a_{cg} - (1 - b_{cg})\Theta, \quad (70)$$

where the coefficients  $a_{cg}$ ,  $b_{cg}$  are understood as matched to nanoscale time.

the nanoscale equation is evaluated at the source sites, not at the domain average, introducing the factor  $R$ ; and (ii) the physical nanoscale loss rate is  $\beta \ll 1$ , whereas the assembly-scale equation (35) normalises its loss coefficient to unity. The true nanoscale effective loss rate is therefore  $\mu_{\text{nano}} = \beta + R |b_{cg}^{(0)}| \simeq 0.76$  for the crossover parameter set.

*Matched coarse-grained coefficients.* Matching the effective loss rate of Eq. (71) to the coarse format  $d\Theta/d\tau = a_{cg} - (1 - b_{cg})\Theta$  yields the NBC correction

$$b_{cg}^{\text{NBC}} = 1 - \beta + R b_{cg}^{(0)}, \quad (72)$$

which simultaneously matches both the decay rate and the long-time asymptote of the spatial mean. For the crossover set:  $R_{\text{NBC}} \simeq 1.01$ , giving  $b_{cg}^{\text{NBC}} = +0.232$ , with steady-state  $\langle \Theta \rangle_\infty^{\text{NBC}} = a_{cg}^{(0)} / (1 - b_{cg}^{\text{NBC}}) = 1.56$ . By contrast, the naive density substitution  $b_{cg}^{(0)} = \mathcal{N}\tilde{b}/\Lambda = -0.744$  omits both corrections (i) and (ii) above, yielding an effective loss rate  $1 - b_{cg}^{(0)} = 1.74$ , a factor 2.3 larger than  $\mu_{\text{nano}}$ , and should be avoided.

For DBC, the escape of heat through the boundaries introduces an additional effective loss channel absent from the NBC case. Thus, the coarse DBC spatial-mean steady state has the closed form

$$\langle \Theta \rangle_\infty^{\text{DBC}} = \frac{a_{cg}}{1 - b_{cg}} \left[ 1 - \frac{\tanh(k\Lambda/2)}{k\Lambda/2} \right], \quad k = \sqrt{\frac{1 - b_{cg}}{\zeta}}, \quad (73)$$

and  $b_{cg}^{\text{DBC}}$  is found by equating this expression to the exact nanoscale steady-state spatial mean  $\langle \theta_{\text{ss}} \rangle^{\text{DBC}}$  (obtained from the modal linear solution  $\theta_{\text{ss}} = -\mathbf{B}^{-1}\mathbf{d}$ ). For the crossover set,  $\langle \theta_{\text{ss}} \rangle^{\text{DBC}} = 1.06$ , giving  $b_{cg}^{\text{DBC}} = +0.110$ .

*Numerical results.* We have found that the matched coefficients reduce the RMS error between  $\langle \theta \rangle_\xi$  and  $\langle \Theta \rangle_\xi$  at  $\tau \in [0, 4]$  by a factor of  $\sim 4$  under NBC (from 0.46 to 0.11) and by a factor of  $\sim 2$  under DBC (from 0.24 to 0.13). The residual discrepancy reflects multi-mode effects: the nanoscale solution involves many decay modes of  $\mathbf{B}$  with different rates, while the coarse equation has a single effective mode. We believe that retaining higher modes should further reduce this residual discrepancy.

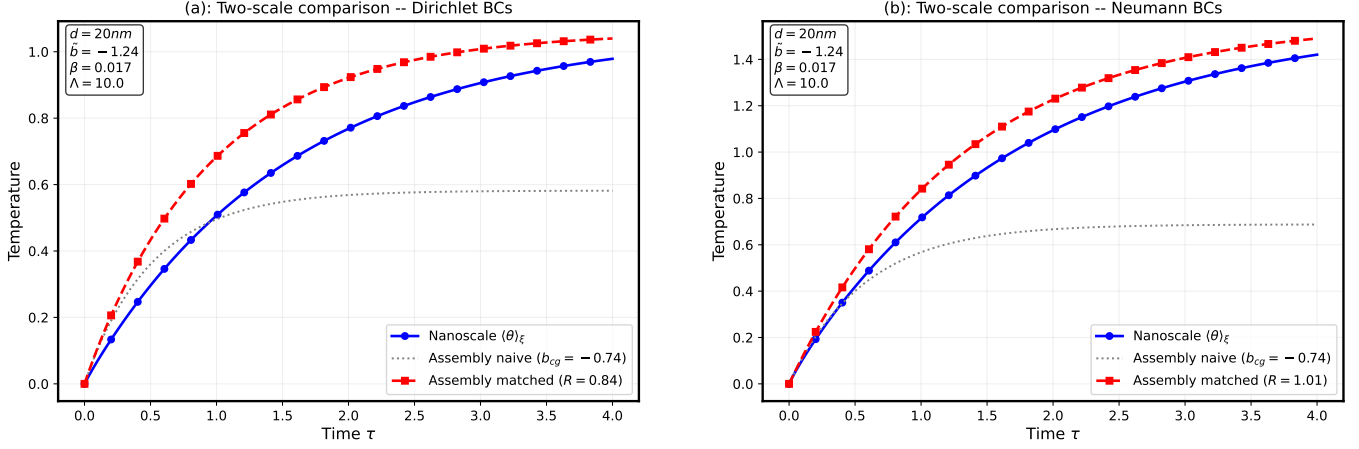


FIG. 10: Nanoscale spatial mean  $\langle\theta\rangle_\xi$  (blue solid) vs coarse-grained spatial mean  $\langle\Theta\rangle_\xi$  with naive density coefficients  $b_{\text{cg}}^{(0)} = \mathcal{N}\tilde{b}/\Lambda = -0.74$  (gray dotted) and analytically matched coefficients (red dashed;  $b_{\text{cg}}^{\text{DBC}} = +0.11$ ,  $b_{\text{cg}}^{\text{NBC}} = +0.23$ ). Left: DBC. Right: NBC. CROSSOVER parameter set ( $\tilde{b} = -1.24$ ,  $\beta = 0.017$ ,  $\Lambda = 10$ ,  $\mathcal{N} = 6$ ,  $\Delta\xi = 2$ ).

#### H. Correlation length, interfacial coupling, and TC-DC interplay

To complete the picture of the crossover and its dependence on the two coupling channels, namely the interfacial thermal conductance  $h_s$  (encoded in  $\gamma_s$ ) and the dipolar coupling (encoded in  $\tilde{\lambda}$ ), we have considered the following three complementary observables.

*Thermal correlation length.* In Fig. 11 we show the first-moment autocorrelation length  $\xi_{\text{corr}}(\tau)$  for four values of  $\tilde{b}$  bracketing the critical value  $\tilde{b}_c$ , using the crossover parameter set ( $\tilde{a} = 2.0$ ,  $\beta = 0.017$ ,  $\Lambda = 10$ ,  $\mathcal{N} = 6$ ,  $\Delta\xi = 2$ ). We see that under DBC, all curves grow slowly and remain near unity, since the boundary conditions suppress any qualitative dependence on  $\tilde{b}$ . On the other hand, under NBC, each curve undergoes a sharp jump to  $\xi_{\text{corr}} \approx \Lambda/2$  at a time  $\tau^*$  that decreases as  $|\tilde{b}|$  approaches  $|\tilde{b}_c|$ : this is the direct signature of the crossover, *i.e.* the spatially uniform NBC zero mode abruptly dominates the profile.

*Sensitivity to the interfacial coupling  $\gamma_s$ .* In Fig. 12 we plot the peak steady-state temperature  $\theta_{\text{max}}$  as a function of  $\gamma_s$  for both boundary conditions, using the physical magnetite-PMMA parameter set ( $\Lambda = 55$ ,  $\mathcal{N} = 56$ ,  $\beta = 1.9 \times 10^{-11}$ ). Under DBC,  $\theta_{\text{max}}$  rises by nearly one order of magnitude over two decades of  $\gamma_s$ , driven by the SAR renormalisation  $\tilde{a} \propto \gamma_s/(\gamma_s - \varepsilon)$ . Under NBC,  $\theta_{\text{max}}$  is essentially constant ( $\Delta\theta/\theta \sim 2 \times 10^{-3}$ ): since the NBC steady state is set by the ratio  $\tilde{a}/|\tilde{b}|$  and both coefficients scale identically with  $\gamma_s$ , the peak temperature is, to leading order,  $\gamma_s$ -independent.

*TC-DC interplay.* Finally, figure 13 adds dipolar coupling  $\tilde{\lambda}$  to the picture. The constraint  $d \geq 3D$  (validity of the dipole approximation) restricts  $\tilde{\lambda}$  to the range  $[0, \tilde{\lambda}_{\text{nat}}] \approx [0, 0.009]$ , achieved at centre-to-centre separations  $d/D \in [3.0, \infty)$ . We see that under DBC, the

dipolar coupling enhances  $\theta_{\text{max}}$  and this enhancement is itself  $\gamma_s$ -dependent: it grows from  $\sim 6\%$  at small  $\gamma_s$  to  $\sim 18\%$  at large  $\gamma_s$ , causing the four curves to fan out, and this is a non-trivial interplay between the two coupling channels. Under NBC, the ratio  $\theta_{\text{max}}(\tilde{\lambda})/\theta_{\text{max}}(0)$  is constant to numerical precision across the full  $\gamma_s$  sweep: the two effects enter multiplicatively and independently, a direct consequence of zero-mode dominance.

#### I. Summary of DBC versus NBC effects across all observables

After this lengthy comparison of the two boundary conditions, we summarize in Table IV the principal differences between them across all observables presented above. The entries summarise the results of Figs. 1–13 and provide a compact reference for the DBC/NBC dichotomy.

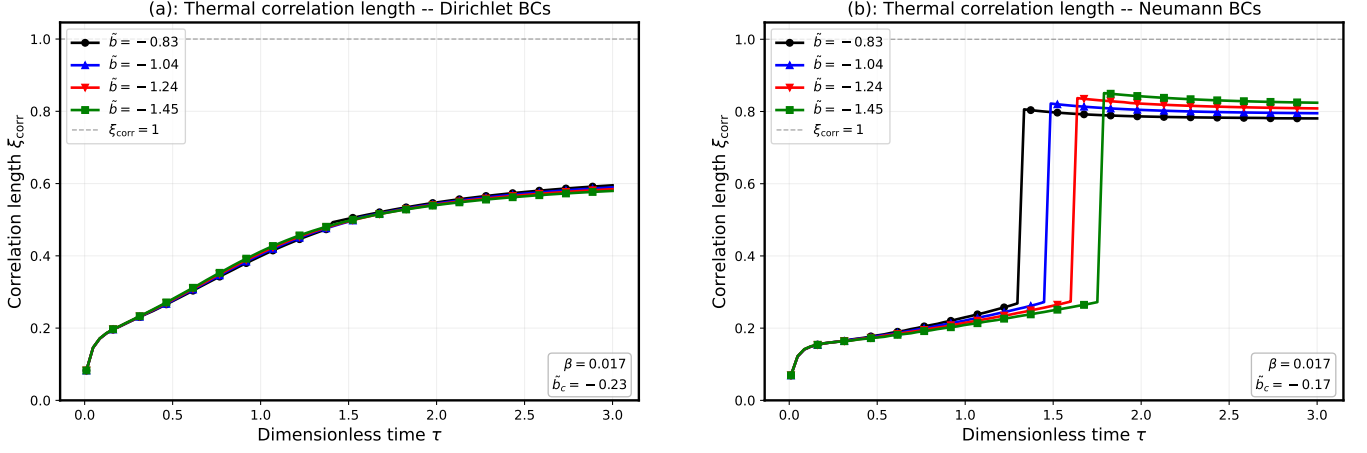


FIG. 11: Thermal correlation length  $\xi_{\text{corr}}(\tau)$  for four values of  $\tilde{b}$  bracketing  $\tilde{b}_c$  (CROSSOVER set:  $\beta = 0.017$ ,  $\Lambda = 10$ ,  $\mathcal{N} = 6$ ,  $\Delta\xi = 2$ ). DBC (a): all curves grow slowly and remain  $\lesssim 1$ , with little sensitivity to  $\tilde{b}$ . NBC (b): each curve undergoes a sharp jump at a time  $\tau^*(\tilde{b})$  that decreases as  $|\tilde{b}| \rightarrow |\tilde{b}_c|$ , the direct signature of zero-mode dominance.

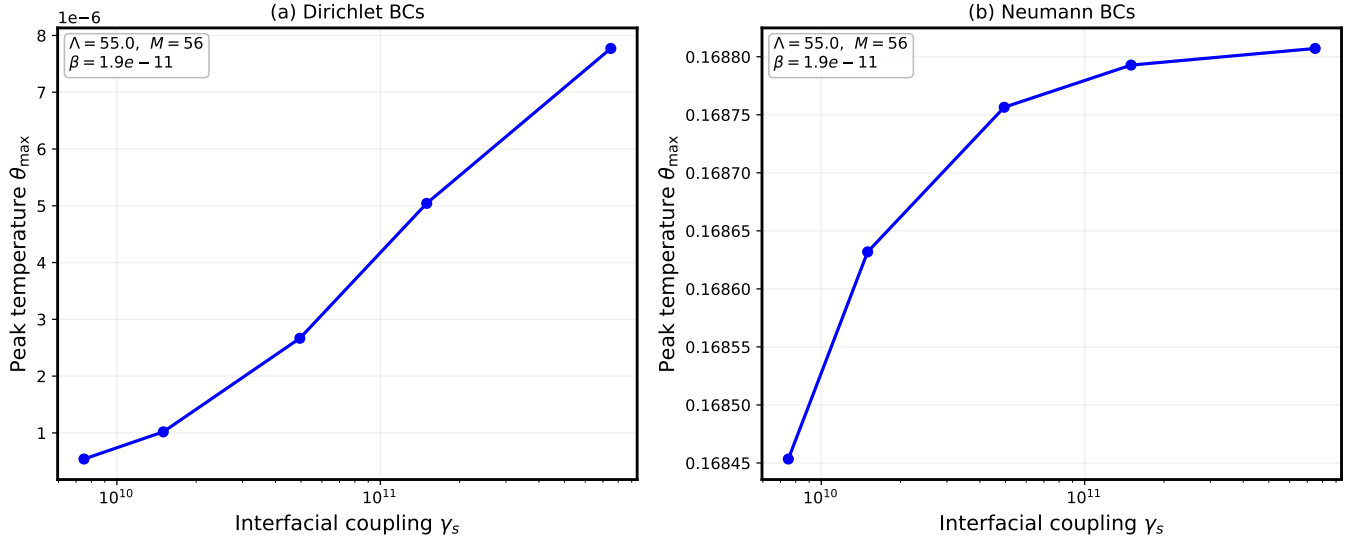


FIG. 12: Peak steady-state temperature  $\theta_{\text{max}}$  vs. dimensionless interfacial coupling  $\gamma_s$  for (a) DBC and (b) NBC (physical magnetite-PMMA:  $\Lambda = 55$ ,  $\mathcal{N} = 56$ ,  $\beta = 1.9 \times 10^{-11}$ ). DBC: strong monotonic growth spanning nearly one decade. NBC: negligible variation ( $\Delta\theta/\theta \sim 2 \times 10^{-3}$ ) because the ratio  $\tilde{a}/\tilde{b}$  is  $\gamma_s$ -independent.

Observable	DBC (ideal bath)	NBC (insulated)
Edge source $\theta$	Suppressed	Enhanced (reflected heat)
Absolute $\theta_{\text{max}}$	Lower	Higher
Spatial contrast	Preserved	Washed out by zero mode
Zero mode	Absent	Present ( $\lambda_0 = 0$ )
$\tilde{b}_c$ threshold	$ \tilde{b}_c $ larger	$ \tilde{b}_c $ smaller
$\text{Var}/\langle\theta\rangle$	$\mathcal{O}(1)$	$\ll 1$
Assembly profile	Dome-shaped	Perfectly flat $a_{\text{cg}}\mathcal{N}/(\Lambda\beta)$ (loss-dominated)
Steady-state scaling	$\theta_{\text{ss}} \propto \Lambda^2$	$ \tilde{a} / \tilde{b} $ (feedback-dominated)

TABLE IV: Summary of the principal differences between Dirichlet and Neumann boundary conditions across all observables.

## VI. CONCLUSIONS

We have developed a two-scale analytical framework, namely the Local-to-Global Heat Crossover, for studying the thermal physics of one-dimensional chains of nanomagnets subjected to alternating magnetic fields. This framework allows us to resolve individual nanomagnet sources as temperature-dependent heat sources and to connect the resulting nanoscale temperature field, through spatial and temporal coarse-graining, to the macroscopic heating observable in, *e.g.*, magnetic hyperthermia applications. We summarize our main findings as follows:

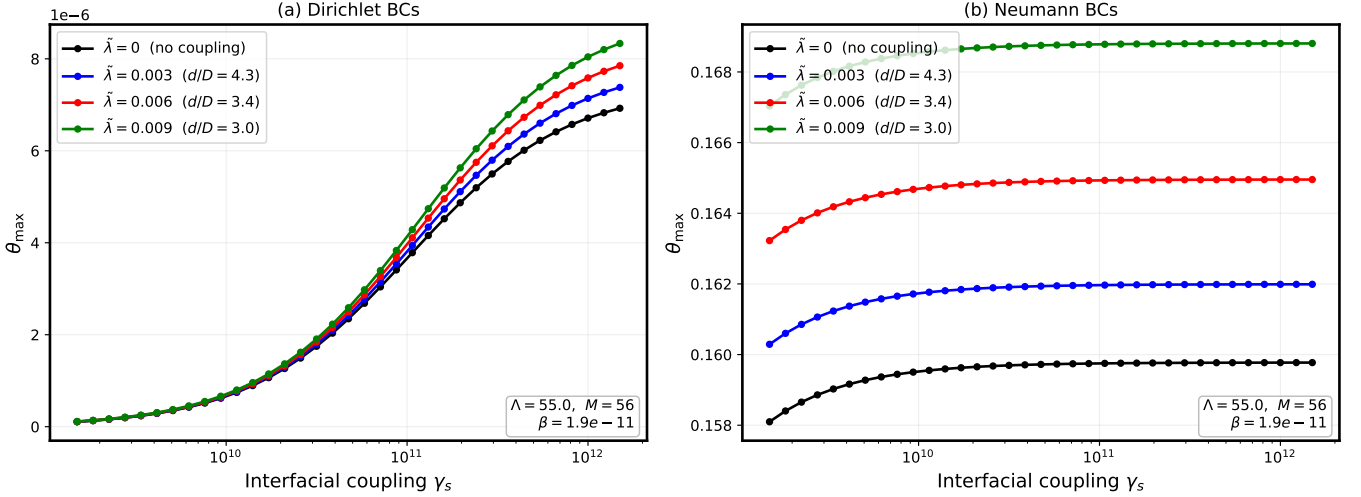


FIG. 13: Peak steady-state temperature  $\theta_{\max}$  vs.  $\gamma_s$  for four physically valid dipolar coupling values  $\tilde{\lambda} \in \{0, 0.003, 0.006, 0.009\}$  ( $d/D \in \{\infty, 4.8, 3.8, 3.0\}$ ), for (a) DBC and (b) NBC. DBC: curves fan out with increasing  $\gamma_s$  (non-trivial TC–DC interplay; enhancement 6%  $\rightarrow$  18%). NBC: curves are parallel (multiplicative independence of the two coupling channels).

*Nanomagnet-scale thermal structure.* The dimensionless heat equation (18), solved exactly via modal decomposition [Eq. (30)], reveals that each nanomagnet generates a cusp-like temperature peak at its source position, with a spatial extent controlled by the thermal decay length  $\ell_T = 1/\sqrt{\beta + |\tilde{b}|}$ . For realistic magnetite–PMMA parameters, the peak amplitudes are of order  $10^{-8}$ – $10^{-9}$  in dimensionless units (corresponding to  $\sim \mu\text{K}$  temperature excursions), confirming that nanoscale thermal localisation, while mathematically exact, is physically unresolvable by any current experimental technique. The source-localised structure is, however, well displayed using illustrative parameters elevated by 7–9 orders of magnitude (Table III), which preserve all qualitative features of the solution.

*Role of boundary conditions.* The extensive comparison of Dirichlet (ideal thermal bath) and Neumann (perfect insulation) boundary conditions reveals a fundamental trade-off with direct consequences for applications. Dirichlet conditions preserve strong spatial heterogeneity: the relative variance  $\mathcal{V}_{\text{rel}}^{(D)}$  is of order unity, steady-state profiles are dome-shaped with a clear edge–bulk difference, and the temperature vanishes at the chain boundaries. Neumann conditions, by contrast, activate a zero mode ( $\lambda_0 = 0$ ) that accumulates heat globally, at the cost of washing out all spatial structure ( $\mathcal{V}_{\text{rel}}^{(N)} \ll \mathcal{V}_{\text{rel}}^{(D)}$ ). The critical feedback coefficient for the local-to-global crossover is smaller under NBC [ $\tilde{b}_c^{(0)} = \beta\Lambda/\mathcal{N}$ , Eq. (59)] than under DBC [Eq. (54)]. In fact, real nanomagnet assemblies will exhibit intermediate (Robin-type) boundary conditions, with the Biot number  $\text{Bi}_b$  interpolating between the two limits analysed here.

*Local-to-global crossover.* We have demonstrated that the analytical stability criterion (54) provides a compact condition for the onset of collective heating: the renormalized feedback coefficient  $\tilde{b}$  must be positive (*i.e.* the bare SLP must be self-amplifying and the interfacial coupling strong enough to transmit the feedback to the matrix) and must exceed the critical threshold  $\tilde{b}_c$ , which depends on the eigenvalue spectrum, nanoscale losses, and source geometry. In the physically prevalent regime ( $\tilde{b} < 0$ , self-limiting feedback), the system is unconditionally stable and heating remains localised at the nanomagnet sites; the transition to global heating requires engineering the system into the self-amplifying regime (case 2 of Sec. III D 1), for instance by tuning the nanoparticle diameter or field amplitude into a region where  $b_p > 0$ .

*Assembly-scale heating and two-scale consistency.* The coarse-grained assembly-scale equation correctly captures the qualitative features of the macroscopic temperature field, such as the dome-shaped profiles under DBC, spatially uniform rise under NBC, and recovers the classical lumped-parameter hyperthermia model as a special case (NBC with uniform source). We then show that the dominant quantitative mismatch between the naive coarse description and the full nanoscale computation originates from a time-scale normalisation: the assembly-scale loss coefficient in Eq. (35) is set to unity, while the physical nanoscale loss rate is  $\beta \ll 1$ . Correcting this through the analytically matched coefficients of Eqs. (72)–(73) allows us to reduce the RMS error by a factor of  $\sim 4$  for NBC and  $\sim 2$  for DBC, attributing the residual to multi-mode dynamics that a single-effective-mode coarse description cannot capture.

*Design implications.* We believe that the present framework will help to identify several controllable design parameters for tuning the thermal response of nanomag-

net assemblies: (i) the interparticle spacing  $d$ , which sets both the source density and the dimensionless thermal parameters via the scaling  $\beta \propto d^2$ ; (ii) the boundary thermal conductance, which interpolates between the DBC (maximum heterogeneity) and NBC (maximum temperature) limits; (iii) the interfacial coupling  $\gamma_s$ , whose interplay with the bare SLP feedback  $b_p$  determines the sign and magnitude of  $\tilde{b}$  and thereby controls whether the local-to-global crossover is accessible; and (iv) the nanoscale loss coefficient  $L_m$ , which provides a dissipation channel that competes with the zero-mode accumulation under NBC.

For magnetic hyperthermia applications, our results suggest that thermally confined (Neumann-like) assemblies with dense packing maximise the absolute temperature rise, whereas well-thermalised (Dirichlet-like) assemblies with moderate packing preserve spatial selectivity.

The one-dimensional local-to-global heating crossover framework we have developed here can be extended in several directions. First, the generalisation to two- and three-dimensional nanomagnet arrays is conceptually straightforward within the modal formalism, although the computational cost of the matrix exponential should increase. Second, the linearized source term  $\tilde{a} + \tilde{b}\theta$  can be replaced by the full nonlinear SLP dependence to capture saturation effects in the supercritical regime; we may proceed by solving the stochastic Landau-Lifshitz equation. Third, the Robin boundary condition (combining Dirichlet and Neumann) can be treated via the transcendental eigenvalue equation, bridging the two limiting cases analysed here. Finally, coupling this framework to realistic magnetic response models (including polydispersity, dipolar interactions beyond the perturbative approach, and Brown relaxation) would allow for a more direct comparison with experimental hyperthermia data, which naturally operate near the local-to-global crossover. Unfortunately, this particular extension can only be carried out using numerical simulations with a relatively high cost.

<sup>1</sup>E. Pop, Energy dissipation and transport in nanoscale devices, *Nano Research* **3**, 147 (2010).

<sup>2</sup>G. Chen, *Nanoscale Energy Transport and Conversion: A Parallel Treatment of Electrons, Molecules, Phonons, and Photons* (Oxford University Press, Oxford, 2005).

<sup>3</sup>G. Benenti, D. Donadio, S. Lepri, and R. Livi, Non-fourier heat transport in nanosystems, *La Rivista del Nuovo Cimento* **46**, 105–161 (2023).

<sup>4</sup>R. E. Rosensweig, Heating magnetic fluid with alternating magnetic field, *J. Magn. Magn. Mater.* **252**, 370 (2002), proceedings of the 9th International Conference on Magnetic Fluids, 23-27 Jul. 2001.

<sup>5</sup>D. Ortega and Q. Pankhurst, Magnetic hyperthermia (2013) pp. 60–88.

<sup>6</sup>R. Hergt, S. Dutz, R. Müller, and M. Zeisberger, Magnetic particle hyperthermia: nanoparticle magnetism and materials development for cancer therapy, *J. Phys.: Condens. Mater.* **18**, 2919 (2006).

<sup>7</sup>A. T. Bell, The impact of nanoscience on heterogeneous catalysis, *Science* **299**, 1688 (2003).

<sup>8</sup>M. Haruta, Size- and support-dependency in the catalytic activity of gold, *Catalysis Today* **36**, 153 (1997).

<sup>9</sup>J. K. Nørskov, T. Bligaard, J. Rossmeisl, and C. H. Christensen, Towards the computational design of solid catalysts, *Nature Chemistry* **1**, 37 (2009).

<sup>10</sup>G. E. W. Bauer, E. Saitoh, and B. J. van Wees, Spin caloritronics, *Nature Materials* **11**, 391 (2012).

<sup>11</sup>K. Uchida, S. Takahashi, K. Harii, J. Ieda, W. Koshibae, K. Ando, S. Maekawa, and E. Saitoh, Observation of the spin seebeck effect, *Nature* **455**, 778 (2008).

<sup>12</sup>H. Adachi, K.-i. Uchida, E. Saitoh, and S. Maekawa, Theory of the spin seebeck effect, *Reports on Progress in Physics* **76**, 036501 (2013).

<sup>13</sup>M. El Baraji, V. Javerliac, W. Guo, G. Prenat, and B. Dieny, Dynamic compact model of thermally assisted switching magnetic tunnel junctions, *Journal of Applied Physics* **106**, 10.1063/1.3259373 (2009).

<sup>14</sup>G. Herzog, S. Krause, and R. Wiesendanger, Heat assisted spin torque switching of quasistable nanomagnets across a vacuum gap, *Applied Physics Letters* **96**, 10.1063/1.3354023 (2010).

<sup>15</sup>P. W. Granitzka, E. Jal, L. L. Guyader, M. Savoini, D. J. Higley, T. Liu, Z. Chen, T. Chase, H. Ohldag, G. L. Dakovsky, W. Schlotter, S. Carron, M. Hoffman, P. Shafer, E. Arenholz, O. Hellwig, V. Mehta, Y. K. Takahashi, J. Wang, E. E. Fullerton, J. Stöhr, A. H. Reid, and H. A. Dürr, Magnetic switching in granular fept layers promoted by near-field laser enhancement, *Nano Letters* **10.1021/acs.nanolett.7b00052** (2017).

<sup>16</sup>Riedinger, A and Guardia, P and Curcio, A and Garcia, MA and Cingolani, R and Manna, L and Pellegrino, T, Subnanometer local temperature probing and remotely controlled drug release based on azo-functionalized iron oxide nanoparticles, *Nano letters* **13**, 2399 (2013).

<sup>17</sup>J. Dong and J. I. Zink, Taking the temperature of the interiors of magnetically heated nanoparticles, *ACS Nano* **8**, 5199 (2014).

<sup>18</sup>D. Serantes, P. Nieves, O. Chubykalo-Fesenko, S. Ruta, R. Chantrell, and O. Hovorka, Local heat release in magnetic nanoparticle hyperthermia: When individual particle hysteresis loops do not represent the local heating, *Physical Review B* **102**, 214412 (2020).

<sup>19</sup>J. B. Weaver, A. M. Rauwerdink, and E. W. Hansen, Magnetic nanoparticle temperature estimation, *Medical Physics* **36**, 1822 (2009).

<sup>20</sup>R. P. Tan, J. Carrey, and M. Respaud, Magnetic hyperthermia properties of nanoparticles inside lysosomes using kinetic monte carlo simulations: Influence of key parameters and dipolar interactions, and evidence for strong spatial variation of heating power, *Physical Review B* **90**, 10.1103/physrevb.90.214421 (2014).

<sup>21</sup>I. Astefanoaei and A. Stancu, A computational study of the bio-heat transfer in magnetic hyperthermia cancer therapy, *J. Appl. Phys.* **125**, 194701 (2019).

<sup>22</sup>Y. Gu, R. Piñol, R. Moreno-Loshuertos, C. D. S. Brites, J. Zeler, A. Martínez, G. Maurin-Pasturel, P. Fernández-Silva, J. Marco-Brualla, P. Téllez, R. Cases, R. N. Belsué, D. Bonvin, L. D. Carlos, and A. Millán, Local temperature increments and induced cell death in intracellular magnetic hyperthermia, *ACS Nano* **17**, 6822 (2023).

<sup>23</sup>B. T. Mai, P. B. Balakrishnan, M. J. Barthel, F. Piccardi, D. Niculaes, F. Marinaro, S. Fernandes, A. Curcio, H. Kakwere, G. Autret, R. Cingolani, F. Gazeau, and T. Pellegrino, Thermoresponsive iron oxide nanocubes for an effective clinical translation of magnetic hyperthermia and heat-mediated chemotherapy, *ACS Applied Materials & Interfaces* **11**, 5727–5739 (2019).

<sup>24</sup>B. Mehdaoui, R. P. Tan, A. Meffre, J. Carrey, S. Lachaize, B. Chaudret, and M. Respaud, Increase of magnetic hyperthermia efficiency due to dipolar interactions in low-anisotropy magnetic nanoparticles: Theoretical and experimental results, *Phys. Rev. B* **87**, 174419 (2013).

<sup>25</sup>J.-L. Déjardin, F. Vernay, M. Respaud, and H. Kachkachi, Effect of dipolar interactions and dc magnetic field on the specific absorption rate of an array of magnetic nanoparticles, *Journal of Applied Physics* **121**, 10.1063/1.4984013 (2017).

- <sup>26</sup>V. Boucher, C. Lacroix, L. P. Carignan, A. Yelon, and D. Ménard, *Appl. Phys. Lett* **98**, 112502 (2011).
- <sup>27</sup>P. Ilg and M. Kröger, Dynamics of interacting magnetic nanoparticles: effective behavior from competition between brownian and néel relaxation, *Physical Chemistry Chemical Physics* **22**, 22244–22259 (2020).
- <sup>28</sup>W. Figueiredo and W. Schwarzacher, Magnetic relaxation and thermal properties of a two-dimensional array of dipolar-coupled nanoparticles, *Journal of Physics: Condensed Matter* **19**, 276203 (2007).
- <sup>29</sup>E. H. Sánchez, M. Vasilakaki, S. S. Lee, P. S. Normile, M. S. Andersson, R. Mathieu, A. López-Ortega, B. P. Pichon, D. Peddis, C. Binns, P. Nordblad, K. Trohidou, J. Nogués, and J. A. De Toro, Crossover from individual to collective magnetism in dense nanoparticle systems: Local anisotropy versus dipolar interactions, *Small* **18**, 10.1002/sml.202106762 (2022).
- <sup>30</sup>F. Vernay, Z. Sabsabi, H. Kachkachi, *Phys. Rev. B* **90**, 094416 (2014).
- <sup>31</sup>H. C. Davis, S. Kang, J.-H. Lee, T.-H. Shin, H. Putterman, J. Cheon, and M. G. Shapiro, Nanoscale heat transfer from magnetic nanoparticles and ferritin in an alternating magnetic field, *Biophysical Journal* **118**, 1502–1510 (2020).
- <sup>32</sup>R. Hergt, R. Hiergeist, I. Hilger, W. Kaiser, Y. Lapatnikov, S. Margel, and U. Richter, Maghemite nanoparticles with very high ac-losses for application in rf-magnetic hyperthermia, *Journal of Magnetism and Magnetic Materials* **270**, 345–357 (2004).
- <sup>33</sup>J.-L. Déjardin and H. Kachkachi, Time profile of temperature rise in assemblies of nanomagnets, *Journal of Magnetism and Magnetic Materials* **556**, 169354 (2022).
- <sup>34</sup>H.-K. Lyeo and D. G. Cahill, Thermal conductance of interfaces between highly dissimilar materials, *Physical Review B* **73**, 10.1103/physrevb.73.144301 (2006).
- <sup>35</sup>D. G. Cahill, P. V. Braun, G. Chen, D. R. Clarke, S. Fan, K. E. Goodson, P. Keblinski, W. P. King, G. D. Mahan, A. Majumdar, H. J. Maris, S. R. Phillpot, E. Pop, and L. Shi, *Appl. Phys. Reviews* **1**, 011305 (2014).
- <sup>36</sup>J.-L. Déjardin, H. Kachkachi, Heat generation and diffusion in an assembly of magnetic nanoparticles: Application to magnetic hyperthermia., *Applied Sciences* **14**, 5757 (2024).
- <sup>37</sup>R. A. Rytov, V.A. Bautin and N.A. Ussov, Towards optimal thermal distribution in magnetic hyperthermia, *Scientific. Rep.* **12**, 1 (2022).
- <sup>38</sup>A. Talapatra and A. O. Adeyeye, Linear chains of nanomagnets: engineering the effective magnetic anisotropy, *Nanoscale* **12**, 20933–20944 (2020).
- <sup>39</sup>M. Anand, V. Banerjee, and J. Carrey, Relaxation in one-dimensional chains of interacting magnetic nanoparticles: Analytical formula and kinetic monte carlo simulations, *Physical Review B* **99**, 10.1103/physrevb.99.024402 (2019).
- <sup>40</sup>A. M. Huízar-Félix, D. Muñoz, I. Orue, C. Magén, A. Ibarra, J. M. Barandiarán, A. Muela, and M. L. Fdez-Gubieda, Assemblies of magnetite nanoparticles extracted from magnetotactic bacteria: A magnetic study, *Applied Physics Letters* **108**, 10.1063/1.4941835 (2016).
- <sup>41</sup>M. Grmela, G. Lebon, P. C. Dauby, and M. Bousmina, Ballistic-diffusive heat conduction at nanoscale: Generic approach, *Physics Letters A* **339**, 237 (2005).
- <sup>42</sup>N. Yang, G. Zhang, and B. Li, Violation of Fourier's law and anomalous heat diffusion in silicon, *Nano Today* **5**, 85 (2010), also available as arXiv:1002.3419.
- <sup>43</sup>D. Jou, A. Sellitto, and F. X. Alvarez, Heat waves and phonon-wall collisions in nanowires, *Proceedings of the Royal Society A: Mathematical, Physical and Engineering Sciences* **467**, 2520 (2011).
- <sup>44</sup>G. Cahill, W. K. Ford, K. E. Goodson, G. D. Mahan, A. Majumdar, H. J. Maris, R. Merlin, S. R. Phillpot, *Appl. Physics* **93**, 793 (2003).
- <sup>45</sup>J. M. Ziman, *Electrons and Phonons: The Theory of Transport Phenomena in Solids* (Oxford University Press, Oxford, 1960).
- <sup>46</sup>H. Rezgui, Phonon hydrodynamic transport: Observation of thermal wave-like flow and second sound propagation in graphene at 100 k, *ACS Omega* **8**, 23964 (2023).
- <sup>47</sup>E. Ziambaras and P. Hyldgaard, Phonon Knudsen flow in nanostructured semiconductor systems, *Journal of Applied Physics* **99**, 054303 (2005).
- <sup>48</sup>P. Vernotte, Les paradoxes de la théorie continue de l'équation de la chaleur, *Comptes Rendus de l'Académie des Sciences* **246**, 3154 (1958).
- <sup>49</sup>C. Cattaneo, Sur une forme de l'équation de la chaleur éliminant le paradoxe d'une propagation instantanée, *Comptes Rendus de l'Académie des Sciences* **247**, 431 (1958).
- <sup>50</sup>A. Majumdar, Microscale heat conduction in dielectric thin films, *Journal of Heat Transfer* **115**, 7 (1993).
- <sup>51</sup>G. Chen, Particularities of heat conduction in nanostructures, *Journal of Nanoparticle Research* **2**, 199 (2000).
- <sup>52</sup>J.-L. Déjardin and H. Kachkachi, Heat generation and diffusion in an assembly of magnetic nanoparticles: Application to magnetic hyperthermia, *Applied Sciences* **14**, 5757 (2024).
- <sup>53</sup>H.L. Rodríguez-Luccioni, M.M. Latorre-Esteves, J.J. Méndez-Vega, O.O. Soto, A. R. Rodríguez, C.C. Rinaldi, M.M. Torres-Lugo, Enhanced reduction in cell viability by hyperthermia induced by magnetic nanoparticles, *Int. J. Nanomed.* **6**, 373 (2011).
- <sup>54</sup>B. Mehdaoui, A. Meffre, J. Carrey, S. Lachaize, L.-M. Lacroix, M. Gougeon, B. Chaudret, and M. Respaud, Optimal Size of Nanoparticles for Magnetic Hyperthermia: A Combined Theoretical and Experimental Study, *Adv. Functional Mater.* **21**, 4573 (2011).
- <sup>55</sup>B. Mehdaoui, J. Carrey, M. Stadler, A. Cornejo, C. Nayral, F. Delpech, B. Chaudret, and M. Respaud, Influence of a transverse static magnetic field on the magnetic hyperthermia..., *Appl. Phys. Lett.* **100**, 052403 (2012).
- <sup>56</sup>C. Haase and U. Nowak, Role of dipole-dipole interactions for hyperthermia heating of magnetic nanoparticle ensembles, *Phys. Rev. B* **85**, 045435 (2012).
- <sup>57</sup>G. Vallejo-Fernandez and K. O'Grady, Effect of the distribution of anisotropy constants on hysteresis losses for magnetic hyperthermia applications, *Applied Physics Letters* **103**, 142417 (2013), <https://doi.org/10.1063/1.4824649>.
- <sup>58</sup>I. Conde-Leboran, D. Baldomir, C. Martinez-Boubeta, O. Chubykalo-Fesenko, M. P. del Morales, G. Salas, D. Cabrera, J. Camarero, F. J. Teran, and D. Serantes, A Single Picture Explains Diversity of Hyperthermia Response of Magnetic Nanoparticles, *The Journal of Physical Chemistry C* **119**, 15698 (2015).
- <sup>59</sup>S. Ruta, R. Chantrell, and O. Hovorka, Unified model of hyperthermia via hysteresis heating in systems of interacting magnetic nanoparticles, *Sci. Rep.* **5**, 9090 (2015).
- <sup>60</sup>P. M. Morse and H. Feshbach, *Methods of theoretical physics* (McGraw-Hill, New York, 1953).
- <sup>61</sup>D. G. Duffy, *Green's functions with applications* (Chapman and Hall/CRC, 2015).
- <sup>62</sup>J. L. Garcia-Palacios, On the Statics and Dynamics of Magnetoanisotropic Nanoparticles, in *Advances in Chemical Physics*, Vol. 112 (John Wiley & Sons, Inc., 2007) pp. 1–210.
- <sup>63</sup>Z. Sabsabi, F. Vernay, O. Iglesias, H. Kachkachi, Interplay between surface anisotropy and dipolar interactions in an assembly of nanomagnets, *Phys. Rev. B* **88**, 104424 (2013).
- <sup>64</sup>F. V. D. Ledue and H. Kachkachi, Magnetization relaxation of interacting chains of nanomagnets, In preparation.
- <sup>65</sup>M. Timko, A. Dzarova, J. Kovac, A. Skumiel, A. Jozefczak, T. Hornowski, H. Gojzewski, V. Zavisova, M. Koneracka, A. Sprincova, O. Strbak, P. Kopcansky, and N. Tomasovcova, Magnetic properties and heating effect in bacterial magnetic nanoparticles, *Journal of Magnetism and Magnetic Materials* **321**, 1521 (2009).
- <sup>66</sup>M. L. Fdez-Gubieda, J. Alonso, A. García-Prieto, A. García-Arribas, L. Fernández Barquín, and A. Muela, Magnetotactic bacteria for cancer therapy, *J. Appl. Phys.* **128**, 070902 (2020).

## Appendix A: Linearized SLP Coefficients from Magnetic Response

In the main text, the local heating power at site  $\xi_n$  was linearized as a temperature-dependent source, see Eq. (12). Here we provide the explicit expressions of the coefficients  $a_p, b_p$  in terms of nanomagnet and field parameters, including dipolar-interaction (DI) effects.

### Linearized SLP: linear response theory

In linear-response theory, the SLP is given by Eq. (9), where  $\chi_{\text{eq}}$  is the equilibrium susceptibility and  $\Gamma(T)$  the relaxation rate, expressed in terms of the energy barrier  $\sigma = KV/k_B T$  and the DI coefficient  $\lambda$ . Approximate analytical expressions for the latter were developed in Refs. 30, 62, and 63. In zero DC magnetic field, the following approximate expression of  $\Gamma(T)$  was obtained in Ref. 64,

$$\Gamma_{\parallel}(0, \sigma, \xi) = \frac{2\sqrt{\sigma}}{\sqrt{\pi\tau_0}} e^{-\sigma(1+4\tilde{\lambda})}. \quad (\text{A1})$$

Then, expanding in the relative temperature elevation  $\theta = (T - T_0)/T_0$ , we obtain the linearized SLP in Eq. (12) with the following baseline and linear temperature-feedback coefficients

$$a_p = A_0 \left[ \left(1 - \frac{1}{\sigma_0}\right) + \left(1 - \frac{2}{\sigma_0}\right) \tilde{\lambda} \right] \frac{\eta_0}{1 + \eta_0^2}, \quad (\text{A2})$$

$$b_p = A_0 \frac{\eta_0}{1 + \eta_0^2} \left\{ -1 + \frac{1}{2} \left(1 - \frac{1}{\sigma_0}\right) (2\sigma_0 - 1) \left(\frac{\eta_0^2 - 1}{\eta_0^2 + 1}\right) + \left[-1 + \frac{1}{2} \left(10\sigma_0 - 13 + \frac{2}{\sigma_0}\right) \left(\frac{\eta_0^2 - 1}{\eta_0^2 + 1}\right)\right] \tilde{\lambda} \right\}, \quad (\text{A3})$$

where we have introduced the standard dimensionless parameters

$$\sigma_0 = \frac{KV}{k_B T_0}, \quad V = \frac{\pi}{6} D^3, \quad (\text{A4})$$

$$\varpi_0 = \omega\tau_0, \quad (\text{A5})$$

$$\lambda = \frac{\mu_0 M_s^2 V^2}{4\pi d^3} \frac{1}{2KV}. \quad (\text{A6})$$

and the effective relaxation parameter (including DI) reads<sup>64</sup>

$$\eta_0 = \frac{\sqrt{\pi}}{2} \varpi_0 \frac{\exp\left[\sigma_0(1 + 4\tilde{\lambda})\right]}{\sqrt{\sigma_0}}. \quad (\text{A7})$$

Dipolar interactions renormalize  $\lambda$  via the Riemann zeta factor:

$$\tilde{\lambda} = \lambda \zeta_R(3). \quad (\text{A8})$$

Here  $\zeta_R$  denotes the Riemann zeta function and should not be confused with the thermal coupling coefficient  $\zeta$  introduced in the main text; for a chain  $\zeta_R(3) \simeq 1.202$ .

The SLP prefactor

$$A_0 = \frac{\mu_0 M_s^2 V}{k_B T_0} \cdot \frac{\mu_0 h_0^2 \omega}{2} \quad (\text{A9})$$

gives the scale of magnetic energy dissipation, with dimensions of power per unit volume ( $\text{W}/\text{m}^3$ ).

Equations (A2)–(A3) provide the explicit mapping from magnetic and geometrical parameters ( $K, M_s, V, d$ ) and AC-field parameters ( $h_0, \omega$ ) to the effective temperature-dependent heating law used throughout this work.

### Relationship to dimensionless coefficients in the main text

The SLP coefficients  $a_p$  and  $b_p$  enter the thermal problem at three successive description levels, each involving a different rescaling:

1. **Nanomagnet-scale coefficients**  $a = \Upsilon_0 a_p$  and  $b = \Upsilon_0 b_p$ , with the scaling prefactor  $\Upsilon_0$  given in Eq. (21).
2. **Renormalized coefficients**  $\tilde{a}$  and  $\tilde{b}$  [Eq. (19)], which account for finite interfacial thermal resistance through the dimensionless coupling strength  $\gamma$  and appear in the nanomagnet-scale heat equation (18).
3. **Coarse-grained coefficients**  $a_{\text{cg}} = a/\beta_N$  and  $b_{\text{cg}} = b/\beta_N$  [Eq. (62)], which govern the assembly-scale source term (37), with  $\beta_N = L_N t_d / (\rho_m c_v m)$  the assembly-scale loss parameter.

This hierarchy clarifies that the same underlying magnetic physics (encoded in  $a_p$  and  $b_p$ ) gives rise to different effective coefficients at different description levels, due to interfacial effects ( $\gamma$ ), loss scaling ( $L_m$  vs  $L_N$ ), and spatial averaging.

### Parameter study for magnetite nanomagnets

For magnetite nanomagnets, we use the physical parameters in Table V to study the dependence of SLP coefficients  $a_p$  and  $b_p$  on key parameters. The reference values correspond to those used in Sec. V.

TABLE V: Physical parameters used in the SAR coefficient study.

Parameter	Symbol	Default Value
Nanoparticle diameter	$D$	12.0 nm
Interfacial coefficient	$h_s$	0.330 W/(m <sup>2</sup> ·K)
AC field amplitude	$h_0$	38.2 kA/m
AC field frequency	$f_0$	194.0 kHz
Material	—	Magnetite

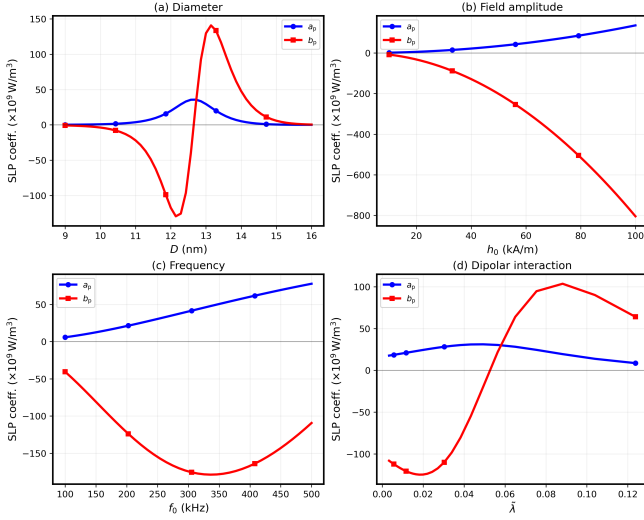


FIG. 14: Dependence of SLP coefficients on (a) nanoparticle diameter  $D$  and (b) AC field amplitude  $h_0$ . Solid lines:  $a_p$ ; dashed lines:  $b_p$ .

Figure 14 shows how  $a_p$  and  $b_p$  vary with nanomagnet diameter and field amplitude. The baseline heating strength  $a_p$  generally increases with both  $D$  and  $h_0$ , while the feedback coefficient  $b_p$  remains negative (indicating self-limiting heating) and becomes more negative with increasing parameters, promoting thermal localization.

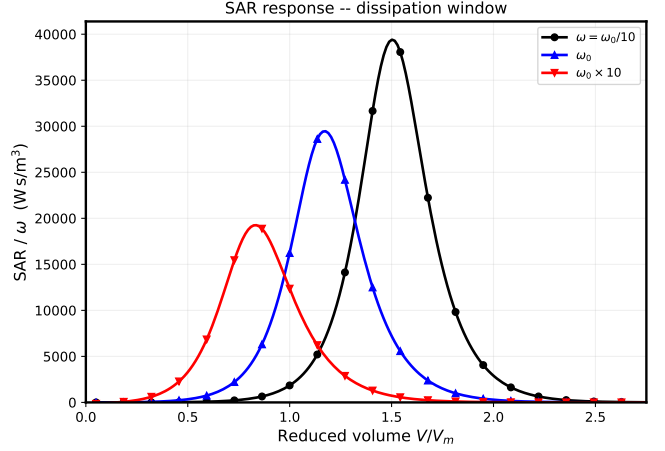


FIG. 15: Specific loss power (SLP) normalized by frequency  $\omega$  as a function of reduced volume  $V/V_m$  for three different driving frequencies:  $\omega = \omega_0/10$ ,  $\omega_0$ , and  $\omega_0 \times 10$ . The peak position shifts systematically with frequency, demonstrating the frequency-tunable dissipation window.

The existence of the dissipation window, revealed by the SLP coefficients  $a_p$  and  $b_p$  in Fig. 14, directly manifests in the SLP response shown in Fig. 15. These plots demonstrate how the SLP( $V/V_m$ ) curves exhibit distinct peaks that shift systematically with driving frequency, confirming the theoretical prediction of a frequency-tunable dissipation window.

At the reference frequency  $\omega_0$ , a well-defined peak emerges where the driving frequency matches the natural timescales of the nanomagnet system, enabling optimal energy absorption. When the frequency decreases to  $\omega_0/10$ , the peak shifts toward larger volumes ( $V/V_m$ ), indicating that lower frequencies couple efficiently to larger magnetic elements. Conversely, at  $\omega_0 \times 10$ , the peak moves to smaller volumes, showing that higher frequencies effectively drive smaller nanomagnets.

This frequency-dependent tunability of the dissipation window underscores the critical importance of matching the driving frequency to the nanomagnet volume distribution for optimal SLP performance in applications such as magnetic hyperthermia. Additionally, the observed variations in peak broadening and amplitude across frequencies reflect changes in the resonance quality factor and energy transfer efficiency within the dissipation window.

## Appendix B: Eigenfunctions and modal solutions for Dirichlet and Neumann boundary conditions

The dimensionless heat equation (18),

$$\frac{\partial \theta}{\partial \tau} - \frac{\partial^2 \theta}{\partial \xi^2} = \sum_{n=0}^{\mathcal{N}-1} [\tilde{a} + \tilde{b} \theta(\xi_n, \tau)] \delta(\xi - \xi_n) - \beta \theta(\xi, \tau), \quad (18)$$

is defined on the domain  $0 \leq \xi \leq \Lambda$  with  $\xi_n = n$  ( $n = 0, \dots, \mathcal{N} - 1$ ) and  $\Lambda = \mathcal{N} - 1$ . Its solution depends on the boundary conditions (BC) imposed at  $\xi = 0$  and  $\xi = \Lambda$ . In this appendix we solve Eq. (18) for two limiting choices — Dirichlet (ideal heat bath) and Neumann (perfect insulation) — and investigate the role of the BC in the formation and persistence of localized thermal hotspots at the nanomagnet positions.

### Motivation

The Dirichlet condition  $\theta = 0$  at both ends models an assembly whose boundary is in perfect thermal contact with a reservoir at the ambient temperature  $T_0$ . This is appropriate, for example, for nanomagnets deposited on a well-conducting substrate. The Neumann (no-flux) condition  $\partial_\xi \theta = 0$  at both ends models a thermally insulated boundary, as encountered in biological systems (e.g. magnetotactic bacteria in a low-conductivity aqueous environment<sup>65,66</sup>) or in free-standing nanocomposite films. Because the boundary conditions control whether heat can escape through the system edges, they directly affect the amplitude and contrast of the temperature field at the nanomagnet positions and therefore influence the very existence of hotspots.

### Dirichlet boundary conditions

We impose

$$\theta(0, \tau) = \theta(\Lambda, \tau) = 0, \quad (\text{B1})$$

corresponding to ideal thermal baths at the chain ends. The orthonormal eigenfunctions of the operator  $-\partial_\xi^2$  satisfying these conditions are

$$\phi_r^{(\text{D})}(\xi) = \sqrt{\frac{2}{\Lambda}} \sin\left(\frac{r\pi\xi}{\Lambda}\right), \quad r = 1, 2, \dots, \quad (\text{B2})$$

with eigenvalues

$$\lambda_r^{(\text{D})} = \left(\frac{r\pi}{\Lambda}\right)^2, \quad r = 1, 2, \dots \quad (\text{B3})$$

The lowest eigenvalue is  $\lambda_1^{(\text{D})} = (\pi/\Lambda)^2 > 0$ ; no zero mode exists. Expanding  $\theta(\xi, \tau) = \sum_{r \geq 1} c_r(\tau) \phi_r^{(\text{D})}(\xi)$ , one obtains the modal system

$$\frac{d\mathbf{c}}{d\tau} = \mathbf{B}^{(\text{D})} \mathbf{c} + \mathbf{d}^{(\text{D})}, \quad (\text{B4})$$

where, after truncation to  $R$  modes,  $\mathbf{c} = (c_1, \dots, c_R)^\top$ ,

$$B_{rs}^{(\text{D})} = -(\lambda_r^{(\text{D})} + \beta) \delta_{rs} + \tilde{b} \mathcal{M}_{rs}^{(\text{D})}, \quad (\text{B5})$$

$$d_r^{(\text{D})} = \tilde{a} \mathcal{S}_r^{(\text{D})}, \quad (\text{B6})$$

and the modal coupling matrix and source vector are

$$\mathcal{M}_{rs}^{(\text{D})} = \sum_{n=0}^{\mathcal{N}-1} \phi_r^{(\text{D})}(\xi_n) \phi_s^{(\text{D})}(\xi_n), \quad (\text{B7})$$

$$\mathcal{S}_r^{(\text{D})} = \sum_{n=0}^{\mathcal{N}-1} \phi_r^{(\text{D})}(\xi_n). \quad (\text{B8})$$

A crucial observation is that  $\phi_r^{(\text{D})}(0) = \phi_r^{(\text{D})}(\Lambda) = 0$  for every  $r$ . Consequently, the boundary nanomagnets  $n = 0$  and  $n = \mathcal{N} - 1$  contribute nothing to either  $\mathcal{M}_{rs}^{(\text{D})}$  or  $\mathcal{S}_r^{(\text{D})}$ : they inject heat into the medium, but the Dirichlet condition immediately drains it, rendering them *thermally invisible* in the modal decomposition.

For vanishing initial conditions,  $\mathbf{c}(0) = \mathbf{0}$ , the exact solution reads

$$\mathbf{c}(\tau) = (\mathbf{B}^{(\text{D})})^{-1} (e^{\mathbf{B}^{(\text{D})}\tau} - \mathbf{I}) \mathbf{d}^{(\text{D})}, \quad (\text{B9})$$

provided  $\mathbf{B}^{(\text{D})}$  is invertible (i.e. the system admits a steady state).

### Neumann boundary conditions

We now impose homogeneous Neumann (no-flux) conditions,

$$\left. \frac{\partial \theta}{\partial \xi} \right|_{\xi=0} = \left. \frac{\partial \theta}{\partial \xi} \right|_{\xi=\Lambda} = 0, \quad (\text{B10})$$

corresponding to perfectly insulated chain ends.

The orthonormal eigenfunctions of  $-\partial_\xi^2$  with these conditions are

$$\phi_r^{(\text{N})}(\xi) = \begin{cases} \frac{1}{\sqrt{\Lambda}}, & r = 0, \\ \sqrt{\frac{2}{\Lambda}} \cos\left(\frac{r\pi\xi}{\Lambda}\right), & r = 1, 2, \dots, \end{cases} \quad (\text{B11})$$

with eigenvalues

$$\lambda_r^{(\text{N})} = \left(\frac{r\pi}{\Lambda}\right)^2, \quad r = 0, 1, 2, \dots \quad (\text{B12})$$

In particular,  $\lambda_0^{(\text{N})} = 0$ : the Neumann spectrum admits a *zero mode* — a spatially uniform temperature perturbation — that is absent from the Dirichlet spectrum. For  $r \geq 1$  the eigenvalues coincide with the Dirichlet ones.

Expanding in the Neumann basis,  $\theta(\xi, \tau) = \sum_{r \geq 0} c_r(\tau) \phi_r^{(\text{N})}(\xi)$ , one obtains an analogous modal system,

$$\frac{d\mathbf{c}}{d\tau} = \mathbf{B}^{(\text{N})} \mathbf{c} + \mathbf{d}^{(\text{N})}, \quad (\text{B13})$$

where now  $\mathbf{c} = (c_0, c_1, \dots, c_R)^\top$ , and

$$B_{rs}^{(\text{N})} = -(\lambda_r^{(\text{N})} + \beta) \delta_{rs} + \tilde{b} \mathcal{M}_{rs}^{(\text{N})}, \quad (\text{B14})$$

$$d_r^{(\text{N})} = \tilde{a} \mathcal{S}_r^{(\text{N})}, \quad (\text{B15})$$

with

$$\mathcal{M}_{rs}^{(N)} = \sum_{n=0}^{\mathcal{N}-1} \phi_r^{(N)}(\xi_n) \phi_s^{(N)}(\xi_n), \quad (\text{B16})$$

$$\mathcal{S}_r^{(N)} = \sum_{n=0}^{\mathcal{N}-1} \phi_r^{(N)}(\xi_n). \quad (\text{B17})$$

Unlike the Dirichlet case,  $\phi_r^{(N)}(0) = 1/\sqrt{\Lambda} \neq 0$  (for  $r = 0$ ) and  $\phi_r^{(N)}(0) = \sqrt{2/\Lambda} \neq 0$  (for  $r \geq 1$ ). Therefore, the boundary nanomagnets at  $n = 0$  and  $n = \mathcal{N} - 1$  contribute fully to the source vector and coupling matrix. All  $\mathcal{N}$  particles are *thermally active* in the Neumann formulation.

The formal solution is again

$$\mathbf{c}(\tau) = (\mathbf{B}^{(N)})^{-1} (e^{\mathbf{B}^{(N)}\tau} - \mathbf{I}) \mathbf{d}^{(N)}, \quad (\text{B18})$$

provided  $\mathbf{B}^{(N)}$  is invertible.

### The zero mode and global heat accumulation

The  $r = 0$  component of the Neumann modal system deserves special attention. Projecting onto  $\phi_0^{(N)} = 1/\sqrt{\Lambda}$  gives

$$\begin{aligned} \frac{dc_0}{d\tau} = & -\beta c_0 + \tilde{b} \frac{\mathcal{N}}{\Lambda} c_0 \\ & + \tilde{b} \sum_{s \geq 1} \mathcal{M}_{0s}^{(N)} c_s + \tilde{a} \frac{\mathcal{N}}{\sqrt{\Lambda}}, \end{aligned} \quad (\text{B19})$$

where we have used  $\mathcal{M}_{00}^{(N)} = \sum_n [\phi_0^{(N)}(\xi_n)]^2 = \mathcal{N}/\Lambda$ .

In the absence of mode coupling (diagonal approximation), the zero-mode amplitude grows or decays at rate

$$\sigma_0 = -\beta + \tilde{b} \frac{\mathcal{N}}{\Lambda}. \quad (\text{B20})$$

This rate is zero when

$$\tilde{b} = \tilde{b}_c^{(0)} \equiv \frac{\beta \Lambda}{\mathcal{N}}. \quad (\text{B21})$$

For  $\beta \rightarrow 0$  (negligible nanoscale losses),  $\tilde{b}_c^{(0)} \rightarrow 0$ : any nonzero positive feedback destabilises the uniform channel. Physically, this reflects the fact that, with insulated boundaries and no volumetric losses, there is no mechanism to remove heat from the system; the temperature drifts upward without bound.

Contrast this with the Dirichlet case, where the fundamental-mode stability criterion reads (cf. Eq. (54))

$$\tilde{b}_c^{(D)} = \frac{\lambda_1^{(D)} + \beta}{\frac{2}{\Lambda} \sum_{n=0}^{\mathcal{N}-1} \sin^2\left(\frac{\pi \xi_n}{\Lambda}\right)}, \quad (\text{B22})$$

which remains finite even for  $\beta = 0$  because  $\lambda_1^{(D)} > 0$ . Diffusion toward the boundary heat sinks alone is sufficient to stabilise the system, independently of the nanoscale loss coefficient.

*Summary:* the existence of the zero mode makes the Neumann system generically less stable than its Dirichlet counterpart. In the physically relevant regime  $\tilde{b} < 0$  (self-limiting feedback) and  $\beta > 0$ , both systems admit steady states, but their temperature levels and spatial structures differ qualitatively, as discussed next.

### Steady-state temperature fields

In steady state ( $dc/d\tau = 0$ ), the temperature field ( $\alpha = D$  or  $N$ ) is

$$\theta_{ss}^{(\alpha)}(\xi) = - \sum_r \frac{d_r^{(\alpha)}}{B_{rr}^{(\alpha)}} \phi_r^{(\alpha)}(\xi) + (\text{off-diag. corrections}), \quad (\text{B23})$$

where the diagonal approximation (neglecting mode coupling through  $\tilde{b} \mathcal{M}_{rs}$ ,  $r \neq s$ ) captures the leading structure. The full solution is obtained from  $\mathbf{c}_{ss} = -(\mathbf{B}^{(\alpha)})^{-1} \mathbf{d}^{(\alpha)}$ .

Two structural differences are noteworthy:

1. **Uniform temperature offset (Neumann only).** The zero-mode contribution to the Neumann steady state is (using Eq. (B19))

$$\theta_{ss}^{(N)} \Big|_{r=0} = \frac{\tilde{a} \mathcal{N} / \Lambda}{\beta - \tilde{b} \mathcal{N} / \Lambda}, \quad (\text{B24})$$

which represents a spatially uniform temperature elevation of the entire chain. No analogous contribution exists in the Dirichlet solution, where  $\theta$  vanishes at the boundaries by construction. For small  $\beta$  and  $\tilde{b} < 0$ ,

$$\theta_{ss}^{(N)} \Big|_{r=0} \simeq \frac{\tilde{a}}{|\tilde{b}|}, \quad (\text{B25})$$

which depends only on the ratio of baseline (or background) heating to feedback strength and is independent of  $\beta$  and the system size.

2. **Boundary nanomagnet temperatures.** For the Dirichlet case,  $\theta_{ss}^{(D)}(\xi_0) = \theta_{ss}^{(D)}(\xi_{\mathcal{N}-1}) = 0$ : the boundary nanomagnets always sit at the ambient temperature, regardless of the heating strength. For the Neumann case,  $\theta_{ss}^{(N)}(\xi_0)$  and  $\theta_{ss}^{(N)}(\xi_{\mathcal{N}-1})$  are finite and, in many configurations, comparable to the temperature of interior particles.

### Hotspot contrast and the role of boundary conditions

A natural measure of the spatial localization of heating is the *hotspot contrast*, defined as the temperature

difference between a nanomagnet position and the midpoint between two adjacent nanomagnets. For interior nanomagnet  $n$  ( $\alpha = \text{D}$  or  $\text{N}$ ),

$$\Delta\theta_n^{(\alpha)} = \theta_{\text{ss}}^{(\alpha)}(\xi_n) - \frac{1}{2} \left[ \theta_{\text{ss}}^{(\alpha)}(\xi_n - \frac{1}{2}) + \theta_{\text{ss}}^{(\alpha)}(\xi_n + \frac{1}{2}) \right]. \quad (\text{B26})$$

Because the zero mode ( $r = 0$ ) is spatially uniform, it cancels exactly in  $\Delta\theta_n^{(\text{N})}$ :

$$\Delta\theta_n^{(\text{N})} = \sum_{r \geq 1} c_{r,\text{ss}}^{(\text{N})} [\phi_r^{(\text{N})}(\xi_n) - \frac{1}{2} \phi_r^{(\text{N})}(\xi_n - \frac{1}{2}) - \frac{1}{2} \phi_r^{(\text{N})}(\xi_n + \frac{1}{2})]. \quad (\text{B27})$$

Therefore, the hotspot contrast is controlled entirely by the  $r \geq 1$  modes in both the Dirichlet and Neumann cases. Since these modes share the same eigenvalues  $\lambda_r = (r\pi/\Lambda)^2$ , the contrast depends on two factors that differ between the boundary conditions: (i) the *source projections*  $\mathcal{S}_r^{(\alpha)}$ , which determine how efficiently the nanomagnet array drives each mode, and (ii) the *modal coupling matrices*  $\mathcal{M}_{rs}^{(\alpha)}$ , which control mode mixing through the feedback term  $\tilde{b}$ .

A key difference arises from the behaviour at the chain boundaries. With Dirichlet BC, the sine functions vanish at  $\xi = 0$  and  $\xi = \Lambda$ , so the two boundary nanomagnets ( $n = 0, n = \mathcal{N} - 1$ ) do not contribute to any mode. With Neumann BC, the cosine functions attain their extremal values at the boundaries ( $\cos 0 = 1, \cos r\pi = (-1)^r$ ), so the boundary nanomagnets couple *maximally* to the modal decomposition. As a result, the effective number of active sources is

$$\mathcal{N}_{\text{eff}}^{(\text{D})} = \mathcal{N} - 2, \quad \mathcal{N}_{\text{eff}}^{(\text{N})} = \mathcal{N}. \quad (\text{B28})$$

For long chains ( $\mathcal{N} \gg 1$ ) this difference is negligible, but for short chains or near the edges it becomes significant.

### Single-source Green's function and local temperature peaks

A complementary perspective is obtained from the diagonal Green's function  $G^{(\alpha)}(\xi, \xi) = \sum_r [\phi_r^{(\alpha)}(\xi)]^2 / (\lambda_r^{(\alpha)} + \beta)$ , which measures the steady-state temperature at a point  $\xi$  due to a unit point source at the same location. Explicitly,

$$G^{(\text{D})}(\xi, \xi) = \frac{2}{\Lambda} \sum_{r=1}^{\infty} \frac{\sin^2(r\pi\xi/\Lambda)}{(r\pi/\Lambda)^2 + \beta}, \quad (\text{B29})$$

$$G^{(\text{N})}(\xi, \xi) = \frac{1}{\Lambda\beta} + \frac{2}{\Lambda} \sum_{r=1}^{\infty} \frac{\cos^2(r\pi\xi/\Lambda)}{(r\pi/\Lambda)^2 + \beta}. \quad (\text{B30})$$

Using  $\sin^2 x + \cos^2 x = 1$ , the difference is

$$\begin{aligned} G^{(\text{N})}(\xi, \xi) - G^{(\text{D})}(\xi, \xi) \\ = \frac{1}{\Lambda\beta} + \frac{2}{\Lambda} \sum_{r=1}^{\infty} \frac{\cos(2r\pi\xi/\Lambda)}{(r\pi/\Lambda)^2 + \beta} > 0 \end{aligned} \quad (\text{B31})$$

for all  $\xi \in (0, \Lambda)$ . Therefore,

$$G^{(\text{N})}(\xi, \xi) > G^{(\text{D})}(\xi, \xi) \quad (\text{B32})$$

for all interior points.

The local temperature peak produced by each nanomagnet is always higher under Neumann BC than under Dirichlet BC. The dominant contribution to the excess comes from the zero-mode term  $1/(\Lambda\beta)$ , which diverges as  $\beta \rightarrow 0$ . This reflects the global heat accumulation that occurs when no heat can escape through the boundaries.

### Comparative stability criteria

The stability of the steady state against perturbations is governed by the eigenvalues of  $\mathbf{B}^{(\alpha)}$ . In the diagonal approximation, the growth rate of mode  $r$  is

$$\sigma_r^{(\alpha)} = -(\lambda_r^{(\alpha)} + \beta) + \tilde{b} \mathcal{M}_{rr}^{(\alpha)}. \quad (\text{B33})$$

The most damaging mode (highest  $\sigma_r$ , assuming  $\tilde{b} > 0$ ) is the one with the smallest bare decay rate  $\lambda_r^{(\alpha)} + \beta$ .

**Dirichlet:** The slowest mode is  $r = 1$  with bare decay rate  $\lambda_1^{(\text{D})} + \beta = (\pi/\Lambda)^2 + \beta > 0$ . The system is stable for

$$\tilde{b} < \tilde{b}_c^{(\text{D})} = \frac{(\pi/\Lambda)^2 + \beta}{\mathcal{M}_{11}^{(\text{D})}}. \quad (\text{B34})$$

Even for  $\beta = 0$ , the boundary-induced diffusive decay  $(\pi/\Lambda)^2$  ensures a finite stability margin.

**Neumann:** The slowest mode is  $r = 0$  with bare decay rate  $\lambda_0^{(\text{N})} + \beta = \beta$ . The system is stable for

$$\tilde{b} < \tilde{b}_c^{(0)} = \frac{\beta\Lambda}{\mathcal{N}}. \quad (\text{B35})$$

For  $\beta \rightarrow 0$ ,  $\tilde{b}_c^{(0)} \rightarrow 0$ : any positive feedback, however small, drives a global thermal runaway through the uniform channel.

In the physically prevalent regime of self-limiting feedback ( $\tilde{b} < 0$ , as is the case for the reference magnetite-PMMA parameters of Table I; see also Appendix A), both systems are unconditionally stable. However, the Neumann system attains a higher steady-state temperature level, as shown above.

For the higher modes ( $r \geq 1$ ), the stability criteria involve the same eigenvalues  $\lambda_r = (r\pi/\Lambda)^2$  in both cases, with only the coupling constants  $\mathcal{M}_{rr}^{(\alpha)}$  differing. These differences are significant primarily for low- $r$  modes and near the boundaries.

### Physical discussion: which BC favours hotspots?

The comparison reveals that the answer depends on whether ‘‘hotspot’’ is defined in absolute or relative terms.

**1. Absolute temperature at the nanomagnet positions.** The Neumann BC yields strictly higher temperatures at every source position [Eq. (B32)], for two reasons: (a) the zero mode accumulates heat globally when no boundary drain is available, and (b) all  $\mathcal{N}$  nanomagnets contribute as active sources, including the two boundary nanomagnets that are suppressed under Dirichlet BC.

**2. Hotspot contrast (temperature peak relative to local baseline).** The zero mode cancels in the hotspot contrast (B26), which depends only on  $r \geq 1$  modes. For interior particles far from the boundaries, the difference between sine and cosine projections diminishes and the contrasts are comparable. Near the boundaries, however, the Neumann BC provides substantially higher contrast because boundary nanomagnets are active sources rather than thermally dead sinks.

**3. Relative temperature variance.** The relative spatial variance

$$\mathcal{V}_{\text{rel}}^{(\alpha)} = \frac{\text{Var}(\theta_{\text{ss}}^{(\alpha)})}{\langle \theta_{\text{ss}}^{(\alpha)} \rangle^2}, \quad (\text{B36})$$

where  $\langle \cdot \rangle = \mathcal{N}^{-1} \sum_n (\cdot)$  denotes the average over nanomagnet positions. In the Dirichlet case, the mean  $\langle \theta_{\text{ss}}^{(\text{D})} \rangle$  is moderate because boundary nanomagnets contribute zero; the variance is controlled by the dome-shaped profile that vanishes at the edges. In the Neumann case, the mean is raised by the zero mode [Eq. (B24)], while the variance is set by higher modes. For small  $\beta$ , the zero-mode pedestal dominates the mean, suppressing the relative variance:

$$\mathcal{V}_{\text{rel}}^{(\text{N})} \ll \mathcal{V}_{\text{rel}}^{(\text{D})} \quad \text{when } \beta \ll |\tilde{b}| \frac{\mathcal{N}}{\Lambda}. \quad (\text{B37})$$

*In relative terms, the Dirichlet BC preserves sharper spatial heterogeneity, because the zero-temperature boundary condition forces the profile to vary between zero and its maximum, whereas the Neumann profile fluctuates about a high pedestal.*

## Summary

Table VI collects the main differences.

The choice of boundary condition is therefore not merely a mathematical convenience but has direct physical consequences for the thermal landscape in nanomagnet assemblies. Dirichlet conditions model well-thermalized boundaries and preserve strong spatial heterogeneity, but at the cost of suppressing edge effects and underestimating absolute temperatures. Neumann conditions model thermal confinement and yield higher absolute temperatures at all positions, but the resulting pedestal reduces the relative contrast of hotspots. In practice, real systems are likely intermediate (Robin BC), with the effective Biot number  $\text{Bi}_b = h_b d / \kappa_m$  interpolating between the two limits:  $\text{Bi}_b \rightarrow \infty$  recovers Dirichlet, while  $\text{Bi}_b \rightarrow 0$  recovers Neumann.

TABLE VI: Comparison of Dirichlet and Neumann boundary conditions for the nanomagnet-scale heat equation.

Property	Dirichlet	Neumann
Zero mode	absent	present ( $\lambda_0 = 0$ )
Boundary NM activity	suppressed	full
Active sources	$\mathcal{N} - 2$	$\mathcal{N}$
SS ( $\beta = 0, \tilde{b} \leq 0$ )	exists	only if $\tilde{b} < 0$
SS ( $\beta = 0, \tilde{b} > 0$ )	if $\tilde{b} < \tilde{b}_c^{(\text{D})}$	does not exist
Absolute NM temp.	lower	higher
Hotspot contrast (int.)	comparable	comparable
Hotspot contrast (bdy.)	zero	finite
Relative spatial var.	higher	lower (pedestal)

For applications requiring *maximum local temperature* at the nanomagnet sites (e.g. bond-breaking, catalysis), Neumann-like confinement is favourable. For applications requiring *maximum spatial contrast* between hot and cold regions (e.g. targeted drug release, site-selective activation), Dirichlet-like boundary thermalization is preferable.

## Appendix C: Green's function formulation of the nanomagnet-scale heat equation

For completeness, we present an alternative derivation of the temperature field at the nanomagnet scale based on the Green's function of the one-dimensional diffusion operator with Dirichlet boundary conditions<sup>61</sup>. This formulation provides a real-space interpretation of the modal solution derived in Sec. III A and is useful for benchmarking, physical interpretation, and future extensions.

Throughout this appendix, we work in dimensional variables and consider the nanomagnet-resolved heat equation, valid on time scales comparable to or slightly larger than an AC-field period and on spatial scales comparable to the nanomagnet size and interparticle spacing.

### Green's function of the nanoscale diffusion operator with losses

At the nanomagnet scale, the temperature elevation  $\Delta T(x, t) = T(x, t) - T_0$  in the embedding matrix obeys the heat equation with localized sources and nanoscale environmental losses [see Eq. (4)]:

$$\rho_m c_{v,m} \frac{\partial \Delta T}{\partial t} = \kappa_m \partial_x^2 \Delta T - L_m \Delta T(x, t) + \sum_{n=0}^{\mathcal{N}-1} P_n \delta(x - x_n), \quad (\text{C1})$$

where  $\kappa_m$  and  $\rho_m c_{v,m}$  are the thermal conductivity and volumetric heat capacity of the matrix,  $L_m$  is the nanoscale volumetric Newton cooling coefficient, and  $P_n$  is the time-averaged power dissipated by nanomagnet  $n$ . Note that interfacial thermal exchange is incorporated

through the self-consistent relation between  $P_n$  and the local temperature difference, as given by Eq. (10) in the main text.

We define the linear diffusion-with-loss operator

$$\mathcal{L} = -\kappa_m \partial_x^2 + L_m, \quad (\text{C2})$$

acting on the interval  $0 \leq x \leq L$  with Dirichlet boundary conditions

$$\Delta T(0, t) = \Delta T(L, t) = 0, \quad (\text{C3})$$

corresponding to a thermally regulated environment.

The Green's function  $G(x, x'; t)$  is defined as the solution of

$$\rho_m c_{v,m} \frac{\partial G}{\partial t} + \mathcal{L}G = \delta(t) \delta(x - x'), \quad (\text{C4})$$

with  $G(x, x'; t < 0) = 0$  and homogeneous Dirichlet boundary conditions<sup>60,61</sup>.

### Modal representation of the Green's function

Expanding  $G$  in the Dirichlet eigenfunctions

$$\phi_r(x) = \sqrt{\frac{2}{L}} \sin\left(\frac{r\pi x}{L}\right), \quad r = 1, 2, \dots, \quad (\text{C5})$$

with eigenvalues

$$k_r^2 = \left(\frac{r\pi}{L}\right)^2, \quad (\text{C6})$$

and noting that these are eigenfunctions of both  $-\partial_x^2$  and the identity operator, we obtain<sup>60,61</sup>

$$G(x, x'; t) = \sum_{r=1}^{\infty} \phi_r(x) \phi_r(x') \exp\left[-\left(\frac{\kappa_m k_r^2 + L_m}{\rho_m c_{v,m}}\right)t\right]. \quad (\text{C7})$$

Each mode relaxes with a characteristic time

$$\tau_r = \frac{\rho_m c_{v,m}}{\kappa_m k_r^2 + L_m}, \quad (\text{C8})$$

which includes contributions from both spatial diffusion and nanoscale environmental losses.

### Convolution representation of the temperature field

Using Duhamel's principle, the solution of Eq. (C1) with zero initial condition can be written as

$$\Delta T(x, t) = \sum_{n=0}^{\mathcal{N}-1} \int_0^t P_n G(x, x_n; t - t') dt'. \quad (\text{C9})$$

Evaluating this expression at the nanomagnet positions  $x = x_m$  gives

$$\Delta T_m(t) = \sum_{n=0}^{\mathcal{N}-1} P_n \int_0^t G(x_m, x_n; t - t') dt', \quad (\text{C10})$$

which describes the mutual thermal coupling between nanomagnets mediated by the embedding matrix, including the effects of nanoscale losses.

In steady state, the convolution reduces to

$$\Delta T_m^{(\text{ss})} = \sum_{n=0}^{\mathcal{N}-1} P_n \mathcal{G}(x_m, x_n), \quad (\text{C11})$$

where the static Green's function is

$$\mathcal{G}(x, x') = \sum_{r=1}^{\infty} \frac{\phi_r(x) \phi_r(x')}{\kappa_m k_r^2 + L_m}. \quad (\text{C12})$$

### Relation to the modal solution in Sec. III A

The connection to the dimensionless modal system of Sec. III A is established as follows. Substituting the linearized source (13), after eliminating the nanomagnet internal temperature via the self-consistent relation (10), into Eq. (C1) and introducing the dimensionless variables  $\xi = x/d$ ,  $\tau = t/t_d$ , and  $\theta = \Delta T/T_0$  [Eq. (17)], one recovers exactly the nanomagnet-scale heat equation (18) with renormalized coefficients  $\tilde{a}$  and  $\tilde{b}$  [Eq. (19)]. Projecting onto the dimensionless eigenfunctions (25) then yields the coupled ODE system (27) with decay rates  $\lambda_r + \beta = (r\pi/\Lambda)^2 + \beta$ , where the first term arises from spatial diffusion (the dimensional eigenvalue  $\kappa_m k_r^2$  rescaled by  $t_d$ ) and the second from nanoscale losses ( $\beta = L_m t_d / (\rho_m c_{v,m})$ ).

The Green's-function formulation thus provides a complementary real-space view of the same physics captured by the modal expansion: localized heating by discrete nanomagnets, diffusive spreading in the matrix, thermal coupling through the temperature field, and nanoscale environmental losses.

### Scope and limitations

It is important to emphasize that the present formulation applies to the *nanomagnet-resolved* temperature field, prior to any spatial or temporal coarse-graining. The interfacial coefficient  $h_s$  enters through the self-consistent relation between  $P_n$  and  $\Delta T(x_n, t)$  as given in Eq. (10) of the main text, and is incorporated into the renormalized coefficients  $\tilde{a}$  and  $\tilde{b}$ . The nanoscale loss coefficient  $L_m$  describes direct environmental coupling at the nanomagnet level and must not be confused with the effective volumetric leakage coefficient  $L_N$  used in coarse-grained, assembly-scale models. The mathematical connection between these two descriptions and the hierarchical relationship  $L_N = L_m + L_{\text{emergent}}$  is addressed in Sec. III C.